Numerical Modelling of Thermochemically Driven Fluid Flow With Non-Newtonian Rheology

Applied to the Earth's Lithosphere and Mantle

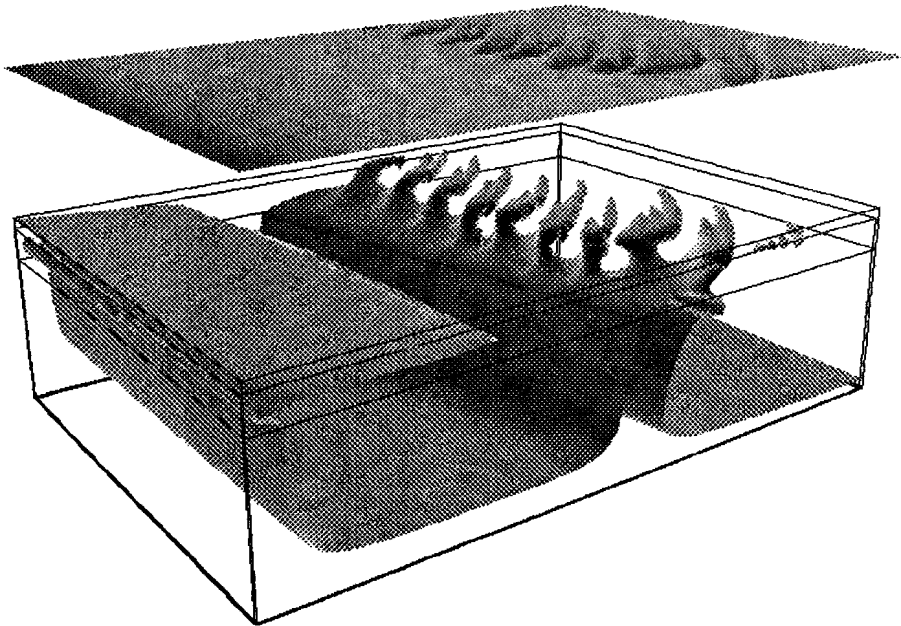PETER EDWIN VAN KEKEN

Numerical Modelling of Thermochemically Driven Fluid Flow With Non-Newtonian Rheology

Applied to the Earth's Lithosphere and Mantle

PETER EDWIN VAN KEKEN

Numerical Modelling of Thermochemically Driven Fluid Flow With Non-Newtonian Rheology

Applied to the Earth's Lithosphere and Mantle

Numeriek modelleren van thermochemisch gedreven
vloeistofstroming met niet-Newtonse rheologie
toegepast op de lithosfeer en mantel van de Aarde

(met een samenvatting in het Nederlands)

PROEFSCHRIFT

TER VERKRIJGING VAN DE GRAAD VAN DOCTOR AAN DE
RIJKSUNIVERSITEIT TE UTRECHT OP GEZAG VAN DE
RECTOR MAGNIFICUS PROF.DR J.A. VAN GINKEL
INGEVOLGE HET BESLUIT VAN HET COLLEGE VAN DEKANEN
IN HET OPENBAAR TE VERDEDIGEN OP VRIJDAG
11 JUNI 1993 DES NAMIDDAGS TE 12.45 UUR

DOOR

PETER EDWIN VAN KEKEN

GEBOREN OP 29 MAART 1966 TE HOEVELAKEN

PROMOTOR: PROF.DR N.J. VLAAR

There is an anecdote about my brother, Bernard, who is an atmospheric scientist in the State University of New York at Albany. Bernard worked for the General Electric Research Laboratory in Schenectady, New York, for a while, where he discovered that silver iodide could precipitate certain sorts of clouds as snow or rain. His laboratory was a sensational mess, however, where a clumsy stranger could die in a thousand different ways, depending on where he stumbled.

The company had a safety officer who nearly swooned when he saw this jungle of deadfalls and snares and hair-trigger booby traps. He bawled out my brother.

My brother said this to him, tapping his own forehead with his fingertips: "If you think this laboratory is bad, you should see what it's like in *here*."

[Vonnegut, 1976].

Kreten van kinderen op straat
klinken van ver, als uit de tijd,
gedempt en helder tegelijk.
Want sneeuw is er altijd weer van vroeger
en ligt er altijd voor het eerst.
Het blijft omdat het overgaat.

[Eijkelboom, datum onbekend].

.

Voor mijn ouders

The research described in this thesis was carried out at the

Department of Theoretical Geophysics
Institute of Earth Sciences
University of Utrecht
P.O. Box 80.021
3508 TA Utrecht
The Netherlands

The author can be reached through E-mail at: keken@geof.ruu.nl

Contents

Chapter 7 The effects of rheological boundaries on inducing sharp diapiric flows in the upper mantle

Chapter 8 The cooling of the Earth in the Archaean

Chapter 1

Introduction and summary

1.1 Introduction

In the 25 years after the general acceptance of the concept of plate tectonics we have witnessed large progress in observational, laboratory, forward modelling and inversion techniques. These provide a clear view of the immense complexities that are facing us when studying the dynamics of the interior of the Earth. Plate tectonics can be seen as both an expression of, and the mechanism controlling, the dynamic cooling of the Earth. Traditionally, the soloistic and often opposing, simplifying views have been adopted of either the 'convectionist', who sees plate tectonics merely as the surface expression of mantle convection, or the 'tectonist', who views the plates as the only dynamic component in an otherwise passive mantle. It clearly emerges from the observational data, knowledge of deformation mechanisms, and the available modelling and inversion results, that a uniform approach, combining the two views would be more appropriate to describe the dynamics of the Earth. The generalized description is made difficult by the very distinct nature of the lithosphere, as expressed by the thermal, compositional and rheological differences from the underlying mantle.

   In this thesis I will present some model studies of the deformation of lithosphere and mantle, recognizing the strong influence of compositional and rheological differences. The approach is more 'convectionistic' than 'tectonistic', in that only ductile deformation is considered and that the brittle/elastic behaviour of the upper and colder lithospheric parts is ignored. Ductile creep has been used with varying success in 'tectonist' models of lithosphere dynamics, but the application of these methods to global deformation problems are, as yet, computationally too expensive.

1.2 Basic assumptions

The Earth's complicated rheological and dynamical behaviour necessitates the use of simplifying assumptions when modelling its dynamics. The next few paragraphs discuss some of the assumptions that are made here.

11

Slow deformation of the Earth below the upper parts of the lithosphere is gov-
erned by high temperature ductile creep. Experimental deformation work at high
temperature shows that the creep behaviour of candidate mantle rocks are well
described by Dorn's equation for power law creep

$$\dot{\varepsilon} = A\sigma^n \exp[-H/RT]\qquad(1.1)$$

where $\dot{\varepsilon}$ is strain rate, σ applied differential stress, T temperature, R the gas con-
stant, and n, A and H empirically determined constants [Ranalli, 1987]. Extrapola-
tion of this creep equation from laboratory conditions to the much lower tectonic
strain rates is done using theoretical creep equations, derived from microphysical
models. Several mechanisms, based on movement of dislocations in crystals, can
'explain' the power law creep behaviour. The Newtonian mechanism of diffusion
creep can be described by the migration of vacancies in grains and between grain
boundaries. This mechanism is not often found to operate at the high strain rates
normally used in laboratory experiments, but it is expected that this creep mecha-
nism is important in the the Earth at low stresses. Although from a mechanistic
point of view very different, diffusion creep can be described mathematically by
the same power law creep law (1.1), for the special case $n = 1$.

The equations are solved for convection in a Boussinesq fluid at infinite Prandtl
number. The narrow definition of the Boussinesq approximation implies that vis-
cous dissipation is neglected, the fluid is incompressible and all material parame-
ters are constant, except in the gravity term of the equation of motion [Busse,
1989]. In practice, this last condition is relaxed for material parameters other than
density, allowing for e.g. variable viscosity and thermal diffusivity.

First principles are used to derive the mathematical differential equations
describing the dynamics of the physical models, under the assumptions described
above. In the general situation, the equations are time-dependent, non-linear and
non-linearly coupled. For only a few exceptional, simplified cases a closed analyti-
cal form of the solution to the differential equations can be found. Numerical meth-
ods are required to obtain solutions to general problems.

Three-dimensional modelling has become available for simple (e.g. stationary,
or isoviscous) problems. It is expected that within a few years, the progress in
computational methods and increasing availability of computer power will allow
for studies that can treat the full 3-dimensional time-dependent problem with real-
istic rheology within a reasonable production time. For the type of models used in
this thesis it is still necessary, from a computational point of view, to consider
2-dimensional models only. For many applications this is a reasonable approxima-
tion, as the models can be imagined to extend in similar fashion in the third dimen-
sion.

1.3 Scope of the thesis

In the work described in this thesis, I have developed numerical methods to model the dynamical behaviour of the Earth's lithosphere and mantle driven by thermal and compositional buoyancy forces using a non-Newtonian power law rheology. The methods have been applied to three different problems:

Salt tectonics

First, the problem of salt tectonics is considered within this framework. Rocksalt is very weak, and deforms by ductile creep even at upper crustal conditions. The formation of salt diapirs is of large economical interest, considering their role in trapping and migration of oil and gas, and in their possible use for disposal of radioactive waste and storage of energy reserves. Traditionally a constant Newtonian viscosity has been used for the salt in both laboratory and numerical modelling of salt diapirism. Here, the flow behaviour of rocksalt has been studied using an empirical creep law [Spiers et al., 1990], that describes the combined effect of dislocation and diffusion creep mechanisms that are known to occur in natural rocksalt. The effects of temperature, constitutive parameters and strain rate on the viscosity of rocksalt are considered and the rheological law has been used in numerical models of salt diapirism.

Mantle convection

Next, the influence of rheological discontinuities on large scale mantle convection is considered. The role of the transition zone between 400 and 670 km depth on mantle dynamics is still under considerable debate. The discontinuity between upper and lower mantle at 670 km has been described to be a chemical discontinuity by some [e.g. Anderson, 1989; Ita & Stixrude, 1992], and to be a mineralogical phase change by others [e.g. Ito & Takahashi, 1989], although many leave the choice between the two possibilities open [e.g. Silver et al., 1988]. The effect of the hypothesized compositional and/or phase change related discontinuity on mantle convection has been investigated in an increasing number of studies [Vening Meinesz, 1962; Verhoogen, 1965; Schubert et al., 1975; Christensen & Yuen, 1984; Liu et al., 1991; Kellogg, 1991; Zhao et al., 1992; Tackley et al., 1993]. Recent experimental results by Karato & Li [1992] show that the lower mantle might deform predominantly by diffusion creep. This opens up the possibility of a non-Newtonian upper mantle overlying a Newtonian lower mantle. The structure of stationary mantle convection using this type of depth varying rheology been investigated by Van den Berg et al. [1991]. In these models, they find the top boundary layer to behave in a plate-like fashion, that is encouraged by introducing a

lithosphere with higher non-linear dependence in the flow law. Here, these studies are extended to time-dependent models, with specific attention to the interaction of an upwelling lower mantle plume with the rheologically defined transition zone.

Archaean dynamics

Finally, a model is presented that may describe the cooling of the Earth in the Archaean (approx. 3.8-2.7 billion years before present). Geological observations give contradictory indications of the thermal state of the Archaean lithosphere and mantle. The presence of komatiites with high extrusion temperatures in Archaean greenstone belts points to a maximum mantle temperature some 400-500 K higher than present day. On the other hand, the metamorphic signature of Archaean high grade terrains indicates that the continental lithosphere was thermally similar to present day's. This seeming paradox can be explained by a model in which the cratonic regions stabilized early in the Archaean and maintained relatively low temperatures at moderate depths (50-100 km). The cooling of the Earth was governed by rapid convection underneath oceanic lithosphere. Most researchers adopt the uniformitarian point of view that plate tectonics was active in the Archaean, with probably higher plate velocities to account for the rapid heat loss [e.g., Arndt, 1983; Bickle, 1986]. However, it seems very unlikely that plate tectonics can have been active in a hotter mantle. One of the consequences of higher temperatures is the increasing amount of compositionally light basalt that is generated at mid-oceanic ridges by pressure-release melting. In the present day situation, with a crustal thickness of 7 km [McKenzie & Bickle, 1988], the newly created oceanic lithosphere is stable with respect to the underlying mantle [Vlaar & Wortel, 1976; Oxburgh & Parmentier, 1977]. Subduction can only occur for lithosphere that has sufficiently cooled. The mechanical coherency of the lithosphere allows then for the rigid plate-like movement, driven by the pull of the subducting slab and the topography-induced ridge push. At the ridges, hot material fills passively the space left by the spreading plates. In a hotter mantle, pressure-release melting starts deeper and a thicker basaltic layer and depleted harzburgitic zone is created [Sleep & Windley, 1982; Vlaar, 1985; McKenzie & Bickle, 1988]. In a mantle that is hotter by 400-500 K, compared with present day's, the thickness of the basaltic layer can amount to over 50 km [Vlaar & Van den Berg, 1991], creating a permanently stably stratified oceanic lithosphere [Vlaar, 1986]. Lack of mechanical coherency of the relatively weak basalt [Hoffman & Ranalli, 1988], and absence of slab pull and ridge push makes the mechanism of plate tectonics ineffective. Here, an alternative model is presented to describe the cooling of the Archaean Earth, through thermally and compositionally driven convection in the upper mantle.

1.4 Summary

The mathematical equations that are derived from first principles describing the physical model are presented in chapter 2.

The finite element methods, used to solve the non-linear and time-dependent equations, are discussed in chapter 3. The equations of motion, together with the incompressibility constraint, are solved, either using a primitive variable, penalty function method or in the stream function formulation. The methods are compared to published benchmarks, from which it is concluded that the methods are very accurate in describing thermal convection in generalized Newtonian media. In the finite element methods described in chapter 3, the basic physical quantities as temperature and velocity are approximated by continuous functions. In many geophysical applications (e.g. salt diapirism), composition changes as a discontinuous function from one layer to the other. The dynamical evolution of models with discontinuously varying composition are modelled using the stream function methods in conjunction with the marker chain method. In general the viscosity and, consequently, the strain rate are discontinuous across a compositional interface and cannot accurately be modelled by the continuous low order approximation of both stream function methods, leading to non-physical oscillations in the strain rate field and, in case of non-Newtonian fluids in the viscosity field. In chapter 4 the characteristics of this oscillatory behaviour and its influence on the dynamical evolution are discussed. An alternative Lagrangian method, based on the penalty function method, is proposed and compared to the stream function methods. It is concluded that for moderate viscosity contrasts and power law indices the dynamical behaviour of the Rayleigh-Taylor instability is modelled accurately by the stream function methods.

Chapter 5 discusses the implementation of a steady state creep law, describing the two parallel mechanisms of dislocation creep and fluid-enhanced grain-boundary diffusion creep in numerical models of salt diapirism. The effective viscosity of the rocksalt depends on constitutive parameters (such as grain size, activation energy, and shear modulus), temperature and strain rate. For strain rates typical of salt diapirism driven by buoyancy alone, it is found that the average viscosity in the salt varies between 10^{17} Pa $\cdot$ s (for small grain size and high temperature salt) and 10^{20} Pa $\cdot$ s (for large grain size and low temperatures salt). For the larger grain sizes, the dislocation creep mechanism is effective during the most vigorous diapiric stage, At the lower strain rates, and for finer grained salts in the presence of trace amounts of water, the diffusion creep mechanism is dominant throughout the diapiric event. Values for the viscosity of rocksalt that have traditionally been used in numerical and physical modelling, are at the lower end of the range that is found from these experiments.

Chapter 6 and 7 discuss the influence of rheological discontinuities, connected with the major phase transitions, on mantle convection. Time-dependent models of plumes interacting with a rheological interface separating an upper non-Newtonian mantle and a Newtonian lower mantle are studied. It is found that pulsating diapiric structures are shedded off the rheological interface as a consequence of the drop in effective viscosity that the plume experiences, when it moves from the Newtonian lower mantle into the non-Newtonian upper mantle. The diapiric upwellings are discernible in the surface heat flow as discrete pulses, that remain relatively stationary underneath the moving surface plate. The periodicity of the pulsations depends on the Rayleigh number, the effective viscosity contrast across the interface, and, as is shown in chapter 7, the depth level of the rheological interface. Diapirs coming off a rheological boundary at the top of the transition zone are found to occur periodically with a dimensional interval of a few million years, which is comparable to the periodicity of hot spot volcanism, exemplified by the discrete nature of the Hawaiian-Emperor seamount chain.

In chapter 8, some aspects of the dynamical behaviour of the lithosphere and mantle in a hotter Earth are investigated. In an Earth that is hotter by 250-500 K than at present day, the compositional stability and lack of mechanic coherency renders plate tectonics inefficient. Decoupling between the upper and lower basaltic crust may lead to subduction of the brittle hydrated upper crust into the ductile lower crust. At lower crustal pressures, the hydrated basalt transforms efficiently into its higher pressure phase eclogite, which allows for fast recycling of the crustal material. Renewed pressure-release melting leads again to basaltic crust formation. Consumption of latent and advective cooling through magma migration is very efficient. It is proposed that this mechanism may have cooled the mantle in the Early Archaean by several hundreds of degrees.

Chapter 2

Basic equations

In this chapter, the basic equations are considered that describe velocity, pressure, temperature and composition in viscous fluid models as applied to the Earth's interior.

2.1 Conservation equations

Neglecting inertial forces, the equations of conservation of mass, momentum and thermal energy can be written for a Boussinesq fluid in the field of gravity as

$$\nabla \cdot \mathbf{u} = 0 \tag{2.1}$$

$$\nabla p = \nabla \cdot \underline{\sigma} + \rho g \hat{z} \tag{2.2}$$

$$\frac{\partial T}{\partial t} + (\mathbf{u} \cdot \nabla)T = \kappa \nabla^2 T + Q/\rho c_p \tag{2.3}$$

where the meaning of the symbols is specified in table 2.1. For multicomponent fluids conservation of composition (assuming negligible mass diffusion) yields

$$\frac{\partial \Gamma}{\partial t} + (\mathbf{u} \cdot \nabla)\Gamma = 0 \tag{2.4}$$

Together with the boundary and/or initial conditions and the equation of state

$$\rho = \rho(T, \Gamma) \tag{2.5}$$

these equations describe the motion of the fluid, and mass and heat transport for flows driven by thermal and chemical buoyancy forces in the field of gravity.

2.2 Rheological model

The deformation behaviour of mantle rock at high temperatures is described, here, by power law ductile creep [e.g. Kirby, 1983], where strain rate is related to the *n*th power of the deviatoric stress

$$\dot{\varepsilon}_{ij} = A\sigma^{n-1}\sigma_{ij} \tag{2.6}$$

Here σ_{ij} are the components of the deviatoric stress tensor $\underline{\sigma}$, $\dot{\varepsilon}_{ij}$ the components of the strain rate tensor $\underline{\dot{\varepsilon}}$ and σ is the second invariant of the deviatoric stress tensor, or the effective shear stress

$$\sigma = [\,\tfrac{1}{2}\sum_{ij}\sigma_{ij}\sigma_{ij}\,]^{\frac{1}{2}} \tag{2.7}$$

Equivalently, the second invariant of the strain rate tensor, or the effective strain rate, is defined by

$$\dot{\varepsilon} = [\,\tfrac{1}{2}\sum_{ij}\dot{\varepsilon}_{ij}\dot{\varepsilon}_{ij}\,]^{\frac{1}{2}} \tag{2.8}$$

The components of the strain rate tensor are given by

$$\dot{\varepsilon}_{ij} = \tfrac{1}{2}\left[\frac{\partial u_i}{\partial x_j} + \frac{\partial u_j}{\partial x_i}\right] \tag{2.9a}$$

An effective isotropic shear viscosity η is then given by,

$$\eta = \frac{\sigma}{2\dot{\varepsilon}} \tag{2.9b}$$

In engineering and fluid dynamics literature often a slightly different definition of the strain rate tensor and viscosity is used:

$$\dot{\varepsilon}_{ij} = \left[\frac{\partial u_i}{\partial x_j} + \frac{\partial u_j}{\partial x_i}\right] \tag{2.10a}$$

$$\eta = \frac{\sigma}{\dot{\varepsilon}} \tag{2.10b}$$

For these two sets of definitions the factor *A* in (2.6) has a different meaning. This should be taken into account when comparing different models or when applying laboratory measurements of strain rate in mathematical models.

For computational purposes the stress dependence of viscosity is expressed in terms of strain rate, through an inversion of (2.6), giving

$$\eta \;=\; \frac{\sigma}{\dot{\varepsilon}} \;=\; A^{-1/n}\dot{\varepsilon}^{\frac{1-n}{n}} \tag{2.11}$$

2.3 Thermal convection

In convection driven by thermal buoyancy forces alone, the equation of state $\rho = \rho(T)$ is written to a first order approximation as

$$\rho \;=\; \rho_0 + \delta\rho \;=\; \rho_0 - \alpha\rho_0(T - T_0) \tag{2.12}$$

where $\rho_0 = \rho$ at temperature $T = T_0$ and α the thermal expansion coefficient. Elimination of hydrostatic pressure from (2.2) leads to

$$-\nabla P + \nabla \cdot (\eta\dot{\varepsilon}) \;=\; \alpha\rho_0 g(T - T_0)\hat{z} \tag{2.13}$$

where $P = p - \rho_0 gz$ is the hydrodynamic pressure.

The equations can be non-dimensionalized using the scaling parameters given in table 2.1. Introducing primed quantities $X' = rX$, where r is the scaling parameter, we find for (2.1-2.3)

$$-\nabla P + \nabla \cdot (\eta\dot{\varepsilon}) \;=\; RaT\hat{z} \tag{2.14}$$

$$\nabla \cdot \mathbf{u} \;=\; 0 \tag{2.15}$$

$$\frac{\partial T}{\partial t} + (\mathbf{u} \cdot \nabla)T \;=\; \nabla^2 T + Q \tag{2.16}$$

where primes have been dropped and

$$Ra \;=\; \frac{\rho_0 g\alpha\Delta T_0 h^3}{\kappa_0\eta_0} \tag{2.17}$$

is the (non-dimensional) thermal Rayleigh number.

The three equations (2.14-2.15) can be reduced to one scalar equation through introduction of the stream function ψ, defined by $\mathbf{u} = (\partial\psi/\partial y, \; -\partial\psi/\partial x)^{\mathrm{T}}$, where we choose the y-axis in the negative z-direction. In non-dimensional quantities, the depth is given by $z = 1 - y$. Use of the stream function yields, in dimensionless form

$$\left[\frac{\partial^2}{\partial x^2} - \frac{\partial^2}{\partial y^2}\right]\eta\left[\frac{\partial^2\psi}{\partial x^2} - \frac{\partial^2\psi}{\partial y^2}\right] + 4\frac{\partial^2}{\partial x\partial y}\eta\frac{\partial^2\psi}{\partial x\partial y} \;=\; Ra\frac{\partial T}{\partial x} \tag{2.18}$$

The continuity equation is now automatically satisfied, at the cost of fourth order derivatives in the resulting differential equation.

Table 2.1 Specification of symbols and (if applicable) non-dimensionalisation factors (after [Christensen, 1984a]). R is the gas constant ($R = 8.314$ $Jmol^{-1}K^{-1}$), g the acceleration of gravity ($g = 9.8$ m · s^{-2}), h a specific length scale (in general the depth of the layer), c_p specific heat at constant pressure, and κ_0, η_0, ΔT_0 arbitrarily chosen reference values. The temperature scale is chosen, such that $T_0 = 0$.

Symbol	Meaning	Unit	factor r for non-dimensionalisation
x, y	horizontal, vertical coordinate	m	$1/h$
$\mathbf{u}$	velocity vector, $\mathbf{u} = (v, w)^T$	m · s^{-1}	h/κ_0
∇	$\nabla = (\partial/\partial x, \partial/\partial y)^T$	m^{-1}	h
$\hat{z}$	unit vector in direction of gravity		
t	time	s	κ_0/h^2
ψ	stream function	$m^2 s^{-1}$	$1/\kappa_0$
η	dynamical viscosity	Pa · s	$1/\eta_0$
$\underline{\sigma}$	deviatoric stress tensor	Pa	$h^2/(\kappa_0\eta_0)$
$\underline{\dot{\epsilon}}$	strain rate tensor	s^{-1}	h^2/κ_0
ρ	mass density	kg · m^{-3}	$1/\rho_0$
κ	thermal diffusivity	$m^2 s^{-1}$	$1/\kappa_0$
α	thermal expansion coefficient	K^{-1}	
T	temperature	K	$1/\Delta T_0$
p	pressure	Pa	$h^2/(\kappa_0\eta_0)$
Γ	composition function		
Q	Internal heating per unit volume	Wm^{-3}	$h^2/(c_p\kappa_0\Delta T_0\rho_0)$

2.4 Thermochemical convection

When both temperature and composition determine the density, the equation of state becomes

$$\rho = \rho(\Gamma)[1 - \alpha(T - T_0)] \tag{2.19}$$

For a model with two layers of different composition, Γ can be defined as a step function and the compositional density is then given by

$$\rho(\Gamma) = \rho_0 + \Delta\rho\Gamma \tag{2.20}$$

where $\Delta\rho$ is the density difference between the two layers. Similar formulations

are possible for multi-layer fluids or models with continuously varying composition. For this particular two-layer case we can write

$$\frac{\partial \rho}{\partial x} = \Delta\rho \frac{\partial \Gamma}{\partial x} - [\rho_0 + \Gamma\Delta\rho]\alpha \frac{\partial T}{\partial x} \tag{2.21}$$

and the equation of motion in the stream function formulation becomes

$$\left[\frac{\partial^2}{\partial x^2} - \frac{\partial^2}{\partial y^2}\right]\eta\left[\frac{\partial^2\psi}{\partial x^2} - \frac{\partial^2\psi}{\partial y^2}\right] + 4\frac{\partial^2}{\partial x\partial y}\eta\frac{\partial^2\psi}{\partial x\partial y} =$$

$$\left[\frac{\rho_0 + \Gamma\Delta\rho}{\rho_0}\right]Ra\frac{\partial T}{\partial x} - Rb\frac{\partial \Gamma}{\partial x} \tag{2.22}$$

where Rb is the so-called boundary Rayleigh number

$$Rb = \frac{\Delta\rho g h^3}{\kappa_0 \eta_0} \tag{2.23}$$

Chapter 3

Numerical methods

3.1 Introduction

Several finite element methods have been used, here, to solve the basic equations (2.1-2.4) numerically. General characteristics of these methods are i) subdivision of the model domain into finite elements ii) construction of basis functions using these elements iii) construction of the best approximation to the solution within the function space spanned by these basis functions. The solution found in this manner satisfies the equations in an average sense. This is the weak formulation of the problem, as opposed to the classical solution, that satisfies the equation in each point of the domain. Here the weak formulation known as Galerkin's principle is used. The general application of this method to boundary value problems, incorporation of natural and essential boundary conditions, and the use of the finite element method to construct the basis functions, are described by Cuvelier et al. [1986]. This chapter gives information on the methods that have been employed to solve the basic equations. First, a description is given of the solution of the time-dependent equations of temperature and composition. Next, the different formulations and methods to solve the equations of motion and of mass conservation (2.1-2.2) are considered. The chapter is concluded with some benchmark results.

3.2 Solution of the temperature equation

The heat equation is solved using a linear triangular element with 3 nodal points in the vertices of the elements. The temperature is approximated within an element by

$$T(x, y) = \sum_{j=1}^{3} T_j \, \phi_j(x, y) \tag{3.1}$$

where T_j is the temperature in nodal point j and ϕ_j is the linear shape function connected with this point. Application of the method of Galerkin to (2.3) leads to a system of ordinary differential equations

$$\mathbf{M\dot{T} + ST = f} \tag{3.2}$$

where $\mathbf{T}$ is the vector of unknowns T_i, the dot denotes time derivative, $\mathbf{M}$ is the heat capacity mass matrix, $\mathbf{S}$ the stiffness matrix, associated with the advection and diffusion of heat, and $\mathbf{f}$ the load vector representing the influence of volumetric heat generation and the inhomogeneous boundary conditions. The matrices and load vector are assembled elementwise using element matrices of the form

$$\mathbf{M}_{ij}^e = \int\!\!\int_e \phi_i \phi_j \; dxdy \tag{3.3a}$$

$$\mathbf{S}_{ij}^e = \int\!\!\int_e \kappa \nabla \phi_i \cdot \nabla \phi_j \; dxdy \; + \; \int\!\!\int_e \phi_j (\mathbf{u} \cdot \nabla) \phi_i \; dxdy \tag{3.3b}$$

$$\mathbf{f}_j^e = \int\!\!\int_e \frac{Q}{\rho c_p} \phi_j \; dxdy \tag{3.3c}$$

The effects of the inhomogeneous boundary conditions are later added to the load vector $\mathbf{f}$. The velocity components are obtained from a solution of the equations of motion and numerical values of $\mathbf{u}^T = (v, w)$ are given in the nodal points. The integrals are calculated using Newton-Cotes quadrature, after expanding the velocity components in the linear shape functions

$$v(x, y) = \sum_{k=1}^{3} v_k \phi_k(x, y) \quad , \qquad w(x, y) = \sum_{k=1}^{3} w_k \phi_k(x, y) \tag{3.4}$$

where k corresponds to the local numbering of the nodal points in the element. Newton-Cotes integration of (3.3a) reduces $\mathbf{M}$ to a diagonal matrix. This process of lumping of the mass matrix is computationally convenient as it reduces the work necessary to solve (3.2) and it often increases the accuracy [Zienkiewicz, 1977].

In most of the calculations presented in this thesis, stable solutions to the heat equation could be obtained with the standard (Bubnov-)Galerkin method described above. Grid refinements were used in the few cases that oscillations were found in the temperature solution. Note that for the discretization of the temperature equation no upwinding techniques have been employed. Upwinding can be implemented in these finite element methods by application of the Petrov-Galerkin method [Heinrich et al., 1977]. This suffers from the disadvantage that artificial diffusivity is introduced and the solution may be inaccurate [Cuvelier et al., 1986]. It has been argued that streamline upwinding [Hughes & Brooks, 1982] greatly reduces cross-wind diffusivity. Upwind techniques have found standard application in mantle convection modelling to stabilize solutions of the advection dominated heat equation [Christensen, 1984a; Blankenbach et al., 1989]. A different, and more natural, approach to find stable solutions is the method of characteristics

[Pironneau, 1982], which is introduced in mantle convection modelling by Malevsky & Yuen [1991]. Disadvantage of this method is that high order shape-functions have to be used to reduce the amount of artificial diffusivity, introduced by the interpolation that is inherent in this method.

3.3 Transport equation for composition

There are several ways to represent the composition function Γ. In the field approach, the compositional differences are represented by a (continuous) function Γ and the transport equation (2-4) can be solved for Γ by the method of Galerkin as described above for the temperature. In this case the diffusion connected terms in the stiffness matrix (3.3b) are set to zero ($\kappa = 0$). A disadvantage of the field approach is, that the applicability of the method of Galerkin -*sec*- to the hyperbolic equation (2-4) is not well defined. For particular cases it can be shown that convergence to the correct solution of hyperbolic equations cannot be obtained [Strang & Fix, 1973], and artificial diffusivity needs to be introduced, e.g. through discontinuous elements, streamline upwinding or the method of characteristics. Another disadvantage of the field approach is, that a discontinuous composition function, as is often encountered in geodynamical problems (e.g. the salt-sediment interface in modelling salt dynamics), can not be modelled accurately. The finite element approximation will smear out the interface over at least the length of one element by its linear approximation to the function. Transporting this approximation over a stationary grid will cause distortion and oscillations of the composition function near the interface. One way to circumvent this problem is to define a smoothing of the interface, for example through a hyperbolic tangent function, that transforms the discontinuity into a shape where the function drops smoothly from one discrete value to the other over the length of a few elements [e.g., Christensen, 1992].

A more popular way of representing compositional differences is the tracer method, in which discrete tracers are initially homogeneously distributed through the fluid layer it represents [Gurnis, 1986; Christensen, 1991; Zaleski & Julien, 1992; Weinberg & Schmeling, 1992]. One of the disadvantages of the method is that often a large number of tracer particles is necessary to discretize the composition function Γ. In situations where no large scale mixing of the fluids occurs, the interface between the fluids can efficiently be represented by a chain of markers (marker chain method). In both cases, the positions of the markers or tracers are determined by the initial distribution and the hyperbolic equations

$$\dot{x}_m(t) = v(x_m(t), y_m(t), t)$$
$$\dot{y}_m(t) = w(x_m(t), y_m(t), t)$$

(3.5)

[Christensen & Yuen, 1984].

3.4 Time integration

The equations of motion and mass conservation (2.1-2.2) contain no explicit time-dependence because inertial forces can be neglected. The velocity and pressure fields are determined by the rheology, boundary conditions and the driving forces, which in the general geodynamical context are governed by the distribution of temperature and composition. Time-dependence is introduced in the equations through the heat and composition equations (2.3-2.4) and possibly the boundary conditions. This allows for following predictor-corrector scheme to solve the governing equations [Christensen, 1984a; Hansen & Ebel, 1988]:

> *Specify initial distribution of T and* Γ
> *Determine velocity field* $\mathbf{u}^0$ *at time t by solving (2.1-2.2)*
> $n = 0$
> *Repeat until end of time integration*
> 　*Determine discrete time step* Δt
> 　*Predict temperature and composition distributions,* $T^{n+1(0)}$
> 　　*and* $\Gamma^{n+1(0)}$, *at time* $t + \Delta t$
> 　*Predict velocity field* $\mathbf{u}^{n+1(0)}$ *at time* $t + \Delta t$
>
> 　$i := 1$
> 　*Repeat for each corrector step i*
> 　　*Correct the temperature and composition distributions*
> 　　　$T^{n+1(i)}$ *and* $\Gamma^{n+1(i)}$
> 　　*Correct the velocity field* $\mathbf{u}^{n+1(i)}$
> 　　$i := i + 1$
> 　$n := n + 1$
> 　$t := t + \Delta t$

To predict the temperature a semi-implicit Euler scheme is used to solve the system of equations (3.2)

$$\mathbf{M} \cdot \frac{T^{n+1(0)} - T^n}{\Delta t} + S(\mathbf{u}^n) \cdot T^{n+1(0)} = f^{n+1} \tag{3.6}$$

after which the correction is calculated by a Crank-Nicholson step

$$\mathbf{M} \cdot \frac{T^{n+1(i)} - T^n}{\Delta t} + \frac{1}{2} S(\mathbf{u}^n) \cdot T^n + \frac{1}{2} S(\mathbf{u}^{n+1(i-1)}) \cdot T^{n+1(i)} = f^{n+1} \tag{3.7}$$

for $i = 1, 2, \cdots$ [Hansen & Ebel, 1988]. A similar scheme can be used for Γ in the field approach. In the marker chain (or tracer) method the coordinates of the

markers can be updated by solving (3.5) using an explicit predictor

$$x_m^{(0)}(t + \Delta t) = x_m(t) + v(t) \cdot \Delta t$$
$$y_m^{(0)}(t + \Delta t) = y_m(t) + w(t) \cdot \Delta t$$

(3.8)

(where v and w are the horizontal and vertical components of velocity $\mathbf{u} = (v, w)^T$), and, after solution of the Stokes equation, a Crank-Nicholson corrector,

$$x_m^{(1)}(t + \Delta t) = x_m(t) + \frac{\Delta t}{2} (v^{(0)}(t + \Delta t) + v(t))$$

$$y_m^{(1)}(t + \Delta t) = y_m(t) + \frac{\Delta t}{2} (w^{(0)}(t + \Delta t) + w(t))$$

(3.9)

The corrector step can be repeated to obtain higher accuracy. Ideally, that is in cases where the evolution of velocity $\mathbf{u}$ is exactly known, the scheme is second order correct in time. The choice of time step Δt is based on the Courant criterion

$$\| v\Delta t/\Delta x , w\Delta t/\Delta y \|_\infty \leq 1$$

(3.10)

where Δx and Δy are the (local) grid spacings in horizontal and vertical direction, resp. The choice of the explicit predictor in (3.8) requires this condition for stability. The accuracy of the time integration scheme depends strongly on the spatial structure of the velocity field and the coupling between the temperature and velocity field. For a strongly temperature dependent viscosity, errors in the temperature field will have a stronger effect than in isoviscous flows, which makes a smaller time step necessary. For a number of applications (both Rayleigh-Taylor instabilities and thermal convection experiments), it was found that limiting the time step to be half the Courant step (3.10) and performing only one corrector step gave a satisfactory trade-off between accuracy and computational cost.

Stationary results for purely thermal convection are obtained by explicitly neglecting time-dependence in (2.3) ($\partial T/\partial t \equiv 0$), yielding

$$(\mathbf{u} \cdot \nabla)T = \kappa \nabla^2 T + Q/\rho c_p$$

(3.11)

In this case, the system of equations (2.1-2.2,3.11) is time independent but non-linearly coupled through velocity and temperature. Picard iteration, or successive substitution, is used to solve the system, starting from an initial temperature field. Using temperature dependent and/or non-Newtonian viscosity introduces additional non-linearities in the equations of motion and underrelaxation is needed to obtain convergence of the Picard iteration.

3.5 The equations of motion

For solving the equations of motion (2.2), combined with the continuity equation for an incompressible fluid (2.1), three different finite element methods will be

discussed. Two are based on the stream function formulation (see equation 2.22), that requires the use of higher order elements, as a consequence of the occurring fourth order derivates. The first method to be discussed is the penalty function method, in which pressure is eliminated from the equations of motion (2.2) by a perturbation of the continuity equation. Following section summarizes some important points of chapters 7 and 8 of Cuvelier et al. [1986].

3.5.1 Penalty function method

First the solution of (2.1-2.2) for an isoviscous fluid will be considered. Equation (2.2) reduces to

$$\nabla p \ = \ \eta \nabla^2 \mathbf{u} + \rho g \hat{z} \qquad (3.12)$$

Pressure can only be defined up to an additive constant. The three equations (3.12) and (2.1) can be solved directly for $\mathbf{u}$ and p using the method of Galerkin, but this is computationally inefficient. The discretized system of equations that has to be solved is large as a consequence of the three unknowns (v, w, p) per nodal point. The pressure does not enter the incompressibility constraint and this introduces zeroes on the main diagonal of the stiffness matrix, which complicates the solution of the system considerably.

A way to circumvent these problems is to eliminate the pressure from (3.12) by perturbing the incompressibility constraint

$$\nabla \cdot \mathbf{u} \ = \ - \varepsilon p \qquad (3.13)$$

where ε is small. This is the penalty function method; ε is called the penalty function parameter. Temam [1977] gives a proof for general boundary conditions that the solution to (3.12-3.13) approaches the solution to (2.1-2.2) as $\varepsilon \rightarrow 0$. After discretising the domain, approximating the velocity and pressure by

$$\bar{v}(x,y) \ = \ \sum_{i=1}^{N} v_i \phi_i \ , \ \ \bar{w}(x,y) \ = \ \sum_{i=1}^{N} w_i \phi_i \ , \ \ \bar{p}(x,y) \ = \ \sum_{i=1}^{M} p_i \psi_i \qquad (3.14)$$

and applying the method of Galerkin, the pressure can be eliminated from the discretized equations of motion, yielding a system of equations

$$\mathbf{S} \mathbf{v} + \tau \mathbf{L}_x{}^T \mathbf{D}^{-1} \mathbf{L}_x \mathbf{v} \ = \ \mathbf{0} \qquad (3.15a)$$

$$\mathbf{S} \mathbf{w} + \tau \mathbf{L}_y{}^T \mathbf{D}^{-1} \mathbf{L}_y \mathbf{w} \ = \ \mathbf{f} \qquad (3.15b)$$

$$\mathbf{p} \ = \ \tau \mathbf{D}^{-1} [\ \mathbf{L}_x \mathbf{v} + \mathbf{L}_y \mathbf{w} \ ] \qquad (3.15c)$$

where $\tau = \varepsilon^{-1}$, $\mathbf{v}$ is the vector of unknowns v_i, $\mathbf{w}$ the vector of unknowns w_i, $\mathbf{p}$ the vector of unknowns p_i, and $\mathbf{f}$ the load vector, defined by

$$\mathbf{f}_i = \int_\Omega \rho g \phi_i \, d\Omega \tag{3.15d}$$

The matrix components are given by

$$S_{ij} = \eta \int_\Omega \nabla \phi_i \cdot \nabla \phi_j \, d\Omega \tag{3.15e}$$

$$L_{z,ij} = -\int_\Omega \psi_j \frac{\partial \phi_i}{\partial z} \, d\Omega \qquad z = x, y \tag{3.15f}$$

$$D_{ij} = \int_\Omega \psi_i \psi_j \, d\Omega \tag{3.15g}$$

The above equations are given for homogeneous boundary conditions. Inhomogeneous boundary conditions give a contribution to the load vector f.

The shape functions ϕ_i and ψ_i are constructed using the Crouzeix-Raviart ($P_2^+ - P_1$) element (figure 3.1). Necessary conditions for an element are that basis functions for velocity are continuous over element boundaries and piecewise continuously differentiable. Pressure basis functions should be continuous within the element, and the order of these basis functions should be at least one lower than that of the velocity basis functions. The Crouzeix-Raviart ($P_2^+ - P_1$) element approximates velocity as an extended quadratic function (using the velocity components in the seven nodal points depicted in figure 3.1 as degrees of freedom) and pressure as a linear function using the pressure and its derivatives to x and y in the
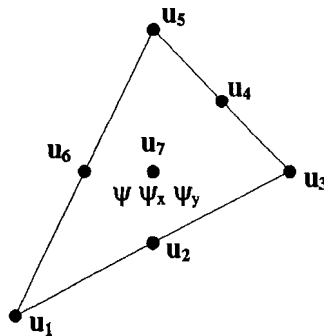

Figure 3.1 *The Crouzeix-Raviart $P_2^+ - P_1$ element.*

barycenter. This element has pleasant properties as to the assembly of the matrix $S + \tau L^T D^{-1} L$: i) the matrix is symmetric and positive definite. ii) construction of the matrix can be carried out elementwise. iii) the velocity components in the barycenter and the pressure derivatives can be eliminated from the system of equations (i.e. they can be expressed as functions of the velocity components from the boundary nodal points only), reducing the number of degrees of freedom with 4. The resulting element has 6 nodal points for velocity and 1 nodal point for pressure (modified Crouzeix-Raviart element). iv) this elimination process makes the pressure matrix D diagonal, with simple inverse D^{-1}.

A more detailed discussion of this element can be found in [Cuvelier et al., 1986].

Choice of penalty function parameter

In the penalty function method, the incompressibility constraint is relaxed to make a more efficient solution of the equations of motion and the conservation of mass possible. To minimize the effects of finite compressibility it is desirable to choose τ as high as possible. However, the penalty function matrix $L^T D^{-1} L$ is singular, and for large τ the total matrix $S + \tau L^T D^{-1} L$ will be singular. Cuvelier et al. [1986] suggest to choose τ in the range

$$10^3 \leq \tau \leq 10^9 \tag{3.16}$$

Throughout the calculations $\tau = 10^6$ has been used.

The choice of the penalty function parameter is less constrained than in the case of incompressible elasticity problems that are solved with the penalty function method [Hughes, 1987]. For compressible elasticity, the constitutive equation is given by

$$\underline{\sigma} = \lambda \nabla \cdot \underline{s} \underline{I} + 2\mu \underline{\varepsilon} \tag{3.17}$$

where μ is the shear modulus, s is the displacement vector, $\underline{\varepsilon}$ the strain tensor and $\underline{I}$ the Kronecker tensor. The Lamé parameter λ is given by

$$\lambda = \frac{2\nu\mu}{1 - 2\nu} \tag{3.18}$$

where ν is Poisson's ratio. In the incompressible case ($\nu = \frac{1}{2}$), λ is unbounded and a different formulation is necessary. The constitutive equation is then written

$$\underline{\sigma} = -p\underline{I} + 2\mu\underline{\varepsilon} \tag{3.19}$$

where the pressure p is introduced as unknown. The additional equation to be solved is just the incompressibility constraint ($\nabla \cdot s = 0$). In the mixed formulation, (3.19) is used as constitutive equation, where the parameter p is defined by

$$0 = \nabla \cdot \mathbf{s} + \frac{p}{\lambda} \qquad (3.20)$$

This leads directly to the penalty function formulation for incompressible elasticity. For the compressible case the average normal stress equals $-\sigma_{kk}/3 = -(\lambda + 2\mu/3)\nabla \cdot \mathbf{s}$. Then, the parameter p from (3.20), $p = -\lambda\nabla \cdot \mathbf{s}$, can only be interpreted as pressure when $\mu \ll \lambda$. Therefore, in the penalty formulation λ has to be chosen finite, but large with respect to μ. Numerical problems arise if λ is chosen too large. Hughes [1987] finds the range

$$10^7 \le \frac{\lambda}{\mu} \le 10^9 \qquad (3.21)$$

to be effective.

The equations for (isotropic) incompressible elasticity and Stokes flow are identical, except for a different meaning of the parameters (the displacement $\mathbf{s}$ is replaced by the velocity $\mathbf{u}$ and μ by the dynamic viscosity η). This would suggest a choice of the penalty parameter τ as a local function of the dynamic viscosity, which would have important consequences for the solution of non-isoviscous flows with the penalty function method. However, it can be shown for a fluid without bulk viscosity, $\zeta = \lambda + 2\eta/3 = 0$, that the average normal stress $-\sigma_{kk}/3$ is always equal to the thermodynamical pressure [Malvern, 1969]. This relaxes the extra constraint on the choice of the penalty function parameter with respect to the dynamic viscosity. The bulk viscosity is related to rapid changes in volume (compared to molecular relaxation processes) and can be neglected in problems with slow deformation [Jarvis & McKenzie, 1980].

It has to be stressed that the viscosity should be scaled properly in a way that the average viscosity is around one. If the average viscosity is much less than one the total matrix $\mathbf{S} + \tau\mathbf{L}^T\mathbf{D}^{-1}\mathbf{L}$ can be singular.

Practical implementation

The Stokes equation, combined with the incompressibility constraint, and the temperature equation (2.1-2.3) are solved using the finite element package Sepran [Segal & Praagman, 1984]. Appendix A contains a description of some technical details of the implementation.

Generalized Newtonian fluids

The rheological model of generalized Newtonian fluid has been used, where the viscosity depends on strain rate, temperature, pressure and composition. The coefficients of the viscous stress matrix (3.15e) have the form

$$S_{ij} = \int\limits_{\Omega} \eta \nabla \phi_i \cdot \nabla \phi_j \; dxdy \tag{3.22}$$

The effective strain rate is a function of gradients of velocity which, in the finite element approximation, are continuous within an element, but in general discontinuous across element boundaries. Pressure is continuous over element boundaries (as it translates to depth in the Boussinesq approximation) and the same holds for the finite element approximation of temperature. Then, the approximation of the viscosity is in general continuous within the elements, but discontinuous across the element boundaries. The integral (3.22) is still integrable and simple tests using a power law creep model have correct convergence behaviour (error in velocity is a function of h^3, error in pressure a function of h^2; h is the element size) and the element shows to be applicable to problems with generalized Newtonian fluids [Jaap van der Zanden, pers. comm., 1992]. A discussion on the effects of composition dependent viscosity is given in chapter 4.

For strain rate dependent viscosity the viscous stress matrix is a function of velocity and the discretized system (3.15) is non-linear. In time-dependent problems Picard sub-iteration is used to solve (3.15), keeping the buoyancy forces and boundary conditions fixed. The velocity field obtained at the previous step is used as initial estimate for the next step.

3.5.2 Stream function formulation

In the stream function formulation, the non-dimensional equation of motion for incompressible thermochemical convection is given by (2.22). The introduction of the stream function reduces the three equations for velocity and pressure to one scalar equation at the cost of fourth order derivatives. Conformity of element shape functions is often imposed to satisfy the basic convergence requirements [Hughes, 1987]. In the stream function formulation, the equation of motion is a fourth order partial differential equation and, for a finite element approximation to be conform, the basis functions should be twice continuously differentiable in each element and at least continuously differentiable throughout the computational domain Ω [Cuvelier et al., 1986]. We consider the implementation of two methods that have been used to solve the equation of motion in the stream function formulation: the first uses a non-conforming type of element [Hansen & Ebel, 1984], the second uses bicubic splines as shape functions [Woidt, 1978; Kopitzke, 1979]. The notation will be used

$$Ra_0 = \frac{\rho_0 \alpha g \Delta T h^3}{\kappa_0 \eta_0} \quad , \qquad Ra(\Gamma) = \left[\frac{\rho_0 + \Gamma \Delta \rho}{\rho_0} \right] Ra_0 \tag{3.23}$$

and a model of two homogeneous fluid layers with different compositional densities will be considered. The function Γ is a step function.

Non-conforming element

The condition of continuity of the slope of shape functions across element boundaries (C_1 continuity) is difficult to impose for conforming elements [Zienkewicz, 1977]. Here a non-conforming element is used, that, although it does not fulfill condition of C_1 continuity, has found successful application in plate bending problems [Zienkewicz, 1977] and mantle convection modelling [Hansen & Ebel, 1984].

The model region Ω is subdivided into rectangular elements with four nodal points in the vertices of the element. In each nodal point a vector of unknowns is defined with three components

$$\mathbf{a}_i = \left[\bar{\psi}_i \ , \quad (\frac{\partial \bar{\psi}}{\partial y})_i \ , \quad -(\frac{\partial \bar{\psi}}{\partial x})_i \ \right]^T \tag{3.24}$$

The stream function in each element is approximated by

$$\bar{\psi} = \sum_{i=1}^{4} \mathbf{N}_i \mathbf{a}_i \tag{3.25}$$

where $\mathbf{N}_i$ is a vector of shape functions. Application of the method of Galerkin leads to a system of equations

$$\mathbf{Sa} = \mathbf{f} \tag{3.26}$$

where $\mathbf{S}$ is the stiffness matrix resulting from the discretization of the differential operator and $\mathbf{f}$ is the load vector, containing the contribution of the right hand side of (2.22) and of the non-homogeneous boundary conditions. The system is solved for the unknowns $\mathbf{a}$. The global matrix and vector are assembled elementwise after calculation of the element matrix

$$S_{ij}^e = \int\int_e \eta \left[\frac{\partial^2 \mathbf{N}_i}{\partial x^2} - \frac{\partial^2 \mathbf{N}_i}{\partial y^2} \right] \left[\frac{\partial^2 \mathbf{N}_j}{\partial x^2} - \frac{\partial^2 \mathbf{N}_j}{\partial y^2} \right] dxdy$$

$$+ \int\int_e 4\eta \frac{\partial^2 \mathbf{N}_i}{\partial x \partial y} \frac{\partial^2 \mathbf{N}_j}{\partial x \partial y} \ dxdy \tag{3.27}$$

and element load vector

$$\mathbf{f}_j^e = \int\int_e Ra(\Gamma)\mathbf{N}_j \frac{\partial T}{\partial x} \, dxdy - Rb\int\int_e \mathbf{N}_j \frac{\partial \Gamma}{\partial x} \, dxdy \tag{3.28}$$

We thus have 12 degrees of freedom in the element and the unknown $\bar{\psi}$ can be expanded by retaining 12 terms of a fourth order polynomial in x and y. Appendix B gives the shape functions for this element. The volume integrals in the coefficients of the stiffness matrix are calculated with the 3×3 Gaussian quadrature rule. The same integration rule is applied in the calculation of the coefficients in the first term of the element load vector

$$\int\int_e Ra(\Gamma)\mathbf{N}_j \frac{\partial T}{\partial x} \, dxdy \tag{3.29}$$

where the temperature is given in the nodal points. The temperature derivative in the Gaussian points is calculated in a way that is consistent with the linear approximation of the temperature within the element (refer appendix B).

The interface between the two fluids is represented by a marker chain with coordinates (x_m, y_m), $m = 1, \cdots, N_m$. The contribution of Γ to the element load vector is then calculated by the approximation

$$\int\int_e \mathbf{N}_j \frac{\partial \Gamma}{\partial x} \, dxdy \approx \sum_{m=2}^{N_m-1} \mathbf{N}_j(x_m, y_m) \frac{(y_{m+1} - y_{m-1})}{2} \tag{3.30}$$

[Christensen & Yuen, 1984].

Bicubic splines

In this section the use of splines in the solution of the equation of motion in the stream function formulation is considered. Bicubic splines are used to define shape functions for the method of Galerkin on a rectangular grid. A rigorous definition of the use of splines in variational methods can be found in Schultz [1973]. Kopitzke [1977] gives a technical description of the use of the method in mantle convection modelling and gives expressions for spline functions defined on non-equidistant grids. Woidt [1980] describes the use of bicubic splines for Rayleigh-Taylor instabilities. Following is a summary of the implementation of the method to solve (2.22), with $Ra \equiv 0$ and free-slip boundaries on equidistant grids. An approximate solution $\bar{\psi}$ of (2.22) can be constructed by

$$\bar{\psi}(\mathbf{x}) = \sum_{j=1}^{N} \beta_j \Psi_j(\mathbf{x}) \tag{3.31}$$

where β_j are called the spline coefficients. Main advantage of using this type of

approximate solution is that the continuity requirement of the first order derivative is satisfied (refer appendix B) at a minimum cost (= low number of degrees of freedom). Disadvantage is that the shape functions are not local (each shape function is non-zero on 16 elements), in contrast to Lagrangian types of shape functions. Another complication arises in the implementation of the boundary conditions, which cannot be treated by elimination of local shape functions, as is common in the Lagrangian approach. Instead, a space spanned by the spline shape functions that satisfies the boundary conditions must explicitly be constructed.

The rectangular geometry $\Omega = [0, L] \times [0, 1]$ can be discretized using a mesh of $N_x \times N_y$ equidistant elements. Each element has dimensions $\Delta x \times \Delta y$. An approximate solution is sought of the form (3.31) where the spline functions Ψ_j satisfy the boundary conditions. The construction of these spline functions is described in appendix B. Application of the method of Galerkin yields a matrix equation

$$\mathbf{A}\,\mathbf{x} = \mathbf{f} \tag{3.32}$$

where the matrix coefficients A_{ij} are given by

$$A_{ij} = \int\!\!\int_\Omega \eta \left[\frac{\partial^2 \Psi_i}{\partial x^2} - \frac{\partial^2 \Psi_i}{\partial y^2} \right]\left[\frac{\partial^2 \Psi_j}{\partial x^2} - \frac{\partial^2 \Psi_j}{\partial y^2} \right] dxdy$$

$$+ \int\!\!\int_\Omega 4\eta \frac{\partial^2 \Psi_i}{\partial x \partial y} \frac{\partial^2 \Psi_j}{\partial x \partial y}\, dxdy \tag{3.33}$$

The integrals in (3.33) are calculated using a 3×3 Gaussian rule. The load vector $\mathbf{f}$ is calculated by an approximation similar to (3.30)

3.6 Benchmark results

The accuracy and the efficiency of the implementations have been compared against analytical solutions and numerical results obtained by different codes for a variety of cases. The three different methods are denoted by

ε penalty function method
C1   stream function approach: non-conforming element
ψ stream function approach: bicubic splines

The quoted CPU times are in seconds and hold for the Iris Indigo workstation with a risc processor (MIPS R3000 @ 33 MHz). Inversion of a 1000×1000 matrix using the Linpack benchmark [Dongara, 1986] is performed at this machine with 3.1 Mflops (64 bit accuracy). The grid specification, as is used throughout this thesis, reflects the number of elements in an indirect way. The actual number of elements depends on the type of approximating shape functions: a grid specified as 10×10 contains 21×21 nodal points, $2 \times 10 \times 10$ quadratic triangles (penalty function method), $2 \times 20 \times 20$ linear triangles (temperature equation) and 20×20 rectangles (non-conforming element, spline method). The equation(s) of motion (in either of the three formulations described above) and the temperature equation are solved on meshes with the same distribution of nodal points. The coupling between the equations is described in appendices A and B.

3.6.1 Thermal convection benchmark

Both the penalty function method and the stream function method with the non-conforming element have been used to study thermal convection. The benchmark comparison of Blankenbach et al. [1989] defines a number of cases and best estimates for the numerical values of some derived quantities, obtained from a comparison of several finite difference, finite element, and spectral methods. Two dimensional thermal convection of a Newtonian Boussinesq fluid at infinite Prandtl number is considered. The non-dimensional equations (2.15-2.17) are solved on a rectangular domain $\Omega = [0, \lambda] \times [0, 1]$, where λ is the aspect ratio. The quantities to be derived are

i) the Nusselt number

$$Nu = -\int_0^\lambda \frac{\partial T}{\partial y}(x, y = 1)dx \ / \int_0^\lambda T(x, y = 0)dx \tag{3.34}$$

ii) the non-dimensional root-mean-squared velocity

$$v_{rms} = \frac{1}{\lambda}\left[\int_\Omega (v_2 + w^2)\, d\Omega\right]^{\frac{1}{2}} \tag{3.35}$$

and iii) the non-dimensional temperature gradient in the corners of the region Ω

$$q = -\frac{\partial T}{\partial y} \tag{3.36}$$

with $q_1 = q(0, 1)$, $q_2 = q(\lambda, 1)$, $q_3 = q(\lambda, 0)$ and $q_4 = q(0, 0)$. Grid refinements are used to improve the resolution in the boundary layers of the convecting cell.

Case 1

Stationary convection with constant viscosity in a square region ($\lambda = 1$), free-slip boundaries, constant temperature at top ($T = 0$) and bottom ($T = 1$) and reflective vertical boundaries ($\partial T/\partial x = 0$). Rayleigh number is varied between 10^4 and 10^6.

Table 3.1a   Blankenbach et al. [1989], Case 1a $Ra = 10^4$

Code	Grid	Nu	v_{rms}	q_1	q_2	cpu †
ε	20 × 20	4.8891	42.896	8.0551	0.5888	37
	30 × 30	4.8880	42.878	8.0589	0.5908	118
	40 × 40	4.8880	42.887	8.0587	0.5911	282
C1	20 × 20	4.8900	42.923	8.0563	0.5886	58
	30 × 30	4.8885	42.894	8.0596	0.5907	211
	35 × 35	4.8885	42.897	8.0590	0.5910	355
best estimate		4.8844	42.865	8.0594	0.5888	

† Cpu-time in seconds on Iris Indigo R3000 workstation (see text)

Table 3.1b   Blankenbach et al. [1989], Case 1b $Ra = 10^5$

Code	Grid	Nu	v_{rms}	q_1	q_2	cpu
ε	20 × 20	10.532	193.262	18.993	0.7181	62
	30 × 30	10.541	193.153	19.076	0.7251	162
	40 × 40	10.539	193.191	19.077	0.7264	386
C1	20 × 20	10.5351	193.407	18.990	0.71691	81
	30 × 30	10.5425	193.233	19.074	0.72438	251
	35 × 35	10.5412	193.272	19.075	0.72548	424
best estimate		10.534	193.215	19.079	0.72275	

Table 3.1c   Blankenbach et al. [1989], Case 1c $Ra = 10^6$

Code	Grid	Nu	v_{rms}	q_1	q_2	cpu
ε	20 × 20	21.852	835.331	44.419	0.8412	64
	30 × 30	21.986	834.030	45.902	0.8791	309
	40 × 40	21.986	833.985	45.948	0.8771	469
C1	20 × 20	21.861	835.703	44.561	0.83619	65
	30 × 30	21.997	834.100	45.852	0.8732	237
	35 × 35	21.998	834.316	45.902	0.8773	403
best estimate		21.972	833.990	45.964	0.8772	

Case 2

Stationary convection with temperature and depth dependent viscosity η

$$\eta = \eta_0 \exp[-bT + c(1 - y)] \tag{3.37}$$

The Rayleigh number Ra_0 is based on the viscosity η_0

$$Ra_0 = \frac{\rho \alpha g \Delta T h^3}{\kappa \eta_0} \tag{3.38}$$

Table 3.2a   Blankenbach et al. [1989], Case 2a: $\lambda = 1$, $Ra_0 = 10^4$, $b = \ln(1000)$, $c = 0$

Code	Grid	Nu	v_{rms}	q_1	q_2	q_3	q_4	cpu
ε	20×20	10.040	476.87	17.393	1.0046	25.182	0.4301	150
	30×30	10.061	478.44	17.504	1.0089	26.731	0.4955	517
	40×40	10.065	478.77	17.520	1.0109	26.905	0.5001	1379
C1	20×20	10.049	477.32	17.406	1.0025	25.284	0.4310	512
	30×30	10.065	478.49	17.509	1.0075	26.771	0.4962	2167
best estimate		10.066	480.43	17.531	1.0085	25.809	0.4974	

Table 3.2b   Blankenbach et al. [1989], Case 2b: $\lambda = 2.5$, $Ra_0 = 10^4$, $b = \ln(16384)$, $c = \ln(64)$

Code	Grid	Nu	v_{rms}	q_1	q_2	q_3	q_4	cpu
ε	32×16	6.9011	171.013	18.187	0.1791	13.756	0.5972	229
	40×20	6.9269	171.442	18.401	0.1799	14.040	0.6115	452
	48×24	6.9276	171.407	18.456	0.1799	14.113	0.6168	809
	56×28	6.9276	171.397	18.472	0.1798	14.139	0.6176	1265
C1	32×16	6.9156	171.592	18.128	0.1796	13.872	0.5984	544
	40×20	6.9396	171.828	18.372	0.1803	14.076	0.6122	1236
	48×24	6.9357	171.650	18.428	0.1802	14.122	0.6173	2422
best estimate		6.9299	171.755	18.484	0.1774	14.168	0.6177	

Case 3

Time-dependent convection with constant viscosity and internal heating. Rigid top and bottom boundary. Constant temperature at top ($T = 0$), insulated bottom ($\partial T/\partial y = 0$) and side ($\partial T/\partial x = 0$) boundaries. Aspect ratio $\lambda = 1.5$, constant heat production rate Q, and Rayleigh number

$$Ra = \frac{\alpha g Q h^5}{\kappa_0^2 \rho_0 c_p \eta_0} = 216000 \tag{3.39}$$

As initial condition the result from the stationary model with lower Rayleigh number $Ra = 21600$ is chosen. After integration of the time-dependent equations over a sufficiently long time interval, the solution becomes periodic in time with two distinct periods (P2). From the time-series of Nu and v_{rms}, the position of the extrema and the values are obtained by quadratic Lagrangian interpolation, using the three data points around each extremum.

Table 3.3   Blankenbach et al. [1989], Case 3

Code	Grid	Period	Nu				v_{rms}			
			max	min	max	min	max	min	max	min
C1	30×20	0.0489	7.367	6.44	7.19	6.77	60.8	32.2	57.6	30.2
	35×25	0.0486	7.374	6.45	7.18	6.78	60.7	32.1	57.2	30.9
best	estimate	0.0480	7.379	6.47	7.20	6.80	60.4	32.0	57.4	30.3

The penalty function method gives very similar results. The global accuracy of the method is governed by the accuracy in solving the time-dependent heat equation (2.3), which is identical for both methods.

3.6.2 Rayleigh-Taylor instability: linear stability analysis

The stream function codes have further been tested for Rayleigh-Taylor instabilities. From linear stability analysis [Chandrasekhar, 1961] it is found that the amplitude of harmonic perturbations between originally horizontal interfaces grows exponentially in time with a specific growth rate κ. The growth rate depends a.o. on the viscosity and densities of the fluids and the boundary conditions, and can be determined analytically for simple models. Consider the situation of two superimposed homogeneous fluid layers of equal thickness, contained in a rectangular geometry $\Omega = [0, 1] \times [0, 1]$ with free-slip boundaries. The fluids are isoviscous ($\eta = 1$) and have density difference $\Delta\rho = 1$. The interface between the fluids at $y = 0.5$ is perturbed by a cosinusoidal perturbation with wavelength 2 and amplitude 0.001. Table 3.4 shows the non-dimensional growth factor for this case. The numerical values are obtained using a discretization of the interface with 101 markers.

Table 3.4   Rayleigh-Taylor instability

Code	Grid	Growth rate	cpu
C1	10×10	0.05304	1.9
	20×20	0.05310	19.5
	30×30	0.05312	85
ψ	2×2	0.05295	0.14
	5×5	0.053118	2.4
	10×10	0.053121	12.8
Analytical		0.0531307	

3.7   Conclusions

From the above results we can conclude that the codes for thermal convection are very accurate: all derived quantities, even for the coarse grids, fall within 0.5 % of the 'best estimates' quoted in Blankenbach et al. [1989]. Results obtained with the non-conforming element and with the penalty function method compare very well. The non-conforming element is about 50 % more expensive with regard to memory and cpu requirements. The spline method shows to be accurate even at very coarse grids. For a given accuracy, the use of splines is much more efficient than using the non-conforming element. A further comparison of the methods is given in the next chapter, in which the application of the methods to Rayleigh-Taylor instabilities is discussed.

Chapter 4

Numerical modelling of Rayleigh-Taylor instabilities

4.1 Introduction

A prominent example of flow of crustal rocks driven mainly by compositional buoyancy is found in salt diapirism. Rocksalt is nearly incompressible and maintains its relatively low density under high pressures. After deposition of the salt in evaporite basins and subsequent burial by increasingly denser sediment, a density inversion can occur which may lead to the formation of salt domes. The large economical interests, associated with hydrocarbon trapping and long term storage of radioactive waste and energy reserves, have lead to an extensive study of the dynamics of salt dome formation, using analytical methods [Hunsche, 1977; Ramberg, 1981], experimental approaches [Whitehead & Luther, 1975; Talbot, 1977; Jackson et al., 1990], and numerical modelling [Berner et al., 1972; Woidt, 1978; Schmeling, 1987]. In both the analytical and numerical approaches, the mathematical model has been used of a Rayleigh-Taylor instability - a gravitational instability of a layer of heavy fluid overlying a lighter one [Chandrasekhar, 1961].

In this chapter some technical aspects of the numerical modelling of Rayleigh-Taylor instabilities will be discussed. The quality of the numerical study of this model depends strongly on the approximation of viscosity and density. The discontinuity of these properties across the interface between the two fluids makes this a non-trivial task.

4.2 Implementation of buoyancy forces

In the stream function methods (chapter 3), the interface is represented by a discrete chain of markers. The elements of the load vector are defined by the integral expression (3.28) (with $Ra = 0$), which for a given distribution of markers can efficiently be calculated by the simple summation (3.30). Table 3.4 of chapter 3 shows the high accuracy that can be obtained. Implementation of the marker chain method is more complicated within the penalty function approach. The element load vector is then given by (refer 3.15d)

$$f_i^e = \int\limits_e \rho g \phi_i \, de \tag{4.1}$$

Calculation of the integral is difficult to perform accurately in elements through which the marker chain passes. A more natural approach is to represent the interface by element boundaries and create a new mesh at each step. The success of this Lagrangian approach depends strongly on the intelligence of the mesh generator. At large deformations the automatic mesh generation can fail, but regular geometries, such as the relatively simple domal shapes, can be handled without problems.

$\Delta x = 0.1$ $\Delta x = 0.06$ $\Delta x = 0.04$ $\Delta x = 0.02$
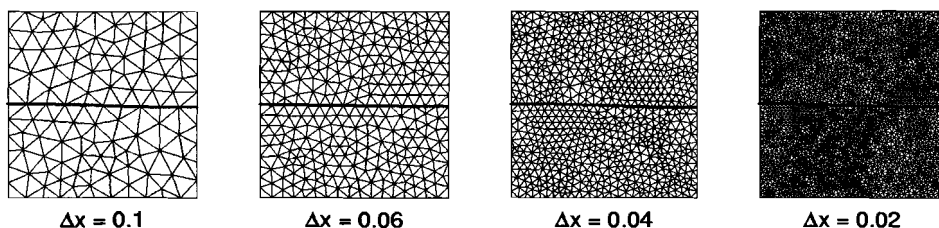
Figure 4.1 *Initial configuration used in the Lagrangian approach for decreasing typical element size Δx.*

The accuracy of the Lagrangian method can be tested by determining the growth rate of a perturbation on an initially horizontal interface. From linear stability analysis an analytical solution can be obtained for this case. Figure 4.1 shows the initial mesh configurations for a Rayleigh-Taylor instability of two layers of equal thickness $h = 0.5$. In this and following models all physical quantities are non-dimensional. The grids are characterized by the typical size of an element boundary Δx. Table 4.1 shows the accuracy of this method in determining the growth rate κ for a model with density contrast $\Delta \rho = 1$, free-slip boundaries and constant viscosity $\eta = 1$. The initially horizontal interface (shown by the thick solid line) is perturbed by a harmonic with wavelength 2 and amplitude 0.01 (compare table 3.4).

Table 4.1   Rayleigh-Taylor instability

Δx	growth rate	cpu
$\Delta x = 0.1$	0.05272	2
$\Delta x = 0.06$	0.05295	8
$\Delta x = 0.04$	0.05302	38
$\Delta x = 0.02$	0.05309	512
Analytical	0.05313	

4.3 Isoviscous models

Figure 4.2 displays the development of the finite element mesh for the Rayleigh-Taylor instability described above. The interface is advanced using the predictor-corrector method described in chapter 3. After each time step the nodal points along the interface and at the vertical boundaries are repositioned to maintain a approximate element size $\Delta x = 0.06$. The mesh is regenerated for each solution of the Stokes equation. At dimensionless time $t = 100$, the interface nearly reaches the top and bottom boundary of the domain. If it would be allowed to reach the boundary the nodal points describing the upper and lower boundary of each fluid layer would overlap and the mesh would become ill-defined. At least one element row is maintained between the top and bottom boundary of the domain and the interface. The vertical size of the element row is kept finite (≥ 0.01) to avoid

| t = 40 | t = 100 | t = 160 | t = 220 |
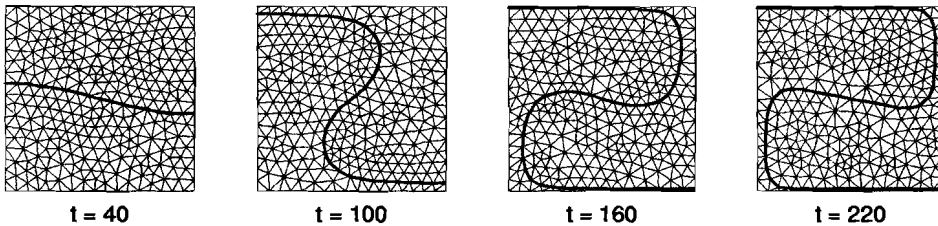
Figure 4.2 *Development of an isoviscous ($\eta = 1$) Rayleigh-Taylor instability with free-slip boundaries, modelled with the Lagrangian approach, $\Delta x = 0.06$. Density difference between the layers is $\Delta \rho = 1$.*

ψ 10x10
c1 10x10

| t = 40 | t = 100 | t = 160 | t = 220 |
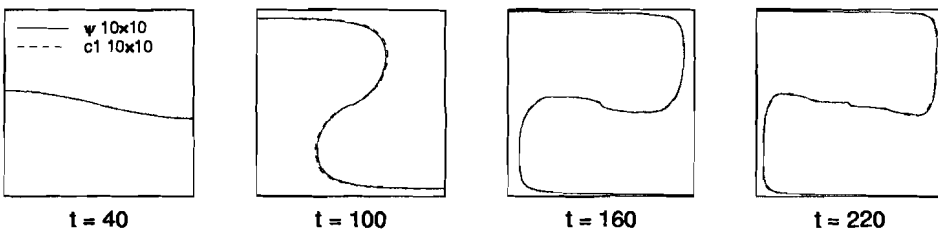
Figure 4.3 *Same as figure 4.2, now modelled using the stream function formulation. ψ indicates the spline method, C1 the method using the non-conforming element.*

numerical errors as a consequence of a large element aspect ratio [Cuvelier et al., 1986].

Figure 4.3 shows the evolution of the interface between the fluids for the same Rayleigh-Taylor model, calculated using the marker chain method in the stream function formulation, using both bicubic splines (denoted by ψ) and the non-conforming element (C1) (for grid specification refer chapter 3). The marker chain is regridded at each time step to maintain an approximate distance between the markers of 0.002.

Figure 4.4 compares the development the height of the diapir h and the root-mean-squared velocity v_{rms} (3.35) for the marker chain method and the Lagrangian approach.
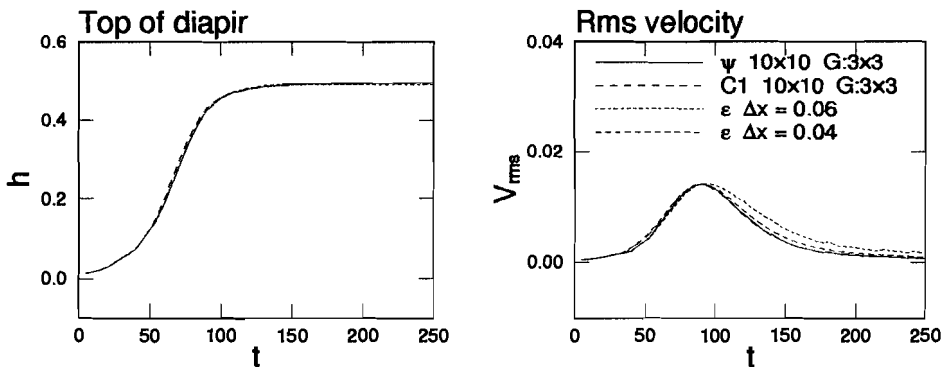
Figure 4.4 *Comparison of the three methods. ε denotes the Lagrangian approach. The use of a 3 × 3 Gaussian quadrature rule is indicated by G:3 × 3.*

Both marker chain methods compare very well. For these isoviscous models the relative coarse grid suffices to calculate the global evolution of the model. In figure 4.3 some small oscillations in the interface are visible at $t = 220$ which is mainly a consequence of the larger relative error in calculating the velocity components from the stream function in the stagnation zone. The marker chain method makes it possible to use a fine discretization of the interface. In the Lagrangian approach it is necessarily coarser and this makes the implementation of the buoyancy forces less accurate. This can be observed when comparing the graphs of v_{rms} in figure 4.4 and the snapshots at $t = 100$ in figure 4.2 and 4.3. This error can be reduced by decreasing the average element size at the cost of much higher computational effort. Figure 4.4 compares v_{rms} calculated using an average element size $\Delta x = 0.04$ with the other models.

The spline method is faster by a factor 3 compared to the non-conforming element method for the problem described above. Both methods are much faster than

the Lagrangian approach, where at each step the mesh has to be regridded and the discretized matrix equation has to be constructed again. In both marker chain methods the finite element mesh and the viscosity distribution are stationary in time and this makes it possible to construct the stiffness matrix only once, and store the decomposed form of the matrix in memory. The discretized Stokes equation can then efficiently be solved by back-substitution. This disadvantage of the Lagrangian approach, with respect to the stream function methods, disappears in the modelling of non-isoviscous flows, where the stiffness matrix has to be constructed at every step, irrespective of the employed method.

4.4 Newtonian models with variable viscosity

A more realistic model for salt diapirism is a Rayleigh-Taylor instability where the upper layer, representing the sediment, has a higher viscosity than the underlying (salt) layer. Traditionally a viscosity contrast of 30-100 has been used [Hunsche, 1977; Woidt, 1978; Roemer & Neugebauer, 1991]. In the Lagrangian approach the discontinuity in the viscosity coincides with the element boundaries representing the interface between the fluids. The viscosity is constant in each element. In the stream function approaches the integrals (3.27) and (3.33) are difficult to calculate accurately in elements in which the viscosity is discontinuous. Using standard Gaussian integration (with 3×3 Gaussian points), the viscosity discontinuity is not well resolved. Woidt [1980] uses an 8×8 Gaussian rule within those elements to improve on this. It is questionable whether this computationally expensive method is necessary for purely Newtonian flows. Local changes in the viscosity distribution will not have a strong influence on the large scale flow, as can be seen from the rise of small 'Stokes' droplets through a viscous medium. The drag exerted on the droplet which is only a function of radius, velocity and viscosity of the surrounding fluid [Batchelor, 1967]. The viscosity of the droplet itself is not important in determining the speed with which it rises. The use of Gaussian integration in calculating the element integrals effectively diffuses the discontinuity over a length scale that is determined by the spacing between the Gaussian points. Using a higher Gaussian rule will decrease the spacing and improve the resolution of the discontinuity, but, as will be shown in the following example, this has not a distinguishable effect on the dynamics of the Rayleigh-Taylor instability.

Figures 4.5-4.7 compare the evolution of a model with two homogeneous fluid layers with different density and viscosity. Initial perturbation is a harmonic with wavelength 2 and amplitude 0.01. The viscosity of the upper layer is $\eta_1 = 100$, the lower layer has viscosity $\eta_2 = 1$. Figure 4.5 shows snapshots of the mesh in the Lagrangian approach with $\Delta x = 0.04$. Figure 4.6 shows the development calculated by the spline method (using both a 3×3 and 8×8 Gaussian rule), in
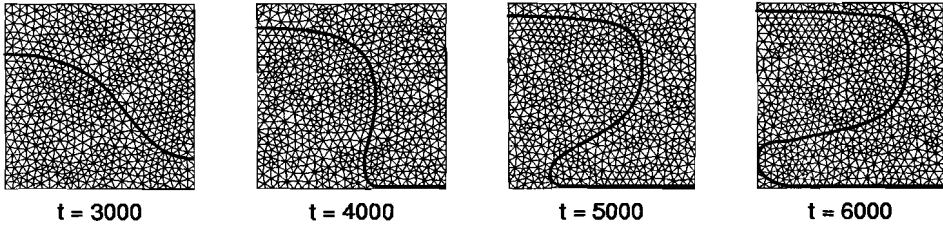
Figure 4.5 *Development of a non-isoviscous Newtonian RT instability with free-slip bound-aries, as modelled by the Lagrangian approach* $(\Delta x = 0.04)$. *The density difference is* $\Delta\rho = 1$, *viscosity of the upper layer is* $\eta_1 = 100$, *and the viscosity of the lower layer* $\eta_2 = 1$.
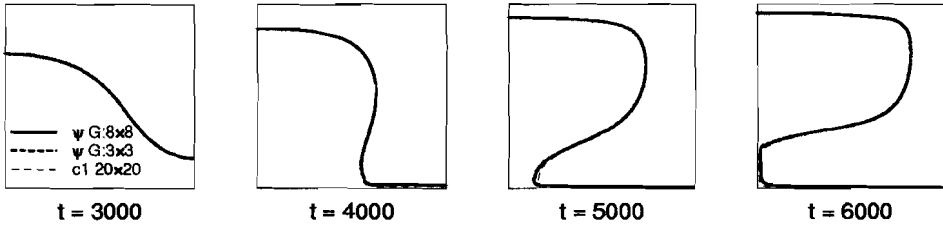

Figure 4.6 *Comparison of development of RT instability (model parameters as in figure 4.5) calculated by the spline method* (ψ, *grid* 10×10) *with* 3×3 *and* 8×8 *Gaussian quadrature rules and the method with the non-conforming element (C1, grid 20×20)).*
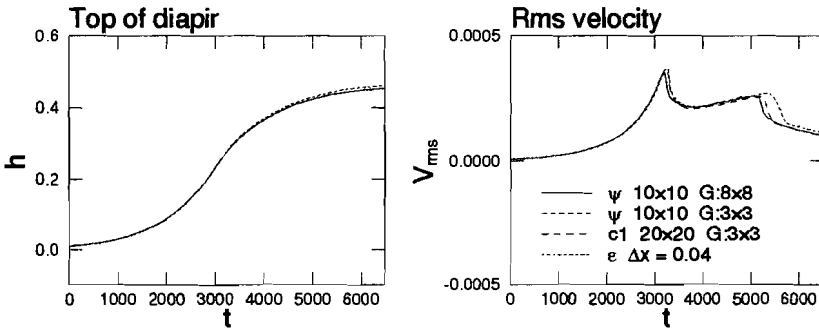
Figure 4.7 *Comparison of the three methods in calculating h and* v_{rms}.

comparison to the result obtained by using the non-conforming element $(3 \times 3$ Gaussian quadrature). h and v_{rms} are displayed in figure 4.7. The rms velocity has

two distinct peaks at $t \approx 3000$ and $t \approx 5200$, which are correlated to reorganizations in the flow pattern, when the interface between the fluids 'feels' the influence of first the lower boundary and next the side boundary. The Lagrangian approach predicts a development that is, as has been observed in the purely Newtonian case (figure 4.4), a little slower than that predicted by the stream function methods, but the difference is small.

The second invariant of the strain rate tensor $\dot\varepsilon$ is the main parameter determining the power law viscosity (2.11). In the models used in this section, the viscosity is discontinuous across the interface between the fluids. As surface tension effects can be neglected, both the normal and shear stress have to be continuous across the interface. In general this leads to discontinuous components of the strain rate tensor and discontinuous $\dot\varepsilon$. In the Lagrangian approach this discontinuity will be resolved accurately, as the interface coincides with element boundaries, across which the derivatives of the velocity shape functions are not necessarily continuous.

In both stream function methods $\dot\varepsilon$ is continuous within the elements and the use of bicubic splines even guarantees continuity of $\dot\varepsilon$ across element boundaries. As will be shown below the continuous approximation to $\dot\varepsilon$ leads to spatial
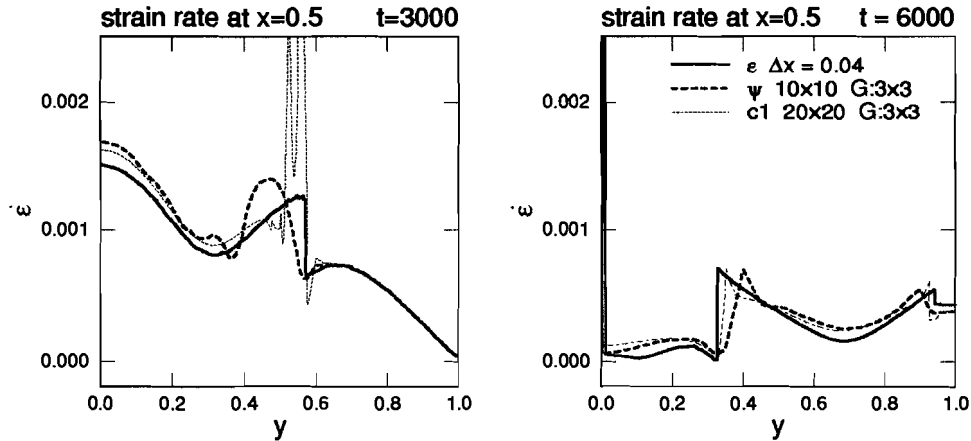
Figure 4.8 *Strain rate $\dot\varepsilon$ at $x = 0.5$ calculated by the three methods for the Newtonian model with homogeneous layers of different viscosity. The discontinuity in strain rate at the interface between the fluid is only well resolved by the Lagrangian approach (ε).*

oscillations that depend on element size and accuracy of the numerical integration. For a power law creep model this will have a strong effect on the viscosity distribution around the interface between the fluids.

Figure 4.8 displays the value of $\dot{\varepsilon}$ at a cross-section through the model at $x = 0.5$ for the three methods at times $t = 3000$ and $t = 6000$ (compare figure 4.6). The heavy solid line displays $\dot{\varepsilon}$ calculated from the Lagrangian approach, showing the discontinuities at the interface at $y = 0.56$ ($t = 3000$), $y = 0.35$ and $y = 0.95$ ($t = 6000$). The spline method (heavy dashed line) gives a continuous approximation, which oscillates in the layer with the lowest viscosity. As a consequence of the relatively coarse discretization (19×19 spline coefficients are used) each spline has a broad basis, and a large part of the medium is influenced by the induced oscillations. The results obtained with the non-conforming element (calculated at a finer grid) show sharp and short wavelength oscillations, again in the layer with the lower viscosity.

Figure 4.9a shows the effect of grid refinement on the results of the spline method, compared with the Lagrangian approach. The mesh indicated with 20×20 results in 39×39 unknown spline coefficients. Figure 4.9b displays results obtained for $t = 3000$ with a more accurate calculation of the integrals in the
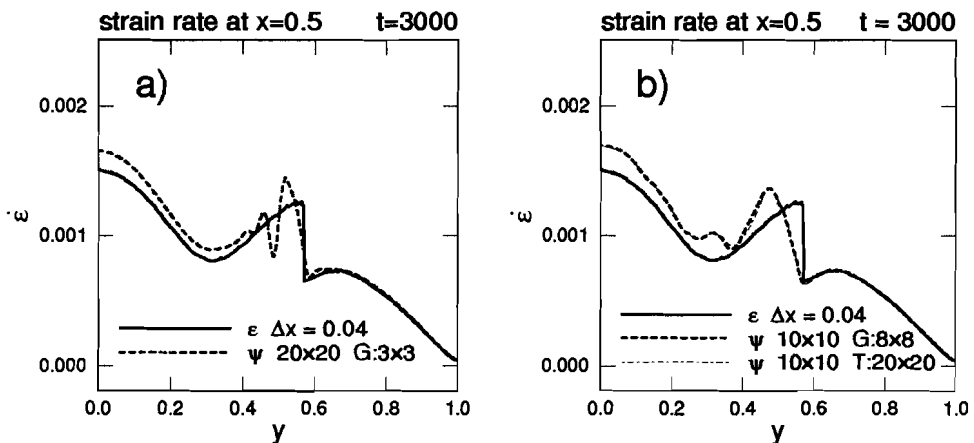
Figure 4.9 *Compare figure 4.8. a) Influence of increasing the number of elements in the spline method ψ b) Influence of calculating the element integrals in the stiffness matrix in the element in which the marker chain lies using an 8×8 Gaussian rule and a trapezoid rule using 20×20 points within the element.*

coefficients of the stiffness matrix (3.33). In the elements in which the viscosity is discontinuous, the integral is approximated by either an 8×8 Gaussian quadrature rule (heavy dash), or a 20×20 trapezoidal rule (light dash-dot). Both methods improve the solution slightly, by decreasing the amplitude of the oscillations. However, it is clear from the above experiments, that the inability of the employed shape functions to model the discontinuous strain rate function is the main reason for the occurrence of the oscillations.

4.5 Non-Newtonian flows

To illustrate the effects of the oscillatory $\dot{\varepsilon}$ in non-Newtonian flows, some experiments are performed with strain rate weakening power law creep model

$$\eta = A^{-1/n} \dot{\varepsilon}^{\frac{1-n}{n}} \qquad n > 1 \tag{4.2}$$

The non-linear equations of motion are solved by Picard sub-iteration. The strain rate $\dot{\varepsilon}$ within an element can be expressed as a function of the velocity components in the nodal points using the analytical expressions of the derivatives of the shape functions (see appendix A and B).

In the first non-Newtonian model to be considered the material properties A and n are constant throughout the medium. Figure 4.10 shows the snapshots of
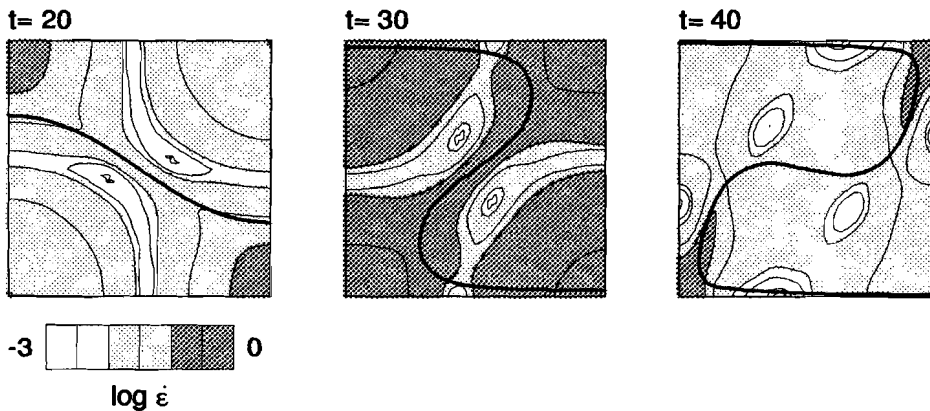
Figure 4.10 *Snapshots of the interface and the strain rate $\dot{\varepsilon}$ for a non-Newtonian RT instability. $A = 1$ and $n = 3$ in both layers.*

$\log \dot{\varepsilon}$ and the interface for a model with $A = 0.1$ and $n = 3$, calculated by the spline method with mesh 15×15. Initial amplitude of the harmonical perturbation is 0.1.

Figure 4.11 compares the top of diapir (h), rms velocity (v_{rms}), and the minimum (η_{min}), maximum (η_{max}), and volume averaged (η_{av}) viscosity calculated by the spline method (ψ) and the Lagrangian approach (ε). Once the interface reaches sufficient amplitude the effective viscosity decreases sharply and the diapir moves fast. The rapid overturn creates the sharp peak visible in the rms velocity. η_{min} and η_{av} are smooth functions of time and show a clear minimum during the overturn. The coarser interface discretization is again the reason for slower development of the model in the Lagrangian approach, but the time lag is small and otherwise the approaches compare quantitatively very well. The maximum viscosity η_{max} is determined by the local strain rate minima in the stagnation points (or rather stagnation zones; figure 4.10). The value of the strain rate in these points is clearly not well defined, but as the amount of deformation is negligible here, the actual value of the viscosity is not very important. The erratic behaviour of the maximum viscosity has been observed previously in time-dependent thermal convection models using the penalty function formulation [Van den Berg et al., 1993]. It shows that η_{max} cannot be used as a good indicator of the dynamical behaviour of the models.

An interesting class of models comprises those with material parameters that are discontinuous across the interface. Consider a dense Newtonian layer overlying a lighter non-Newtonian one. The discontinuity in the creep law induces a viscosity discontinuity and consequently oscillations in the strain rate $\dot{\varepsilon}$ if the marker chain method is employed (section 4.4). The oscillations in $\dot{\varepsilon}$ have a strong influence on the viscosity distribution in the non-Newtonian layer and it has to be investigated whether the marker chain method can still be used for this class of models. Following examples are calculated with the Lagrangian approach and the spline
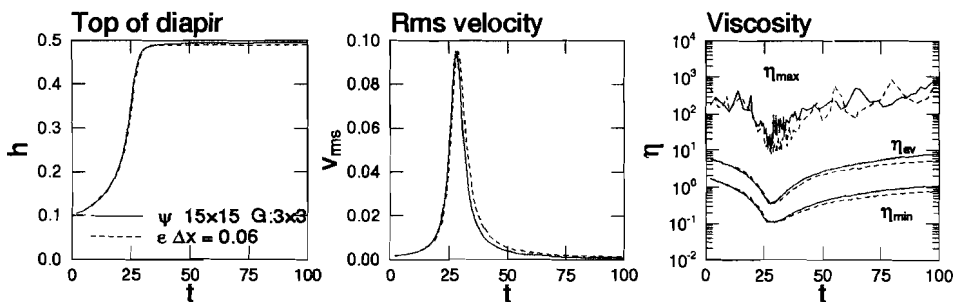

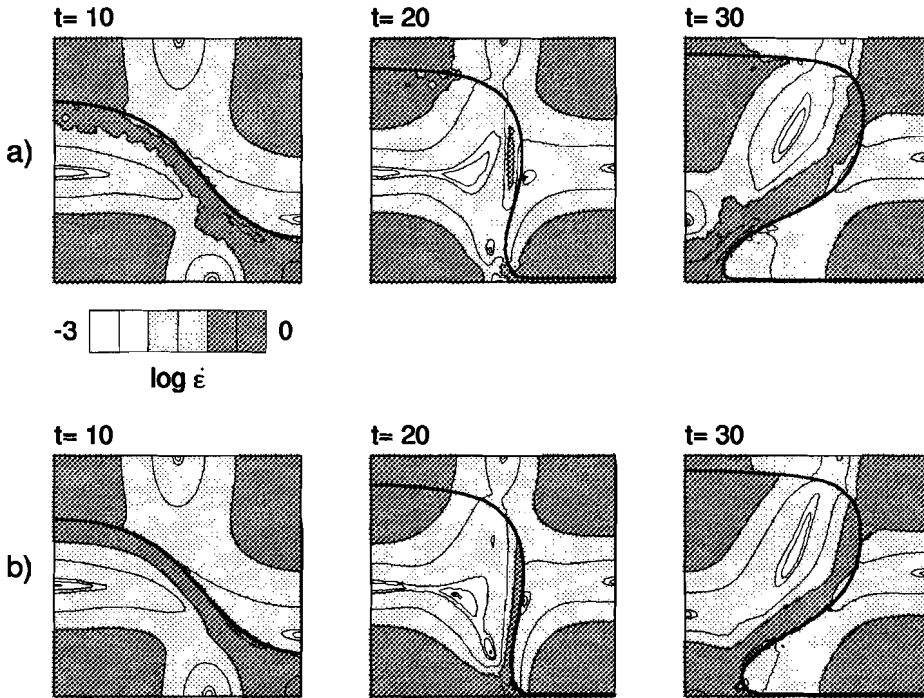**Figure 4.11** *Development of h and v_{rms} for the non-Newtonian model.*

Figure 4.12 *Development of a RT instability with Newtonian rheology in the upper layer (A = n = 1 and non-Newtonian in the lower layer (A = 0.01 , n = 3). The oscillations in strain rate ε̇ that are induced by the approximation of the interface in the spline method (top row) are absent in the Lagrangian approach (bottom row).*

method. The other marker chain method behaves qualitatively in a similar way as the spline method. The conclusions that are made hold equally for both marker chain methods.

Figure 4.12 shows snapshots of the interface and ε̇ for a model with Newtonian upper layer ($A = 1$, $n = 1$) and non-Newtonian lower layer ($A = 0.01$, $n = 3$). Other model parameters are as in the previous model. Some derived quantities are plotted in Figure 4.13. The results displayed in the top row (Fig. 4.12a) are calculated using the spline method (grid 15×15). The oscillations close to the interface resulting from the use of the marker chain method are clearly visible. The wavelength of the oscillations is determined by the grid spacing, the amplitude depends on the amplitude of the nearby viscosity discontinuity. In the areas where low strain rates prevail the viscosity discontinuity is largest.
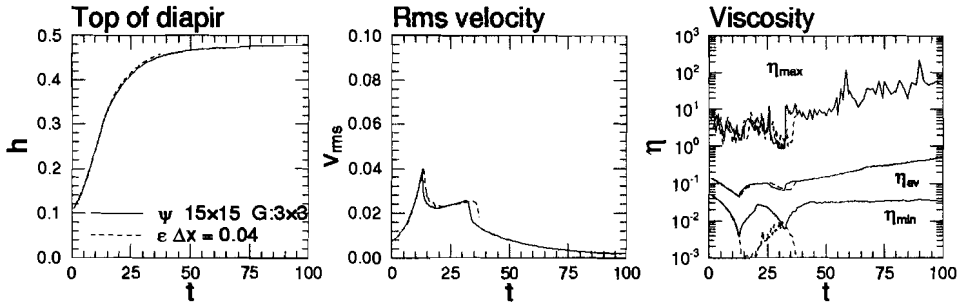
Figure 4.13 *Development of h, v_{rms} and η for the mixed Newtonian/non-Newtonian model, comparing the spline method (ψ) and the Lagrangian approach (ε).*

The results obtained using the Lagrangian approach ($\Delta x = 0.04$) are shown in Fig. 4.12b. The discontinuity in $\dot\varepsilon$ is well resolved and oscillations of the sort that are visible in figure 4.12a do not occur.

In figure 4.13 the position of the top of diapir h, rms velocity v_{rms}, and the viscosity η in the lower layer are plotted as function of time. h and v_{rms} are similar in both calculations, except for the - expected - time lag induced by the Lagrangian approach. At $t \approx 13$ the viscosity is minimal in the lower right hand side corner where the lower layer is squeezed away from the right hand side boundary. In the thin row of elements that is maintained between the interface and the lower boundary the calculation of the strain rate is not very accurate and its value is generally overestimated (compare e.g. figure 4.8b, near $y = 0$). Locally, this induces the exaggerated viscosity minimum, that is visible in figure 4.13. The viscosity contrast across the interface (that is now time and position dependent) is moderate in the above model (on the average around 10×, compare figure 4.13). Some models have been examined with higher contrasts. Those displayed stronger oscillations in $\dot\varepsilon$ and η when using the marker chain method. Methods to smooth the oscillations have been examined, but these showed to have negligible effect on the dynamics of the Rayleigh-Taylor instability. However, it cannot be excluded, that in situations with strong viscosity contrasts and a highly non-linear rheology the numerical oscillations in the viscosity field can play a role in governing the dynamics of the model and that the Lagrangian approach might be essential in obtaining a reasonably accurate solution to the problem.

From a computational point of view the spline method is the most efficient, with respect to both computer time and memory. In the example above with free-slip boundaries and grid 15×15) there are $29 \times 29 = 841$ degrees of freedom (the spline coefficients). The matrix has a bandwidth of $3 \times 29 + 3$ (refer appendix B)

and requires approximately 600 Kbyte of core memory. Calculation of the matrix coefficients is by far the computationally most expensive task in the solution process, because of the complicated expressions (3.33). Construction of the matrix and solution of the discretized system of equations takes 11 seconds on a Iris Indigo workstation. On the same grid there are 2463 unknowns in the C1-method. The matrix can be stored in 2 Mbyte. The solution of the system takes 9 seconds, just a little faster than the spline method, but it should be stressed that for approximately the same accuracy the C1 method needs more elements. In the Lagrangian approach with $\Delta x = 0.04$ there are 5508 unknowns and the matrix storage requires approximately 4.7 Mbyte. The solution of the system takes 30 seconds. A further disadvantage of the Lagrangian method is that convergence of the Picard iteration to solve the equation of motion for non-linear rheology is slow. It takes about 2 × the number of iterations compared with both stream function methods.

4.6 Conclusions

The two stream function methods described in chapter 3 and a Lagrangian approach using the penalty function formulation have been considered to model Rayleigh-Taylor instabilities. The density discontinuity is most accurately approximated by the marker chain method; the spline method is the most efficient of the two stream function methods. The necessarily much coarser discretization of the interface in the Lagrangian approach leads in the considered models to a slower development of the instability. Rheological discontinuities are most accurately approximated by the Lagrangian approach. In general the strain rate is discontinuous across the interface and this cannot accurately be modelled by the continuous low order approximation of both stream function methods, leading to oscillations in the strain rate field and (in case of non-Newtonian flows) in the viscosity field. The wavelength of the oscillations depend on the grid spacing and its amplitude on the grid spacing, the viscosity contrast across the interface, and the accuracy of the calculation of the coefficients of element matrices in elements in which the viscosity is discontinuous. For moderate viscosity contrasts and power law indices the dynamical behaviour of the Rayleigh-Taylor instability is modelled accurately by the stream function methods, as is seen from direct comparison of geometry, rms velocity and viscosity between the three methods. Use of the spline method is favourable from a computational point of view.

Chapter 5

The effective viscosity of rocksalt: implementation of steady-state creep laws in numerical models of salt diapirism †

P.E. van Keken, C.J. Spiers, A.P. van den Berg and E.J. Muyzert.

Abstract

A steady-state creep law for rocksalt, describing the two parallel mechanisms of dislocation creep and fluid-enhanced grain-boundary diffusion creep, has been used in numerical models of salt diapirism, to study the effective viscosity of rocksalt. Typical models included a 3 km thick sedimentary layer on top of 1 km of rocksalt. The grain size of the salt has been varied between 0.5-3 cm and the geothermal gradient between 25-35 K/km. For strain rates of $10^{-12} - 10^{-15}$ s^{-1}, typical of salt diapirism driven by buoyancy alone, the diffusion creep mechanism dominates at the fine grain sizes, with dislocation creep becoming important in coarsely grained salt. The effective viscosity ranges from 10^{17} Pa · s for small grain size and high temperature salt to 10^{20} Pa · s for large grain size and low temperature salt. The viscosity is strongly dependent on grain size and moderately dependent on temperature. For the larger grain sizes, the dislocation creep mechanism is most effective during the diapiric stage, but the non-Newtonian effects in the salt are not important in determining the growth rate and geometry of the diapirs. The estimates for the Newtonian viscosity of salt that have traditionally been used in modelling of salt dynamics are at the lower end of the range that we find from these numerical experiments.

5.1 Introduction

Dynamical studies of salt tectonics have received renewed attention in the last few years. This has been stimulated by research into the question of radioactive waste disposal in salt formations, and by interest in modelling the role of halokinesis in controlling the migration and trapping of hydrocarbons in rapidly subsiding basins of the type exemplified by the Gulf of Mexico.

Traditionally, salt diapirism has been studied numerically using Rayleigh-Taylor type models, describing the gravitational instability of fluid layers [Woidt, 1978; Schmeling, 1987; Roemer & Neugebauer, 1991]. These models have been extended to include several factors and relevant mechanisms, such as the effects of topography [Poliakov & Podladchikov, 1992], erosion and sedimentation [Poliakov et al., 1993], and tectonic extension and compression [Daudré et al., 1992]. However, in almost all of these studies, a Newtonian rheology, with a temperature-independent viscosity ranging between 10^{17} and 10^{18} Pa $\cdot$ s, was used to model the behaviour of the salt. Thus, the complicated rheological behaviour observed in deformation experiments on salt has been largely neglected hitherto, as has the brittle/frictional rheology, characteristic of most sedimentary overburden [Kirby & Kronenberg, 1987].

An extensive body of experimental data available on salt indicates that both dislocation [e.g., Carter & Hansen, 1983; Wawersik & Zeuch, 1986] and diffusional creep mechanisms [Urai et al., 1986; Spiers et al., 1990] can be important in salt under geological conditions. In this paper, we follow the approach used by Spiers et al. [1989, 1990], to develop a steady-state creep equation for natural rocksalt, based on parallel operation of dislocation creep plus fluid-enhanced grain-boundary diffusional or "pressure solution" creep. We have used this creep law to conduct a systematic study of the dependence of the viscosity of rocksalt on variables such as temperature and grain size, and we have implemented the creep law in numerical, Rayleigh-Taylor type models of salt diapirism. For computational simplicity and for purposes of comparison, we follow previous numerical studies in assuming a Newtonian rheology for the sediments overlying the salt. The present paper thus represents only a first step towards incorporating realistic rheologies into the numerical modelling of salt diapirism.

5.2 Creep behaviour of rocksalt at 20-200 °C

Deformation Mechanisms Observed in Experiments

Natural salt flow or halokinesis generally occurs at shallow crustal levels where temperatures are relatively low, i.e. less than 150-200 °C [e.g., Heard, 1972; Jackson & Talbot, 1986]. In order to understand the steady-state creep behaviour of

rocksalt under such conditions, numerous experiments have been conducted in recent years, on a wide variety of natural salts [e.g., Carter & Hansen, 1983; Wawersik & Zeuch, 1986; Horseman & Handin, 1990]. Conditions investigated cover temperatures in the range 20-200 °C, strain rates down to 10^{-10} s^{-1} and confining pressures typically up to 30 MPa. At experimental flow stresses below ~ 15 MPa and strain rates below ~ 10^{-7}s^{-1} (i.e., at conditions most closely approaching nature), it is generally agreed that these experiments show flow by dislocation creep [see Carter & Hansen 1983; Wawersik & Zeuch 1986]. With regard to the rate-controlling mechanism, Wawersik & Zeuch [1986] and Skrotzki & Haasen [1988] use mechanical and microstructural data to argue that the main rate-controlling process at 20-200 °C is probably cross-slip of screw dislocations. On the other hand, Carter & Hansen [1983] observed subgrain development at 100-200 °C, suggesting that dislocation climb might be rate-controlling in this range. Most recently, Carter and co-workers [Horseman et al., 1992; Carter et al., 1992] have presented mechanical and microstructural data for Avery Island salt, which suggest that creep at 50-200 °C may by controlled by cross-slip at high strain rates (> 10^{-7} to 10^{-9} s^{-1}) and by climb at lower rates. Thus, the question of detailed rate-controlling mechanism remains unclear. Fortunately, however, most salts show rather similar creep behaviour in the range 20-200 °C, and a variety of empirical power law and other creep equations are available which adequately describe the observed flow behaviour [see Carter & Hansen 1983; Wawersik & Zeuch 1986; Carter et al. 1992]. These have been widely adopted to model the creep of salt in nature [Carter et al., 1990, 1992].

In addition to the dislocation mechanism(s) discussed above, recent experiments on fine grained (dynamically recrystallized), natural rocksalt and fine grained, synthetic salt have demonstrated that when trace amounts (e.g. ≥ 0.05 wt%) of water are present at grain boundaries (as is almost always the case in natural rocksalt), deformation can occur by fluid-assisted grain-boundary diffusional creep or pressure solution [see Spiers et al., 1986, 1988; Urai et al., 1986]. This grain size sensitive, Newtonian creep mechanism involves dissolution of material at grain boundaries under high mean normal stress, diffusion through the grain-boundary fluid, and precipitation at grain boundaries under low mean normal stress. The constitutive behaviour associated with the mechanism has been investigated in detail by Spiers et al. [1990] and suggests that for the water contents and coarse grain sizes characteristic of most rocksalts, the mechanism will not be observed in laboratory experiments, but may contribute significantly to natural deformation.

Two-Mechanism Creep Law for Salt

We now follow the approach adopted by Spiers et al. [1989, 1990; see also Carter et al., 1990, 1992] to develop a creep "law" and deformation map for the flow of rocksalt under natural conditions. Assuming that the relevant mechanisms are those discussed above, and noting that dislocation and diffusion creep processes are parallel mechanisms, we can write the total steady-state creep rate for rocksalt as

$$\dot{\varepsilon} = \dot{\varepsilon}_{ps} + \dot{\varepsilon}_{dc} \tag{5.1}$$

where $\dot{\varepsilon}_{ps}$ and $\dot{\varepsilon}_{dc}$ are the strain rate contributions provided by pressure-solution and dislocation creep respectively. For the strain rate due to pressure solution we use the constitutive equation determined by Spiers et al. [1990]. This is written

$$\dot{\varepsilon}_{ps,l} = 6.95 V_m \cdot 10^{-15} \cdot \frac{\exp[-24530/RT]}{T} \cdot \frac{\sigma_l}{d^3} \tag{5.2}$$

where the various terms appearing are defined in Table 5.1.

Table 5.1   Definition of physical quantities occurring in equations (5.2) and (5.3)

Symbol	Definition	Units
d	grain size	m
R	gas constant (8.314)	$Jmol^{-1}K^{-1}$
V_m	molar volume of solid phase (2.693×10^{-5})	$m^3 \cdot mol^{-1}$
T	absolute temperature	K
σ_l	differential stress	Pa
Qcs	Activation energy for cross-slip controlled creep	$Jmol^{-1}$
μ	average shear modulus	Pa
τ_0	flow stress at absolute zero	Pa
μ_0	average shear modulus at absolute zero (14×10^9)	Pa
$\dot{\varepsilon}_{dc,l}$	Axial strain rate associated with dislocation creep	s^{-1}
$\dot{\varepsilon}_{ps,l}$	Axial strain rate associated with pressure-solution creep	s^{-1}
σ_l	Axial differential stress	Pa

For the strain rate due to dislocation creep we use the cross-slip based creep equation of Wawersik & Zeuch [1986] fitted to creep data for rocksalts from both West Hackberry (U.S.A.) and Asse (F.R.G.). This is written

$$\dot{\varepsilon}_{dc,l} = D \exp \left\{ -Q_{cs} \left[\ln \frac{\tau_0}{\mu_0} - \ln \frac{\sigma_l}{\mu} \right] \right\} \tag{5.3}$$

where the terms appearing are again defined in Table 5.1, and where the constitutive parameters Q_{cs}, τ_0/μ_0 and D for the W. Hackberry and Asse salts are listed in table 5.2.

Table 5.2 Dislocation creep parameters for Asse and West Hackberry salt
[After Wawerzik & Zeuch, 1986]

File	Origin	ln D (s^{-1})	Q_{cs} (kJmol^{-1})	τ_0/μ_0
BGRC1	Asse (FRG)	7.92	18.96	0.074
WH2	West Hackberry (USA)	1.63	14.02	0.060

Note that our choice of the latter creep equation (5.3) is not based on any particular view regarding the rate-controlling mechanism for dislocation creep in rocksalt at 20-200 °C, since this is clearly still open to question. Rather, we chose the Wawersik & Zeuch law because i) the range of parameters given for the W. Hackberry and Asse salts encompasses the behaviour of most salts tested in the range 20-200 °C, and ii) the parameters given for W. Hackberry salt yield a creep law which is closely similar to the widely used power law creep equation obtained by Carter & Hansen [1983]. Thus, the Wawersik & Zeuch law provides a convenient empirical description expected to embody the main elements of the dislocation creep behaviour exhibited by salt at temperatures below 200 °C. Some uncertainty exists in extrapolating the law to slow natural strain rates, but the same criticism applies to all creep equations presently available.

The above creep law given by equations (5.1), (5.2) and (5.3) now enables us to construct a deformation map for natural salt (grain size 1 cm), incorporating the two mechanisms considered. The result is identical to that obtained by Spiers et al. [1990] and is shown in Figure 5.1. From this diagram, and taking into account the variability of grain size in natural salts, it can be expected that deformation at natural rates should be dominated by pressure solution in fine grained salts and dislocation creep in coarse grained salts, thus spanning the transition.

5.3   The effective shear viscosity of rocksalt

We now derive expressions for the shear viscosity of rocksalt associated with pure dislocation creep, pure pressure solution, and simultaneous operation of the two mechanisms. The influence of strain rate, grain size, temperature and salt type on total viscosity is then considered.

Viscosity associated with dislocation creep

We begin by rewriting (5.3) as
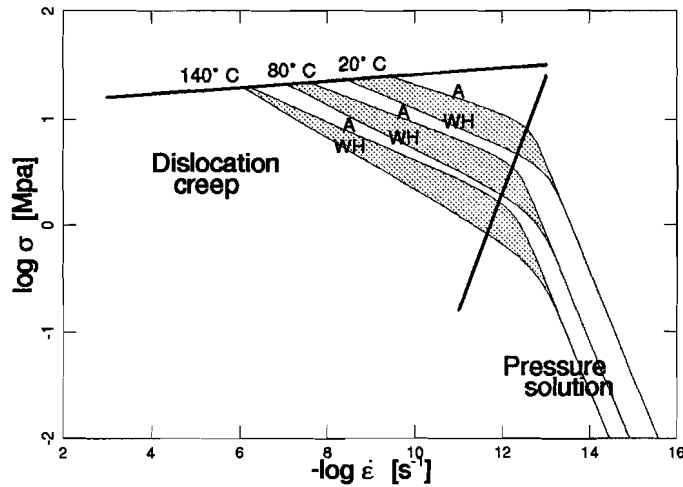
Figure 5.1 *Deformation map for rocksalt (grain size d=1 cm) constructed using the creep law (refer equation 5.1) combining pressure-solution creep and cross-slip controlled dislocation creep [Wawerzik & Zeuch, 1986] for the Asse (A) and West Hackberry (WH) salts. Reconstruction of fig. 10 of Spiers et al. [1990].*

$$\dot{\varepsilon}_{dc,l} \;=\; \varepsilon_{0l}(T)\,\sigma_l^{\,n(T)} \tag{5.6}$$

where

$$n(T) \;=\; \frac{Q_{cs}}{RT} \qquad \text{and} \qquad \varepsilon_{0l}(T) \;=\; D\exp\!\left[-\frac{Q_{cs}}{RT}\ln\frac{\tau_0}{\mu_0}\right]\mu^{-\frac{Q_{cs}}{RT}}$$

For Asse salt (file BCGR1, table 5.2), $Q_{cs} \approx 19$ kJmol^{-1}. For the temperature range 20-200 °C, this gives an effective 'power law' exponent $n(T) = 7.8 - 4.8$. For West Hackberry salt (WH2, table 5.2), the same temperature range yields $n(T) = 5.8 - 3.7$.

Now, the parameters D, τ_0/μ_0, and Q_{cs} in (5.6) are determined from axisymmetric compression experiments, and $\dot{\varepsilon}_{dc,l}$ and σ_l represent axial strain rate and differential stress. To obtain a generalized expression for shear viscosity, equation (5.6) must be rewritten in terms of effective deviatoric stress and strain rate [Ranalli, 1987, p. 78]. For the effective strain rate due to dislocation creep, this yields

$$\dot{\varepsilon}_{dc} = \left\{ \frac{3^{(n(T) + 1)/2}}{2} \, \varepsilon_{0l}(T) \right\} \sigma^{n(T)} = \varepsilon_0(T) \, \sigma^{n(T)} \tag{5.7}$$

with the corresponding shear viscosity then given

$$\eta_{dc} = \frac{\sigma}{2\dot{\varepsilon}} = \eta_0 \, \dot{\varepsilon}^{1/n - 1} \tag{5.8}$$

where

$$\eta_0 = \frac{1}{2} \left[\frac{3^{(n+1)/2}}{2} \cdot D \right]^{-\frac{1}{n}} \mu \frac{\tau_0}{\mu_0} \qquad \text{and} \qquad n = \frac{Q_{cs}}{RT}$$

Viscosity associated with pressure-solution creep

Once again, the parameters in (5.2) are determined from axi-symmetric experiments. Following the above approach [Ranalli, 1987] and noting that (5.2) can be viewed as a power law with $n = 1$, we can write the shear viscosity due to pressure solution as

$$\eta_{ps} = \frac{\sigma}{2\dot{\varepsilon}_{ps}} = \frac{\sigma}{3\dot{\varepsilon}_{ps,l}} = \frac{Td^3}{3 \times 6.95 \, V_m \cdot 10^{-15} \cdot \exp[-24530/RT]} \tag{5.9}$$

Total effective shear viscosity of salt

Following equation (5.1), the total strain rate due to the above mechanisms can now be written,

$$\dot{\varepsilon} = \dot{\varepsilon}_{ps} + \dot{\varepsilon}_{dc} = f_s(T, d)\sigma + \varepsilon_0 \sigma^n \tag{5.10}$$

where f_s describes the temperature and grain size dependence of the pressure solution creep rate $(f_s(T, d) = 1/(2\eta_{ps}))$, and ε_0 and n are defined in (5.8). Re-expressing this in the form

$$\dot{\varepsilon} = \left[f_s(T, d) + \varepsilon_0^{\frac{1}{n}} \dot{\varepsilon}^{\frac{n-1}{n}} \right] \sigma \tag{5.11}$$

then leads to the total effective shear viscosity, given

$$\eta = \frac{\sigma}{2\dot{\varepsilon}} = \frac{1}{2f_s(T, d) + 2\varepsilon_0^{\frac{1}{n}} \dot{\varepsilon}^{\frac{n-1}{n}}} = \left[\frac{1}{\eta_{ps}} + \frac{1}{\eta_{dc}} \right]^{-1} \tag{5.12}$$

This geometric mean of the viscosities, derived for the parallel operation of two creep mechanisms, is equivalent to the Ellis model, discussed by Bird et al. [1960]. The same method of expressing the shear viscosity as a function of two different creep mechanisms has been used in mantle convection modelling by Parmentier et al. [1976] and Van den Berg et al. [1993].

Influence of strain rate, grain size, temperature and salt type on total viscosity

Figure 5.2 displays total effective viscosity η as a function of strain rate $\dot{\varepsilon}$, for different grain sizes d, temperatures T and types of rocksalt (Asse or West Hackberry). The thin lines in Figure 5.2a-c show the viscosity of rocksalt at surface temperature ($T = 20\ °C$) for grain sizes varying between 5 mm and 3 cm, which is the approximate range of grain sizes occurring in natural rocksalt. The solid and dashed lines indicate the viscosity of Asse and West Hackberry salt, respectively. Below a strain rate of $\dot{\varepsilon} \sim 10^{-12}\ s^{-1}$ the viscosity for the smallest grain size, $d = 0.5$ cm, is independent of the strain rate, as the diffusion creep mechanism is dominant. For larger grain sizes the transition from dislocation to diffusion creep, as the dominant mechanism, shifts to lower strain rates. The bold lines in figure 5.2 show the viscosity at a temperature of $T = 160\ °C$, which is approximately the temperature at 4 km depth in a region with a geothermal gradient of 35 K/km. The increase in temperature decreases the viscosity by around one order of magnitude.
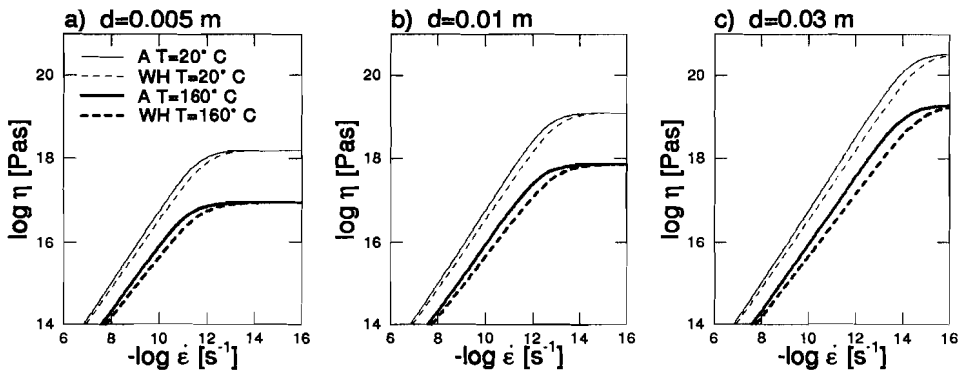
Figure 5.2 *Effective viscosity derived from the two-mechanism creep law (figure 5.1) for grain sizes of 0.5 (a), 1 (b) and 3 (c) cm. Bold lines indicate viscosity at high temperature (160 °C) normal lines at room temperature. Viscosities are shown for the Asse (A; dashed lines) and West Hackberry (WH; solid lines) salts.*

Figures 5.1 and 5.2 suggest that, for geologically relevant diapiric strain rates in non-tectonic regions ($\dot\varepsilon = 10^{-15} - 10^{-12}$ s^{-1} [Heard, 1972]) the deformation behaviour of rocksalt falls in the transition zone between the two creep mechanisms. Figure 5.2 shows that the range of $10^{17} - 10^{18}$ Pa $\cdot$ s for the Newtonian viscosity, used in most previous numerical models [Roemer & Neugebauer, 1991; Poliakov & Podladchikov, 1992] is reasonable for the finer grained salts at relatively high temperatures.

5.4 Model and governing equations

We model the dynamics of the basement-salt-sediment system in a two-dimensional layer model using a viscous fluid formulation. A realistic effective viscosity for salt has been derived above from steady-state creep laws governing the deformation of rocksalt. In contrast, using a viscous approximation for the rheology of the sediments is unrealistic in most situations. It has long been recognized from rock mechanics experiments that the deformation of sediments under upper crustal conditions is dominated by brittle/frictional-plastic processes [e.g., Byerlee, 1978; Kirby & Kronenberg, 1987]. Furthermore, geological observations show a clear relation between diapirism and faulting, both in the overlying sediment and underlying basement [to name a few: Woodbury et al., 1973; Mart & Hall, 1984; Jenyon, 1986; Cobbold & Szatmari, 1991; Remmelts & Van Rees, 1992]. Only rarely might the overlying sediment be expected to deform mainly by viscous creep, e.g. in the Great Kavir in central Iran [Jackson et al., 1990]. In that particular region, the clastic redbeds overlying the salt show a complete lack of diapir-related faulting, probably because of significant weakening and pervasive flow caused by disseminated halite. Hence, in the general situation a constitutive description that uses ductile creep for the rocksalt and a brittle/frictional-plastic deformation mechanism for the sediments is most appropriate for modelling salt diapirism.

Unfortunately, incorporation of this type of compound constitutive description into numerical models is hampered by technical difficulties induced by the distinct nature of the time-independent (brittle) versus time-dependent (creep) mechanisms, and the discontinuous change across the sediment-salt interface. Only very recently, efforts to resolve this problem in numerical models have started appearing in literature [Bobineau, 1992; Schultz-Ela & Bobineau, 1992]. In the present paper, however, we use a simple linear viscous rheological model for the overlying sediment, taking a viscosity that gives geologically reasonable values for ascent velocities and strain rates. This is clearly not appropriate for modelling the structural evolution which generally accompanies salt diapirism, but it allows us to determine an estimate of the temporal and spatial variability of the effective

viscosity within diapiric rocksalt, and can be used for comparison with previously published Rayleigh-Taylor models, describing salt diapirism.

Having decided on the rheological description to be used, the dynamics of the salt structure can now be described by the Stokes equation

$$-\nabla p + \nabla(\eta \underline{\dot{\varepsilon}}) = -\rho \mathbf{g} \tag{5.13}$$

where p is the dynamical pressure, η the viscosity, $\underline{\dot{\varepsilon}}$ the deviatoric strain rate tensor, with components $\dot{\varepsilon}_{ij} = \frac{1}{2}(\partial v_j/\partial x_i + \partial v_i/\partial x_j)$, and $\mathbf{g}$ the gravity vector. The second invariant of the strain rate tensor, used in calculating the effective viscosity (5.12) is defined by $\dot{\varepsilon} = [\frac{1}{2}\dot{\varepsilon}_{ij}\dot{\varepsilon}_{ij}]^{\frac{1}{2}}$, where the Einstein convention for summation is used. The flow is assumed incompressible. Pressure is eliminated from equation (5.13) by the introduction of the stream function ψ as a velocity potential $(\mathbf{v}^T = (\partial\psi/\partial y , -\partial\psi/\partial x))$. Subsequent equations are given in dimensionless form, following the scaling given by Christensen [1984a; see also table 2.1].

First, the equation of motion for a N-layer model with thermal and chemical buoyancy forces is given by

$$\left[\frac{\partial^2}{\partial x^2} - \frac{\partial^2}{\partial y^2}\right]\eta\left[\frac{\partial^2\psi}{\partial x^2} - \frac{\partial^2\psi}{\partial y^2}\right] + 4\frac{\partial^2}{\partial x\partial y}\left[\eta\frac{\partial^2\psi}{\partial x\partial y}\right] =$$

$$Ra\frac{\partial T}{\partial x} - \sum_{i=1}^{N-1} Rb_i\frac{\partial\Gamma_i}{\partial x} \tag{5.14}$$

[Christensen & Yuen, 1984]. Here Ra is the thermal Rayleigh number, defined

$$Ra = \frac{\alpha\rho g\Delta T h^3}{\kappa\eta_0} \tag{5.15}$$

and Rb_i are the so-called boundary Rayleigh numbers

$$Rb_i = \frac{(\rho_i - \rho_{i+1})g h^3}{\kappa\eta_0} \tag{5.16}$$

where ρ_i is the density in the i-th layer. The layers and the interfaces are numbered sequentially from the top down. The function $\Gamma \equiv \sum_{i=1}^{N}\Gamma_i$ describes the N-layer composition. We take each Γ_i to be 0 in the layers above in the interface i, and 1 in the layers below. The functions Γ_i are discontinuous across the interface i.

For the thermal regime, we impose an average geothermal gradient (dT/dz) by keeping the temperature constant at the top $(T_0 = 20\ ^{\circ}\text{C})$ and bottom $(T_b = T_0 + (dT/dz) \times h)$. The thermal diffusivity of the salt is much higher (approximately 5 times) than the diffusivity of the surrounding sediment, and this

will have a strong influence on the temperature distribution in and around the salt [Selig & Wallick, 1966]. For models of salt diapirism with a typical vertical length scale of 4 km, the thermal Rayleigh number is around unity, much smaller than the critical Rayleigh number [Busse, 1989], and thermal buoyancy forces can be neglected. In addition, the thermal diffusion time h^2/κ, (where h is the depth of the layer and κ is the thermal diffusivity) is much shorter than the turn-over time of the system. For example, taking $h = 4$ km, and the accepted thermal diffusivity for salt ($\kappa = 5 \times 10^{-6}$ m^{2}s^{-1}) the diffusion time scale is 100,000 a, compared with 10-100 Ma for a diapir to reach its mature stage [Jackson & Talbot, 1986]. This implies that thermal advection can be neglected and the temperature in and around the salt can be calculated from the steady-state heat diffusion equation. We neglect here possible effects of convection in ground water surrounding the salt.

As shown in figure 5.3, the present fluid layers are contained in a rectangular box with aspect ratio (length-to-depth ratio) λ. The side boundaries are reflective, the top boundary is free-slip, the bottom boundary is either free-slip or rigid (stick-slip). The temperature is kept constant at the top and bottom. The dynamics of this N-layer model are then governed by the equation of motion (5.14), the temperature equation

$$\nabla k \nabla T = 0 \qquad\qquad\qquad (5.17)$$

(where k is the thermal conductivity), the transport equation for the layer
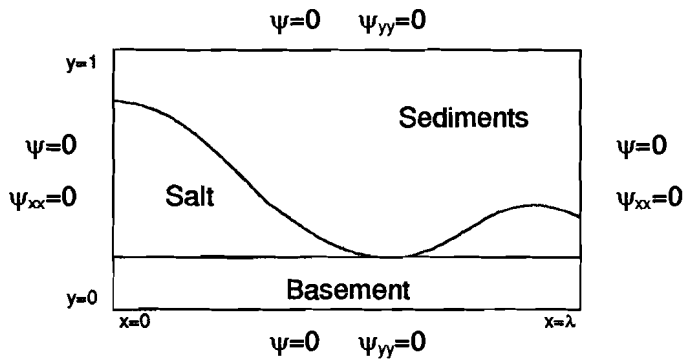
Figure 5.3 *Geometry and boundary conditions used in the present model. The salt diapirism is modelled in a rectangular box with aspect ratio λ with stress free boundaries. Top and bottom are kept at constant temperature, side walls are reflective. No material can flow in or out of the box.*

composition, given

$$\frac{\partial \Gamma}{\partial t} + (\mathbf{v} \cdot \nabla)\Gamma = 0 \qquad (5.18)$$

(where t is time), and the viscosity law (given for the salt by (5.12)).

5.5 Numerical method

The equation of motion and the heat equation are solved here using the method of Galerkin, applying a finite element method to construct the basis functions [Cuvelier et al., 1986]. Using this type of numerical method, it is possible to construct a full solution to the non-linear and time-dependent problem for given initial and boundary conditions and given physical parameters. The method also allows for a well-controlled experimental search for solutions in a given parameter space. Although the solution obtained is approximate, the accuracy can be very high. With good numerical analysis and a careful implementation of the method, it is well possible to constrain the errors in the solution to be small. A carefully controlled numerical method is to be preferred to methods of linear stability analysis, since the latter degrade the full problem via the linearizations introduced to allow analytical solutions. Thus, stability analysis gives only a very limited subset of solutions to the full problem contained in the solutions from the numerical method. A much more important problem than the finite accuracy of the numerical solution, is the applicability of the description of the physics of the model to the geological situation, but this holds equally for numerical, analytical and experimental methods.

For solving the equation of motion, we have used two different finite element methods. The first employs a type of non-conforming element that stems from plate bending problems [Zienkewicz, 1977] and which has found application in mantle convection modelling also [Hansen & Ebel, 1984]. The second method was the method of splines, which has been used by several authors in mantle convection modelling [Kopitzke, 1979; Christensen & Yuen, 1984], and in studies of salt diapirism [Woidt, 1978; Schmeling, 1987; Roemer & Neugebauer, 1991]. The buoyancy forces are determined by the position of the composition function Γ alone. Here, the interface between fluids is modelled by a chain of markers that advect with the flow. We followed Christensen & Yuen [1984] in the implementation of the buoyancy forces and the advection of the markers, using a predictor-corrector method. Both finite element methods were tested against a variety of analytical models, and against published numerical models for Rayleigh-Taylor instabilities [e.g., Poliakov & Podladchikov, 1992] and showed good agreement. The method using the non-conforming element has also been extensively tested for mantle convection problems and it compares well with Hansen's implementation in

the European mantle convection benchmark [Blankenbach et al., 1989]. The codes were checked against a non-Newtonian benchmark published in Malevsky & Yuen [1992], that made a comparison between the independent spline methods of Christensen and Malevsky, and the primitive variable method published in Van Keken et al. [1992] and Van den Berg et al. [1993].

The equation of motion (5.14) is non-linear through the strain rate dependence of the viscosity. The equation is solved at each step by Picard sub-iteration [Van den Berg et al., 1993], until

$$\frac{|\,\psi_{i-1} - \psi_i\,|_\infty}{|\psi_i|_\infty} < \delta \tag{5.19}$$

where $|\psi_i|_\infty$ is the maximum of the stream function at the i-th iteration. The convergence criterion δ was taken to be $\delta = 5 \times 10^{-4}$. Typically 2-5 iterations were necessary for the cases with the largest strain rate dependence.

We used a relatively high resolution in both time and space. The speed of present day workstations is sufficient to allow for a systematic, high-resolution study of 2D time-dependent and non-linear models in a reasonable amount of time. For the spline method, we used 30 elements in the vertical direction; the number of elements in the horizontal direction was dependent of the aspect ratio of the model. For the method with the non-conforming type of element somewhat more elements (40 in the vertical direction) were used. The time-step was limited to less than 0.5 of the Courant-Friedrichs-Levy criterion [Schmeling, 1987]. The calculations were started by inducing a variety of small perturbations into the initial horizontal stratification of the basement-salt-sediment system. Harmonic perturbations have been shown to grow exponentially with a specific growth rate [e.g., Biot & Odé, 1965]. Therefore, in the initial stages of the calculations the time-step was reduced using a criterion based on growth rate [Schmeling, 1987] to be able to follow the exponential growth of the interface amplitude.

The accuracy of several runs has been checked against runs using a higher or lower resolution in time and space. The models with lower resolution (down to 15 elements in the vertical direction) showed no major quantitative differences in the evolution of the models. Only minor changes were found in the spatial character of the viscosity field. Typical runs took between 15 minutes for the most simple cases to several hours for the larger aspect ratio models.

5.6 Results

First, we will look at simple two layer models in which a sediment layer with uniform properties lies over a rocksalt layer in a rectangular cross-section with dimensions 8×4 km (aspect ratio $\lambda = 2$). Next, we will consider the influence of the basement, larger aspect ratios and varying sediment properties. Finally, models including sedimentation will be considered. In each case, we will assess the influence of the variable rocksalt viscosity on the dynamics of the system, in a comparison with models similar to those published previously.
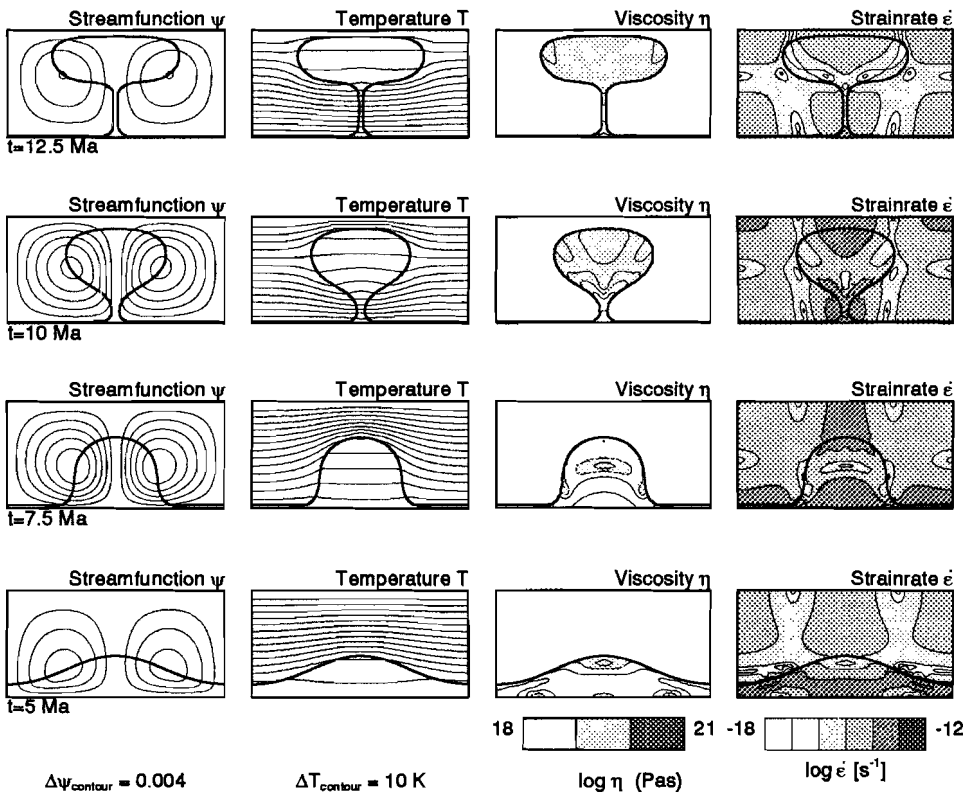
Figure 5.4 *Time evolution of a model with dimensions 8×4 km with grain size 3 cm and temperature gradient 35 K/km. Sediment has constant density 2300 kg $\cdot$ m^3 and viscosity 3×10^{19} Pa $\cdot$ s. Isolines are shown of stream function ψ, temperature T, salt viscosity η, and strain rate $\dot{\varepsilon}$*

5.6.1 Two-layer models with uniform sediment properties

Figure 5.4 shows a typical example of the development of a single diapir in a simple two-layer model. The sediment layer has a thickness of 3 km, and lies on top of a 1 km thick salt layer. The interface between the salt and sediment layers was perturbed at time 0 by a harmonic perturbation with a wavelength of 8 km and an amplitude of 40 m. Note that, as a consequence of the negligible strength of the salt and sediments, this small perturbation is sufficient to start the development of the diapir. The boundaries are free-slip and the bottom boundary is kept at 160 °C, implying an average geothermal gradient of 35 K/km. The salt has the dislocation creep properties of West Hackberry rocksalt (WH2; see table 5.2), a grain size of $d = 3$ cm, and density $\rho_{salt} = 2160$ kg $\cdot$ m^{-3}, which lies midway in the range recorded for natural salt [Gevantman, 1981; Hatheway & Kiersch, 1982]. The sediments are isoviscous with $\eta_{sediment} = 3 \times 10^{19}$ Pa $\cdot$ s. The density of the sediments is $\rho_{sediment} = 2300$ kg $\cdot$ m^{-3}. Figure 5.4 shows snapshots of (from left to right) the isolines of the stream function ψ, temperature T, viscosity η, and strain rate $\dot{\varepsilon}$, at 5, 7.5, 10 and 12.5 Ma. The corresponding ranges are indicated below the figures. The snapshots for temperature clearly show the effects of the 5 times higher thermal conductivity of the rocksalt compared with the sediments; the isotherms diverge around the salt. The viscosity of the rocksalt varies nearly two orders of magnitude as the diapir travels through the sediment. Also, the effects of variations in strain rate (higher viscosity near the stagnation zone in the centre of the diapir) and temperature (increase in viscosity as the diapir moves into the colder, upper regions) are clearly visible.

For the same model, we can compare the relative contributions of the two creep mechanisms to the effective viscosity (5.12), by calculating the ratio $r = \eta_{dc}/\eta_{ps}$ where the effective viscosities derived for the two creep laws are defined in (5.8) and (5.9). For $r > 1$, dislocation creep gives a larger effective viscosity than pressure-solution creep, indicating that the latter (Newtonian) mechanism is dominant. Figure 5.5 displays this ratio for the above model with grain size $d = 3$ cm. In the grey region, the dislocation creep mechanism is dominant. In stagnation zones, where the strain rate is low, Newtonian creep is dominant. In areas with large deformation rates dislocation creep yields a lower viscosity and becomes the dominant mechanism. At the beginning and end of the diapiric evolution the strain rates are low and the pressure-solution creep mechanism is dominant throughout the salt.

In the following we will consider the influence of variations in grain size, overburden viscosity, and geotherm on the evolution of the diapir and the effective viscosity distribution in the rocksalt.
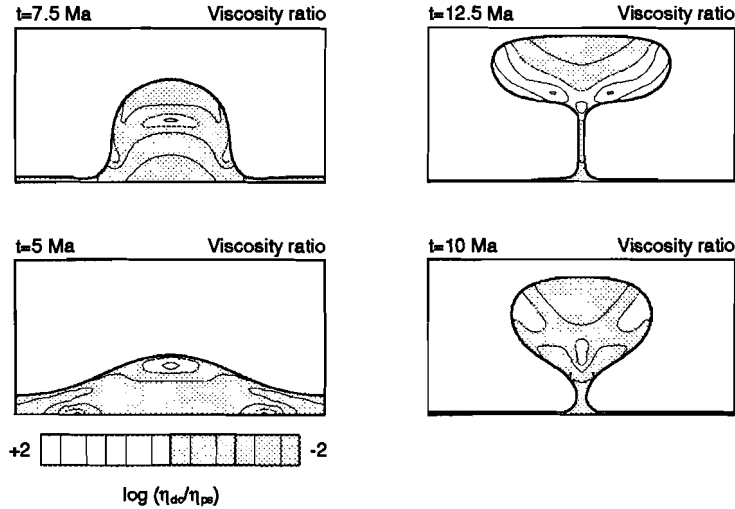
Figure 5.5 *Evolution of the viscosity ratio r (see text) for the model in figure 5.4. The grey area indicates dislocation creep is dominant. Diffusion creep is dominant in the white area.*

Effect of grain size

Figure 5.6 shows the temporal evolution of a range of parameters, calculated for models similar to the one represented in figure 5.4. Displayed are the height of the diapir (h) and the minimum (η_{min}), maximum (η_{max}), and volume averaged (η_{av}) viscosities within the rocksalt for $d = 0.5, 1, 2$, and 3 cm. For the models with the largest grain size, a clear influence of the strain rate dependent dislocation creep mechanism is visible: both η_{min} and η_{av} show minima around $t = 5$ Ma and $t = 7.5$ Ma, where the strain rate peaks at nearly 10^{-12} s^{-1}. The average (rms) velocity peaks here too, at about 600 m/Ma. These peaks are associated with reorganizations in the flow field, as the interface between salt and sediment feels first the bottom boundary (the basement), and next the side boundary (just before the necking stage). For the case with the smallest grain size ($d = 0.005$ m), η_{min} is largely uniform throughout the evolution; the strain rate thinning effect is minimal. As seen for all grain sizes, the average viscosity increases by nearly an order of magnitude as the diapir moves into the colder parts of the section.

Although the effective average viscosity of the rocksalt varies by more than two orders of magnitude in these models, the speed with which the diapir travels is hardly affected. For all cases, the viscosity of the sediment (3×10^{19} Pa $\cdot$ s) is higher than the salt viscosity. As has been mentioned previously [Jackson &
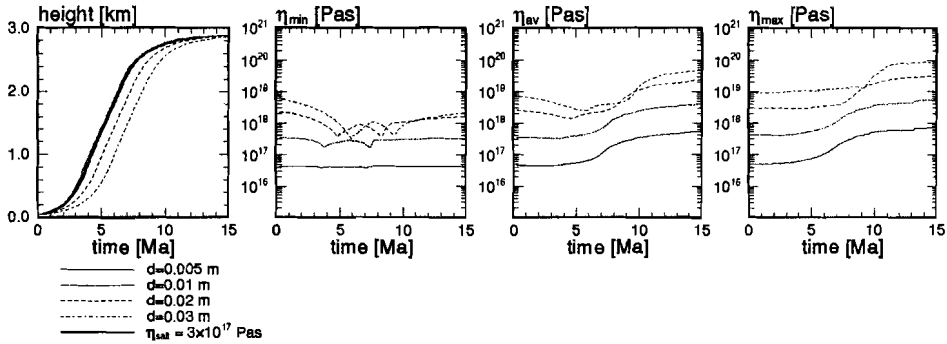
Figure 5.6 *Top of diapir, and minimum, average and maximum viscosity in the salt for the model in figure 5.4. Grain sizes vary between 0.5-3 cm. In this range the viscosity varies by more than two orders of magnitude. The temperature difference between top and bottom causes a viscosity increase of almost an order of magnitude as the diapir moves up. The bold line in the first frame indicates a model with a constant Newtonian viscosity $\eta = 3 \times 10^{17}$ Pa · s for the salt.*

Talbot, 1986], the layer with the highest viscosity controls the uplift rate of the diapir. This is illustrated by taking a model with constant salt viscosity. In the plot of the height of the diapir ($h(t)$ in figure 5.6), the thick solid line represents the evolution of the model with a uniform salt viscosity of 3×10^{17} Pa · s and a sediment viscosity of 3×10^{19} Pa · s, the values used by Woidt [1978] and Roemer & Neugebauer [1991]. The model description is comparable to model A of Roemer & Neugebauer [1991; p. 2392], but not exactly the same. This results in that in our case the diapir travels faster because of the thicker source layer (1 km c.f. 500 m) and the higher density contrast with the sediment (140 kg · m^{-3} c.f. 100 kg · m^{-3}).

Effect of sediment viscosity

In all of the above simulations, the evolution of the diapir is fast (full development after 10 Ma) and this induces a maximum volume averaged strain rate on the order of 10^{-13} s^{-1}. This is higher than the estimated strain rates in most diapiric regions [Jackson & Talbot, 1986]. An increase of the viscosity of the sediments to $\eta_{sediment} = 10^{20}$ Pa · s retards the diapir evolution. Figure 5.7 shows the evolution the top of the diapir ($h(t)$) and the viscosity for varying grain size. Full development of the diapir is now after 30 Ma. The effective viscosity for salt with grain size 0.5 cm is clearly unaffected by the increase in sediment viscosity. The models with larger grain sizes show similar behaviour to that obtained with the lower sediment viscosity, but the average viscosity is just a little higher (20-30 %). In models
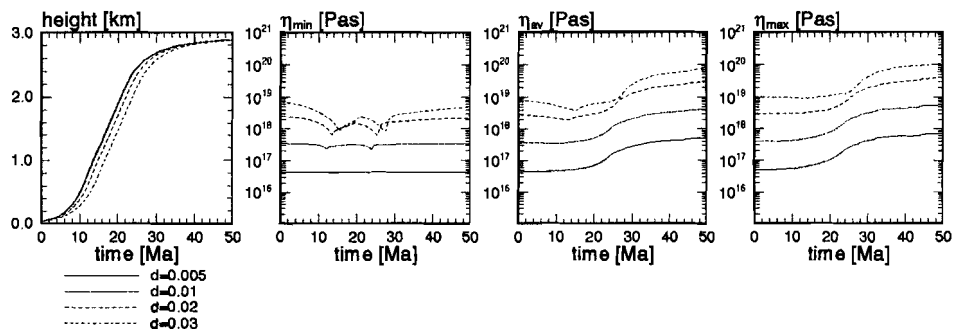
Figure 5.7 *As figure 5.6, but now for a higher viscosity of the overburden* $\eta_{sediment} = 10^{20} \ Pa \cdot s$.

with a 5 times higher sediment viscosity, $\eta_{sediment} = 5 \times 10^{20}$ Pa $\cdot$ s, the diapir needs more than 250 Ma to reach its maximum height. The corresponding strain rates are very low (the average strain rate does not exceed 10^{-17} s^{-1}) and the strain rate thinning effect is minimal for all grain sizes.

Effect of geothermal gradient

In all of the above models a geothermal gradient of 35 K/km was maintained, which is at the high end of estimates for the gradient in the U.S. Gulf Coast region [22-36 K/km; Carter & Hansen, 1983]. The gradient is estimated at 30 K/km for
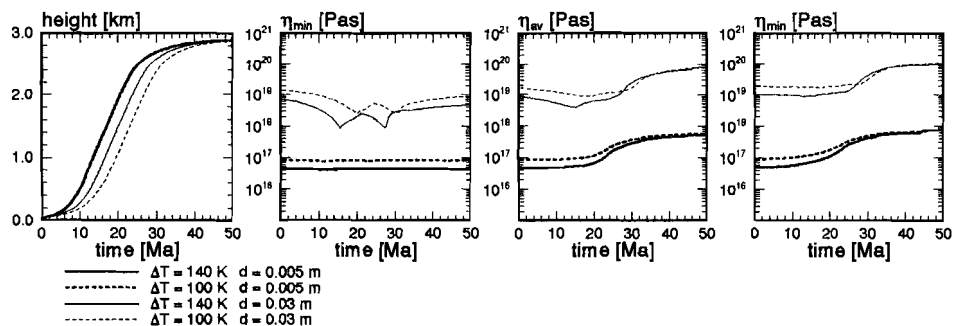
Figure 5.8 *As figure 5.7, but now for temperature gradients 25 K/km (dashed lines) and 35 K/km (solid lines). Bold lines indicate grain size 0.5 cm, normal lines grain size 3 cm.*

the Great Kavir region in central Iran [Jackson et al., 1990]. We have varied the gradient between 25 and 35 K/km for two-layer models with $\eta_{sediment} = 10^{20}$ Pa · s and varying grain size. Figure 5.8 shows results for $dT/dz = 25$ K/km for grain sizes $d = 0.5$ and 3 cm, in comparison with those of figure 5.7. For the models with grain size 0.5 cm, the viscosity at depth is higher by about half an order of magnitude, but the overburden viscosity remains much higher and, as can be expected, controls the dynamical evolution of the model. For the models with larger grain size, the effective salt viscosity is strongly influenced so that the variation in geothermal gradient has a clear, but not very large, dynamical effect.

Volumetric importance of mechanisms

In the above examples, it is clear that the diffusion creep mechanism plays a major role in the dynamics of the diapirs. We can quantify this further by calculating the fractional volume of the salt in which each of the two mechanisms is dominant, using

$$R_{ps} = V_{ps}/V_{salt} \tag{5.21}$$

Figure 5.9a shows the relative volume R_{ps} for grain sizes ranging from 0.5 to 3 cm for the model with $\eta_{sediment} = 3 \times 10^{19}$ Pa · s (figure 5.6). For $d \le 1$ cm, the
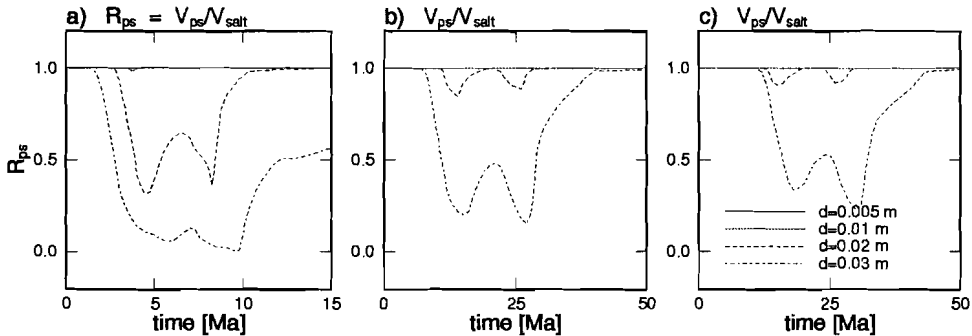
Figure 5.9 *Plots of the relative volume fraction of the salt in which the diffusion creep mechanism is dominant. Figure b) shows the temporal evolution for the model in figure 5.7, with $\eta_{sediment} = 10^{20}$ Pa · s and geotherm dT/dz=35 K/km. Figure a) shows the effect of viscosity decrease of the overburden to $\eta_{sediment} = 10^{20}$ Pa · s (refer figure 5.6). Figure c) shows the effect of a decrease of the geothermal gradient to dT/dz=25 K/km (refer figure 5.8).*

influence of the dislocation creep mechanism is minimal. For larger grain sizes, this mechanism becomes important and R_{ps} shows a minimum around the two peaks in the strain rate, as discussed already. Increasing the sediment viscosity strongly decreases the importance of the dislocation creep mechanism (figure 5.9b). Decreasing the geothermal gradient has a similar but less profound effect (figure 5.9c).

5.6.2 Models with large aspect ratio

The dynamics seen in preceding numerical experiments are influenced by the small aspect ratio of the box and the initial harmonical perturbation. In this section, we present results for a model with dimensions 5×20 km. Initially, the salt layer is 750 m thick in most of the model, except for a thickening of the salt by 250 m near the left hand side (figure 5.10, lowermost frames). The interface between salt and basement is at 4.25 km depth. The density and viscosity of the basement are
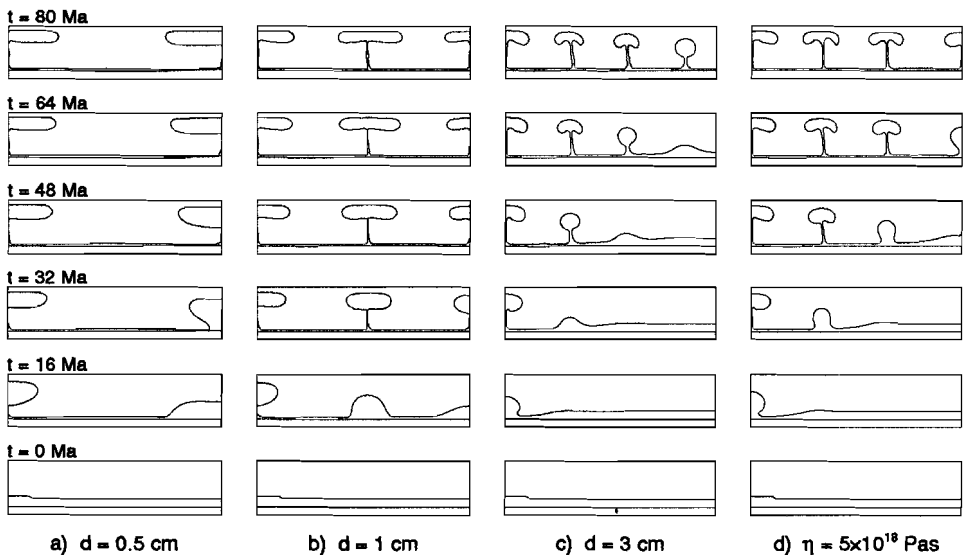
Figure 5.10 *Large aspect ratio models of dimensions 5×20 km. Viscosity of overburden is 10^{20} Pa·s. Density of the overburden is according to compaction equation (5.22). Figures a)-c) show the evolution of the models for grain sizes of 0.5, 2 and 3 cm, resp. d) shows pure Newtonian model with $\eta_{salt} = 5 \times 10^{18}$ Pa·s.*

(arbitrarily) chosen to be $\rho_{basement} = 2400$ kg $\cdot$ m^{-3} and $\eta_{basement} = 10^{23}$ Pa $\cdot$ s, which effectively guarantees that the basement does not deform during the dynamical evolution of the salt, mimicking rigid, crystalline rock. The overburden has uniform viscosity $\eta_{sediment} = 10^{20}$ Pa $\cdot$ s. For the sediment density, we have now included the effect of compaction on the sediments and used the approximation of Biot & Odé [1965] to Nettleton's [1934] estimates of the density-depth relation for sediments in the Gulf Coast region. This is written

$$\rho_{sediment}(z) = 2490 - 590e^{-\alpha z} - aze^{-\beta z} \quad \text{kg} \cdot \text{m}^{-3} \tag{5.22}$$

in which z is the depth in m, $\alpha = 0.59 \times 10^{-3}$ m^{-1}, $\beta = 1.6 \times 10^{-3}$ m^{-1}, and $a = 5 \times 10^{-5}$ kg $\cdot$ m^{-3}. The geothermal gradient is taken to be 35 K/km.

Figure 5.10 shows the development of the model for salt with West Hackberry dislocation creep properties and with grain sizes $d = 0.5$, 1, and 3 cm. The simulations show the development of a diapir from the thickened portion of the salt at the left, followed by the later appearance of one or more secondary diapirs. The diapirs do not reach the surface because of the lower density of the upper most sediments. There is an effect of grain size on development of the secondary diapirs. In the case with the smallest grain size ($d = 0.5$ cm, figure 5.10a), the salt behaves mostly in a Newtonian manner and has a low effective viscosity compared with that of the sediment (average viscosity of the salt at 4 km depth $\approx 3 \times 10^{16}$ Pa $\cdot$ s). The sediments control the evolution of the diapirs, resulting in two widely spaced diapirs. We have calculated the development of models with a pure Newtonian viscosity for the sediment. It was observed that increasing the viscosity of the salt decreases the spacing between the diapirs. Figures 5.10b and 5.10c illustrates this with the the evolution of the model for $d = 1$ and 3 cm. In these cases, the average viscosity in the salt at 4 km depth is around 3×10^{17} Pa $\cdot$ s, and 5×10^{18} Pa $\cdot$ s respectively. Figure 5.10d shows the development of a pure Newtonian model with $\eta_{salt} = 5 \times 10^{18}$ Pa $\cdot$ s. There are minor differences in comparison with the large grain size model; the diapirs evolve faster and the spacing between them is larger. This can be partly attributed to the non-Newtonian character of the salt in the large grain size model, causing localization of flow (smaller wavelengths) and a viscosity that can be locally higher than the average viscosity (slower evolution). However, these non-Newtonian effects do not seem to have a major influence.

5.6.3 Syndepositional diapirism

The above simulations do not include the effects of sedimentation and erosion, but model dynamic evolution after instantaneous burial of the salt beneath a thick layer of sediments. This is clearly an oversimplification [Roemer & Neugebauer, 1991]. We have addressed this by extending the present approach to models in which

diapirism can occur during sedimentation. The lowermost frames of figure 5.11 show the initial configuration used; the base of the salt layer (with similar geometry as in figure 5.10) is at a depth of 1 km. Sedimentation is slow, at a rate of 50 m/Ma, and continues until the base of the salt reaches a depth of 4.25 km. The density of
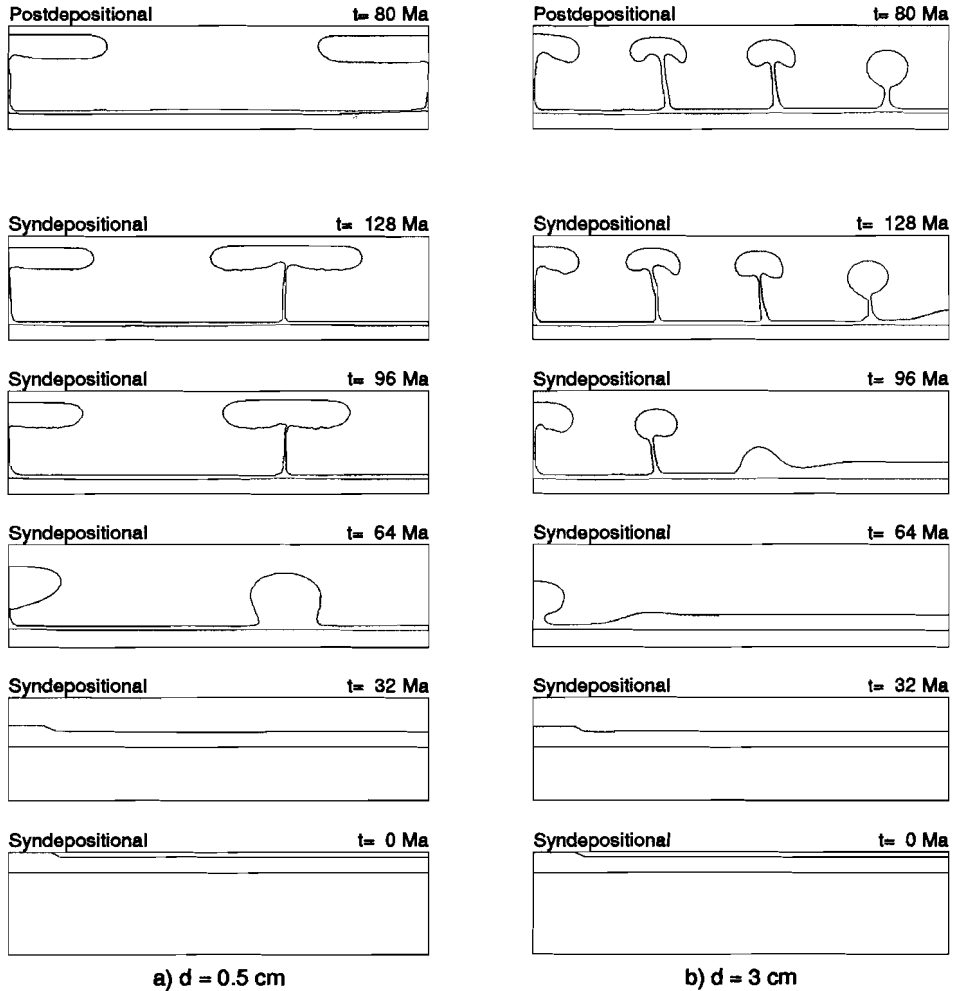

a) d = 0.5 cm   b) d = 3 cm

Figure 5.11 *Effect of sedimentation on models with grain sizes of 0.5 cm (a) and 3 cm (b). Sedimentation rate is 50 m/Ma. Other parameters as in figure 5.10. The uppermost frames show the last frames from figure 5.10 for the corresponding grain sizes.*

the sediments is given by (22). The viscosity of the sediments is taken as $\eta_{sediment} = 10^{20}$ Pa · s.

Figure 5.11a shows the development of the model for grain size $d = 0.5$ cm. Diapirism starts only after the sediments on top have compacted and the density has become higher than the salt density. The top frame of figure 5.11a shows the final stage of the postdepositional evolution as in figure 5.10. In the syndepositional case the diapirs start evolving with less overburden than in the postdepositional case, which results in a smaller diapir spacing [Jackson et al., 1990]. The syndepositional model with the larger grain size $d = 3$ cm (figure 5.11b) behaves differently. The salt has to be buried deeper for diapirism to set in as a consequence of the higher viscosity (both grain size and temperature dependent), and the diapir spacing is approximately equal to that in the postdepositional case.

Figure 5.12 shows the top of the first evolving diapir that develops with respect to the top of the salt layer (initially at a depth of 250 m for the syndepositional case, and at a depth of 3.5 km for the postdepositional case). The bold lines indicate the development for the postdepositional models, showing the fast rise until
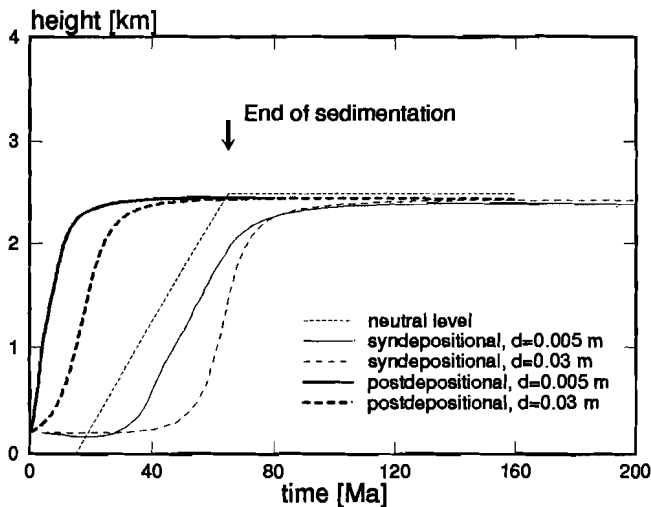
Figure 5.12 *Development of the top of the first diapir for syndepositional (normal lines) and postdepositional (bold lines) for the models in figure 5.11. The short dashed line indicates the neutral level with respect to the top of the salt layer. The top of the salt layer passes the neutral level at 15 Ma; sedimentation stops at 65 Ma.*

the mass centre of the diapir reaches the neutral level. The short dashed line indicates the position of the neutral level (at a depth of approximately 1 km) with respect to the top of the salt layer in the syndepositional case. In these models, the inversion of density does not occur before 15 Ma; sedimentation stops after 65 Ma. In the syndepositional models the diapirs are buried beneath the neutral level, and do not reach it during the sedimentation stage. In the syndepositional model with $d = 0.5$ cm, the thickened part of the salt is reduced in size, as the salt is denser than the surrounding sediment in the top 1 km of the model. The viscosity of the salt in the syndepositional model with grain size $d = 3$ cm is much higher and resists deformation until sedimentation has nearly ceased. Then the diapir moves fast, helped by non-Newtonian effects and the high density contrast between salt and surrounding sediment. Finally, note that for the large grain sizes (3 cm), there is little difference between the syn- and postdepositional evolution of the diapirs, apart from the relative time shift.

5.7 Discussion

Sensitivity of results to variability in constitutive parameters

The results presented above have been obtained using the creep parameters of West Hackberry salt (WH2; see table 5.2) to describe the dislocation creep contribution to total strain rate. For comparison we have calculated the development of models using the dislocation creep parameters for salt from the Asse mine in Germany (BGRC1). Most other types of salt quoted in table 2 of Wawerzik & Zeuch [1986] show dislocation creep behaviour that is intermediate between these two, at least in the strain rate region of interest [see Carter & Hansen, 1983; Wawerzik & Zeuch, 1986]. As expected from figure 5.1, the Asse salt parameters lead to a lower contribution by dislocation creep to the total strain rate, in comparison to the creep parameters of the West Hackberry salt. A larger volume of the salt is in the Newtonian, pressure solution, field and for the larger grain sizes the effective average viscosity is higher.

Turning to the pressure-solution creep law (5.2), used in present study, uncertainties in the pre-exponential factor and activation energy reported by Spiers et al. [1990], imply uncertainties in the effective viscosity η_{ps} of a factor of around 3. However, this is negligible in comparison to variations in η_{ps} as a consequence of grain size and temperature changes (2-3 orders of magnitude), and the uncertainties in question have a negligible effect on the evolution of the models.

In the present paper, the temperature distribution in the salt has been calculated assuming that the thermal conductivity of the salt is $5 \times$ higher than that of the

surrounding sediment. Thermal conductivity data for some typical sediments is given by Clark [1966]: $k = 1 - 2.3$ Wm^{-1}K^{-1} for sandstone (depending on porosity), and $k = 1.75$ Wm^{-1}K^{-1} for shale . The thermal conductivity of rocksalt has been measured as 5.7 Wm^{-1}K^{-1} [Schoen, 1983], giving a range of 2.5-5.7 for the thermal conductivity ratio. Varying this ratio in the models changes the lateral temperature distribution, which is important during the the diapiric stage, but even then no clear effect on the rheology can be observed. The primary effect is the decrease of temperature as the salt moves up along the geotherm. The present results have shown that it is important to take this into account when calculating the effective viscosity.

In our models, we have neglected thermal convection. This is valid at least for thin ($\sim$ 1 km) layers. For salt layers with a thickness above 2 km, thermal convection has been suggested as a feasible mechanism for the internal deformation of the salt. For example, Jackson et al. [1990] used linear stability analysis to study thermal convection within the salt of the Great Kavir region. (Note the erroneously high thermal expansion coefficient α printed in Jackon et al. [1990; their table 3.2]: $\alpha \approx 10^{-5}$ K^{-1} should be used to reconstruct their figure 3.8. This agrees better with the quoted value of α from Gevantman [1981]: $\alpha = 4.25 \times 10^{-5}$ K^{-1}). For a viscosity lower than $\sim 10^{16}$ Pa $\cdot$ s the thermal Rayleigh number in a layer > 2 km thick is larger than the critical Rayleigh number, $Ra_c = O(10^3)$, and low amplitude thermal convection might be possible. Jackson et al. [1990] have used this effective viscosity of 10^{16} Pa $\cdot$ s to scale both laboratory and analytical models of the Great Kavir salt diapirs. It is not clear to us how they obtained this low value of $\leq 10^{16}$ Pa $\cdot$ s for pressure-solution creep in salt with grain size $d = 5$ mm [Jackson et al., 1990; their figure 2.1], since most of the results published by Urai et al. [1986] to which they refer, are consistent with the creep law of Spiers et al. [1990; see figure 9], used in the present study (equation 5.9). For $T = 70$ °C and $d = 0.005$ m, this creep law gives an effective viscosity (for pressure-solution creep alone) $\eta_{ps} = 4 \times 10^{17}$ Pa $\cdot$ s, which is almost two orders of magnitude higher than the value used by Jackson et al. [1990]. Such a value rules out thermal convection within the salt. To obtain thermal convection in salt using present rheology, a thickness of the salt layer of more than 30 km is required.

In addition to the above, Jackson et al. [1990] used the same low value of 10^{16} Pa $\cdot$ s for the viscosity of the sediments, to scale the results obtained from the centrifuge models and linear stability analyses. Inserting this value for $\eta_{sediment}$ in our models gave an unrealistically fast development of the diapirs. In models with the same initial geometry as in figure 5.10, and with $\eta_{salt} = \eta_{sediment} = 10^{16}$ Pa $\cdot$ s, the first diapir reached maturity in approximately 12,000 years. A complete turnover of the salt was observed within 50,000 years. This short time scale is

confirmed by figure 3.10 in Jackson et al. [1990], where for some models of the Kavir region a characteristic time on the order of 5,000 years is given. This fast evolution contradicts geological evidence [see Jackson & Talbot, 1986; Jackson et al., 1990, p. 92]. As already shown by several authors [e.g. Woidt, 1978; Roemer & Neugebauer, 1991; this paper] the effective viscosity of the overburden should be at least 10^{19} Pa · s to obtain evolution of the diapiric system on a geologically reasonable time scale of 1-10 Ma.

Comments on tectonic effects and sediment rheology

The average strain rates in the models shown in this paper are typical of salt diapirism driven by buoyancy alone. Higher strain rates can occur in cases with differential loading, extrusion of the salt [Jackson & Talbot, 1986], and active compressional tectonics [Daudré et al., 1992]. For these higher strain rates, the dislocation creep mechanism might play a role even for salt with smaller grain sizes.

In most analytical, laboratory and numerical studies of salt diapirism, the rheology of the sediment has been modelled as a Newtonian fluid. The conclusions drawn in this paper with regard to diapir spacing, rise rate and overburden control can be compared with these previous models. For most geological situations the approximation of Newtonian viscous flow in the overburden is clearly not appropriate, and it emerges that the dynamics of salt diapirism is strongly, if not completely, governed by the brittle behaviour of the sediments. Recently, more realistic approximations of the brittle/frictional-plastic behaviour of the sediments have been used in physical modelling of salt diapirism by employing sand as an overburden, resting on silicone putty to simulate salt [e.g., Vendeville & Cobbold, 1987; Vendeville & Jackson, 1992]. Incorporation of a realistic deformation law for the overburden is the most important subject for future numerical modelling work on salt dynamics.

Microstructural evolution implied by models

The present buoyancy-driven models, in which the rheology of salt is described using equations (5.1)-(5.3), predict that the creep behaviour of the rocksalt during diapirism is dominated by the pressure-solution mechanism when the salt is fine-grained ($d \leq 1$ cm), with dislocation creep becoming important at coarser grain sizes. For the range of grain size perhaps most frequently seen in natural salts ($\sim 1 - 3$ cm), both mechanisms are predicted to occur, operating either simultaneously, sequentially or even in cyclic alternation in different regions of the salt. Often, pressure solution is predicted to dominate in the early and late stages of diapirism, with dislocation creep featuring in the main stage of upwelling. The

present models thus imply that coarse natural diapiric salts ($d > 1$ cm) should show microstructural evidence for both mechanisms, whereas finer salts should show pressure solution microstructures only.

As pointed out by Spiers et al. [1990], some natural domal/anticlinal salts do indeed show microstructural evidence for both dislocation and solution-transfer processes. For example, the Asse (Speisesalz) rocksalt ($d \sim 0.5 - 2$ cm) shows numerous overgrowth features indicative of solution transfer, as well as a lattice preferred orientation and subgrain structures indicative of dislocation creep [Spiers et al., 1986; Urai et al., 1987].

On the other hand, the microstructure of most domal/anticlinal salts, both coarse and fine grained, seems to be more or less entirely dominated by dislocation creep features such as subgrain development [Carter et al., 1990]. In such cases, it is possible that water loss during the natural diapiric process may have inhibited pressure-solution creep in the later stages of upwelling; there is a great deal of evidence in the literature for water loss during diapirism (e.g. from 1 to 2 % in bedded salt to < 0.01 % in some salt domes [Carter & Hansen, 1983]). An alternative explanation lies in the point made above regarding the possible occurrence of driving forces other than buoyancy. The concomitant increase in the importance of dislocation creep could then effectively eliminate pressure solution and/or evidence for its the microstructural signature. Lastly, we cannot rule out the possibility that pressure solution may be more or less precluded at natural strain rates by a transition from the dislocation creep behaviour described by equation (5.3) to dislocation creep with a lower stress sensitivity of strain rate, such as the climb-controlled mechanism reported recently by Carter et al. [1992].

5.8 Conclusions

(1) The effective viscosity of salt at strain rates typical of diapirism driven by buoyancy alone is influenced by the two assumed parallel mechanisms of dislocation creep and fluid-enhanced grain-boundary diffusional creep, thought to best describe the behaviour of salt in nature. In most of the models that were considered, the diffusional creep mechanism was found to be dominant. However, the efficiency of the diffusional creep mechanism is strongly dependent on the grain size, and for larger grain sizes (> 1 cm) the dislocation creep mechanism is important during the most vigorous diapiric stage, effectively reducing the viscosity.

(2) For the assumed dislocation and diffusional creep laws, changing the grain size from 0.5 cm to 3 cm increases the effective viscosity by more than two orders of magnitude. Typical values obtained for the viscosity of salt at 70 °C and low strain rates ($\dot{\varepsilon} \leq 10^{-15}$ s^{-1}) are 3×10^{17} Pa · s for a grain size of 0.5 cm and

9×10^{19} Pa · s for a grain size of 3 cm.

(3) Similarly, a temperature decrease of 150 K, from 200°C to 50°C, increases the viscosity by one order of magnitude. The lateral variation of temperature as a consequence of the higher diffusivity of the salt has a negligible effect on the effective viscosity. Varying the geotherm in the range typical for diapiric regions (25-35 K/km), has only a minor effect.

(4) The rheology of the sediment controls the diapiric rate. In the present models, which use a Newtonian viscous rheology for the sediments, the ratio between the viscosity of the salt and the sediment is an important factor in determining the geometry. The dislocation creep mechanism in the salt is found to have little influence on diapiric rate or geometry.

(5) For salt with small grain sizes ($d \leq 1$ cm), a difference is found between post- and syndepositional models of diapirism. In the syndepositional case, the small grained salt is weak enough to start diapirism during sedimentation and a smaller spacing between the diapirs is observed, as compared to the postdepositional models. For the larger grain sizes, the rocksalt is more viscous and the amount of deformation during sedimentation is negligible.

(6) The implication of the present models for microstructural development in salt diapirs is consistent with microstructural evidence found in some coarser natural salts for the operation of both dislocation and fluid-assisted diffusional processes. However, the dominance of dislocation microstructures reported for many other salts, even fine-grained ones, suggests that the relative importance of the pressure-solution mechanism can be suppressed during natural diapirism. This could be brought about through i) water loss, ii) increased deformation rates caused by other driving forces in addition to buoyancy, or iii) the operation, at natural strain rates, of some relatively easy dislocation mechanism not accounted for in the creep equation used in this study.

Acknowledgments

Chapter 6

Pulsating diapiric flows: Consequences of vertical variations in mantle creep laws †

Peter E. van Keken, David A. Yuen and Arie P. van den Berg

Abstract

Recent laboratory work has suggested that the rheology of the lower mantle may be Newtonian. We have studied the time-dependent dynamics of plumes interacting with a rheological interface separating an non-Newtonian upper mantle and a Newtonian lower mantle. Pulsating diapiric structures with fast time scales are promoted by the interaction of the rising plumes with this rheological boundary. Surface heat flow signals are discernible as pulses, which remain relatively stationary. They correlate well with the localized upwellings just below the surface. The presence of a mobile lithosphere from increasing the non-Newtonian power law index helps to produce a large-scale circulation in the upper mantle which draws large hot patches away from nearby upwellings. In our calculations the resultant averaged effective viscosity of the non-Newtonian upper mantle is about two orders of magnitude lower than that of the Newtonian lower mantle. A viscously stratified Newtonian model produces more incoherent and broadscale diapiric structures and is less efficient for generating sharply varying time-dependent thermal signatures.

6.1 Introduction

Mantle convection has traditionally been studied numerically or experimentally on the assumption that the creep law relating the stress to strain rate does not change character with depth [Parmentier et al., 1975; Jarvis & Peltier, 1982; Christensen, 1984a; Machetel & Yuen, 1989]. But recent experiments on perovskite analogues by Karato & Li [1992] have opened up the possibilities for the rheology of the lower mantle to be Newtonian. This finding would, then, suggest vertical variations in rheological laws with depth, as both olivine [Goetze & Kohlstedt, 1973; Karato et al., 1986] and garnet in the transition zone [Wang et al., 1991] may have strong non-linear dependence of the strain rate on the stress in the flow law. The dynamics of such types of rheological stratification, a non-Newtonian upper mantle overlying a Newtonian lower mantle, have recently been examined [Van den Berg et al., 1991] within the framework of a steady-state model. There it was found that concentrated surface streamlines and plate-like characteristics were promoted by this type of rheological stratification, in which the upper mantle had an effective viscosity which was lower than the underlying Newtonian mantle. In this work we will demonstrate that allowing for time-dependence in convection with a rheological layering will bring about some interesting phenomena in the development of pulsating diapiric flows, that is not found in models with a homogeneous rheology. Hitherto, studies on modelling of plume dynamics have been focussed on a fluid medium with a single flow law with continuously varying parameters, whether it is temperature-dependent [Christensen, 1984b; Yuen & Fleitout, 1985; Olson et al., 1988], strictly Newtonian [Hansen et al., 1990, 1992], non-Newtonian [Christensen & Yuen, 1989; Malevsky & Yuen, 1992], or with phase changes [Liu et al., 1991]. Thus, there have been no investigations on the time-dependent behaviour of plumes interacting with such a rheological boundary. From physical considerations one would expect a strong non-linear coupling to be developed at this rheological boundary where the flow law changes abruptly from a linear to a non-linear rheology in the course of the plume's ascent. Also, from the mathematical point of view the partial differential equations governing the momentum equations change suddenly from a linear to a strongly non-linear elliptic equation. There are also many circumstances in nature in which the transport property of the medium changes its character all of a sudden, such as radiation passing through composite material with vastly contrasting dielectric constants. Therefore, this problem of time-dependent mantle convection in a rheologically composite medium is very interesting from many view points.

In this work we will present results based on three different models, and show the importance of vertical variations in the creep law parameters on generating pulsating diapiric flow structures. The surface expression of discrete volcanoes along linear volcanic chains suggests that mantle plumes are in the form of diapirs

[Schilling, 1985] instead of continuous conduits.

6.2 Model, equations, and methods

The model mantle to be focussed on here is an incompressible medium with a non-Newtonian upper mantle overlying a Newtonian lower mantle. The olivine upper mantle is considered to be non-Newtonian because of the presence of dislocations in mantle xenoliths and the existence of seismic anisotropy in the upper mantle [Karato, 1988]. Recent laboratory work on garnet [Wang et al., 1991] has shown that it also has a rather strong non-linear rheology. We solve the Boussinesq equations for infinite Prandtl number convection without internal heating. The momentum and temperature equations are given in dimensionless from for temperature T, dynamical pressure p and velocity u by,

$$\nabla \cdot \underline{\sigma} - RaT\hat{z} - \nabla p = 0 \tag{6.1}$$

$$\frac{\partial T}{\partial t} = \nabla^2 T - u \cdot \nabla T \tag{6.2}$$

and the dimensionless depth-varying creep law used in the computations is given by,
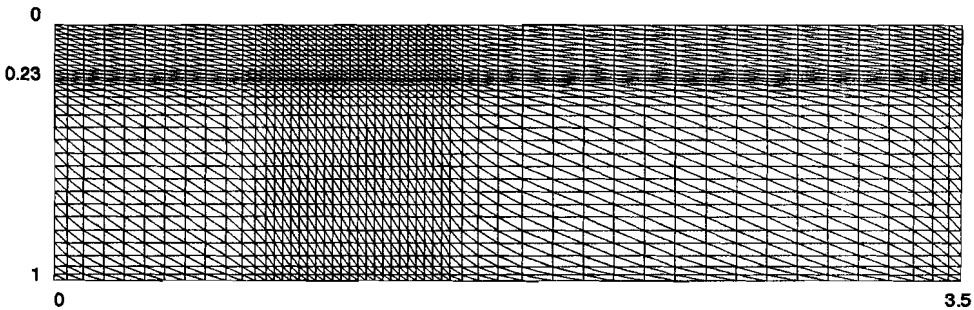
Figure 6.1 *Finite element grid used for capturing diapiric structures. This grid is used for the global snapshot in figure 6.2. Quadratic triangular elements are used for the velocity field and linear triangular elements for the temperature field. There are six grid points per velocity element and three grid points per temperature element. Vertically there are 19 velocity elements in the upper mantle and 18 in the lower mantle. Along x are 14 velocity elements between 0 and 0.8, 24 between 0.8 and 1.5 and 21 between 1.5 and 3.5. Total number of grid points used exceeds 8,500.*

$$\sigma_{ij} = A(z)\,\dot{\varepsilon}^{1/n(z)-1}\dot{\varepsilon}_{ij} \tag{6.3}$$

where *Ra* is the Rayleigh number based on the Newtonian viscosity of the lower mantle and the depth of the entire layer, σ_{ij} and $\dot{\varepsilon}_{ij}$ are the elements of respectively the deviatoric stress $\underline{\sigma}$ and strain rate tensor $\underline{\varepsilon}$, $n(z)$ represents the depth variation of the power law index n in the mantle creep law, $\dot{\varepsilon}$ is the second invariant of the strain rate tensor, defined in [Malevsky & Yuen, 1992], and T is the dimensionless temperature based on the temperature difference imposed across the layer. The important control variables of this problem are *Ra*, $n(z)$ and $A(z)$. It is to be noted that $A(z)$ in (6.3) is a dimensionless parameter and is not coupled to $n(z)$. In dimensional units $A(z)$ would depend on $n(z)$ in eqn. (6.3) [Ranalli, 1987]. For this composite rheology we find it computationally convenient to base the Rayleigh number on the linear viscosity of the lower mantle. The power law index for the lower mantle is taken to be $n = 1$, representing a diffusion creep mechanism. For the upper mantle we take either $n = 1$ (for the purely Newtonian layered case) or $n = 3$, representing a dislocation creep mechanism [Ranalli, 1987]. In the model with a lithosphere present we use $n = 5$ to describe Dorn creep used for describing lithospheric deformation [Cloetingh et al., 1982].

The coordinates are given by x and z with the z-axis aligned with the gravity vector. Isothermal boundary conditions ($T = 0$ and $T = 1$) are imposed respectively at the top ($z = 0$) and bottom ($z = 1$). We integrate equations (6.1), (6.2), (6.3) in time with a penalty function, finite element method [Cuvelier et al., 1986], imposing free-slip, impermeable boundary conditions along all sides and reflecting boundary conditions at the two vertical boundaries.

A predictor-corrector method [Van den Berg et al., 1993; this thesis, Chapter 3] is used in advancing the set of time-dependent convection equations with a penalty function parameter of 10^6 and with linear temperature and quadratic velocity triangular elements. We have benchmarked for aspect ratio one this primitive variable code against two codes [Christensen, 1984a; Malevsky & Yuen, 1992] based on bicubic splines for non-Newtonian ($n = 3$) rheology and found good agreement [Malevsky & Yuen, 1992; Van den Berg et al., 1993]. For this problem with fast diapiric instabilities coming off a rheological boundary, grid refinement is needed at the interface ($z = 0.23$). Figure 6.1 shows the finite element grid configuration with aspect ratio 3.5 which is used for monitoring a time-dependent solution, shown in figure 6.2, in which 49 and 59 unevenly spaced velocity elements are used respectively along the vertical and horizontal directions. There are six grid points in one velocity element and three points in one temperature element, because of the different order [Van den Berg et al., 1993; this thesis, Appendix B]. The vertical column with a dense grid is moved along x adaptively by the user in order to follow and capture the diapiric structure rising from the central plume shown in figure 6.2.
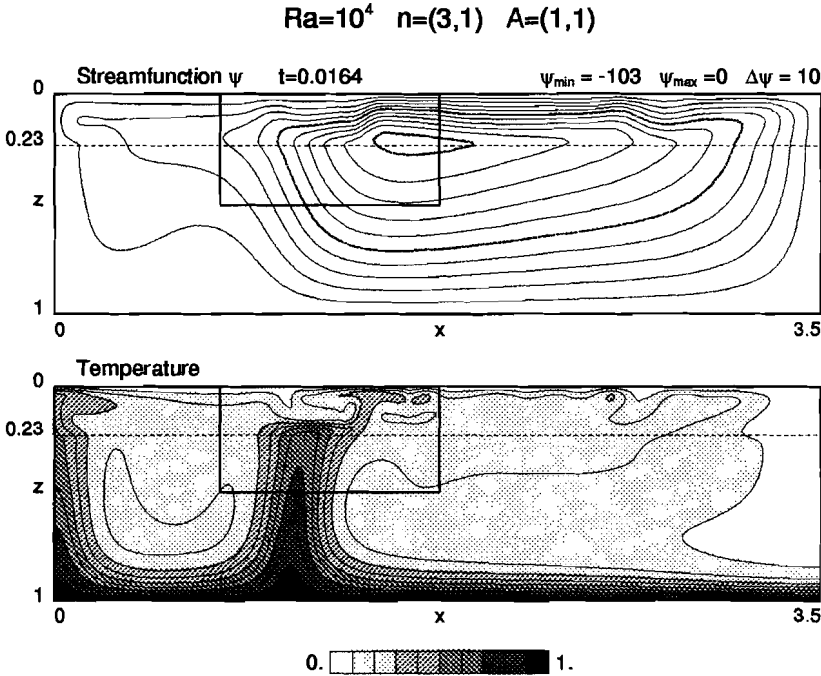
Ra=10⁴ n=(3,1) A=(1,1)

Figure 6.2 *Global shots of the stream function and temperature T for model A. This is a model with a non-Newtonian upper mantle above a Newtonian lower mantle with the same prefactors A. Ra based on the lower mantle viscosity is 10^4. The boundary between upper and lower mantle is at z = 0.23. The box indicates section where zoom snapshots are taken. Time is non-dimensionalized by the thermal diffusion across the layer (d^2/κ). For a model mantle 1800 km deep (accounting for the spherical to cartesian transformation), t = 0.001 would correspond to 102 Myr. Greyscales are linear in scale and evenly spaced.*

These calculations have been conducted for an aspect ratio of 3.5 in order for the plumes not to be influenced by edge effects. In contrast to Newtonian convection the computational time for this type of mixed Newtonian-non-Newtonian fluids is much longer than for simple Newtonian fluids, as the viscosity distribution changes in time, and sub-iteration is needed at each time-step. The cost in CPU time is at least 5 times greater than for purely Newtonian fluids (see case H below in figures 6.11-6.16). We note that it is essential to examine the dynamics of this type of flow first in two-dimensional configurations, which allow much better - and necessary - resolution for the diapiric regimes than is now feasible in 3D [Rabinowicz et al., 1990]. Moreover, the spatial and temporal resolutions needed for

monitoring sharp diapiric instabilities in 3-D would impose a severe restriction on
an extensive investigation of strongly convecting regimes in which a new physical
mechanism has to be understood.

In contrast to the study of steady-state situations [Van den Berg et al., 1991],
visualization of the time-dependent events on graphics workstations plays an indis-
pensable role in this investigation. Many of the phenomena shown below (see for
example figures 6.2 and 6.3) may not have been perceived, had we not employed
visualization techniques to monitor in detail the temporal development of these
flows.

6.3 Results

In this section we present results taken from large-scale numerical simulations of
three cases. These computations are lengthy and require over 100 hours of super-
computer (CRAY-XMP) time. The first is called model A which consists of a non-
Newtonian upper mantle above a Newtonian lower mantle. The second model,
model C, is similar to model A, but with a lithosphere. The third, model H, has a
viscously stratified Newtonian rheology throughout.

Model A (with non-Newtonian upper mantle and Newtonian lower mantle)

In this first case, A, we will examine a two-layer model with $n(z) = (3, 1)$ for the
upper and lower mantle, respectively; the prefactors are $A = (1, 1)$ for the two lay-
ers and Rayleigh number is 10^4. The initial condition is taken from a steady-state
solution [Van den Berg et al., 1991] together with a perturbation in T with an
amplitude of 0.05 and fundamental sinusoidal wavelengths along both x and z
directions. Figure 6.2 shows a global snapshot at diffusional $t = 0.0164$, which
takes place well after the initial transients have died away. The smaller box repre-
sents the region to be focussed on in figure 6.3. This is the site of the broad
upwelling impinging on the rheological interface. At the interface there is a drop in
effective viscosity owing to the stresses produced by the large-scale rapid circula-
tion in the upper mantle. We notice that at the left the upwelling does not undergo
a sharp change in the horizontal dimension. From the grey scale contours one can
see that in the upper mantle there is a large patch of medium-temperature material
being advected around by the large-scale flow. The descending currents are slug-
gish in the lower mantle because of the increase of viscosity, as the flow descends
into a stiffer Newtonian lower mantle. At the interface above the upwelling lower
mantle plume a boundary layer has been formed. In figure 6.3 we show the sequen-
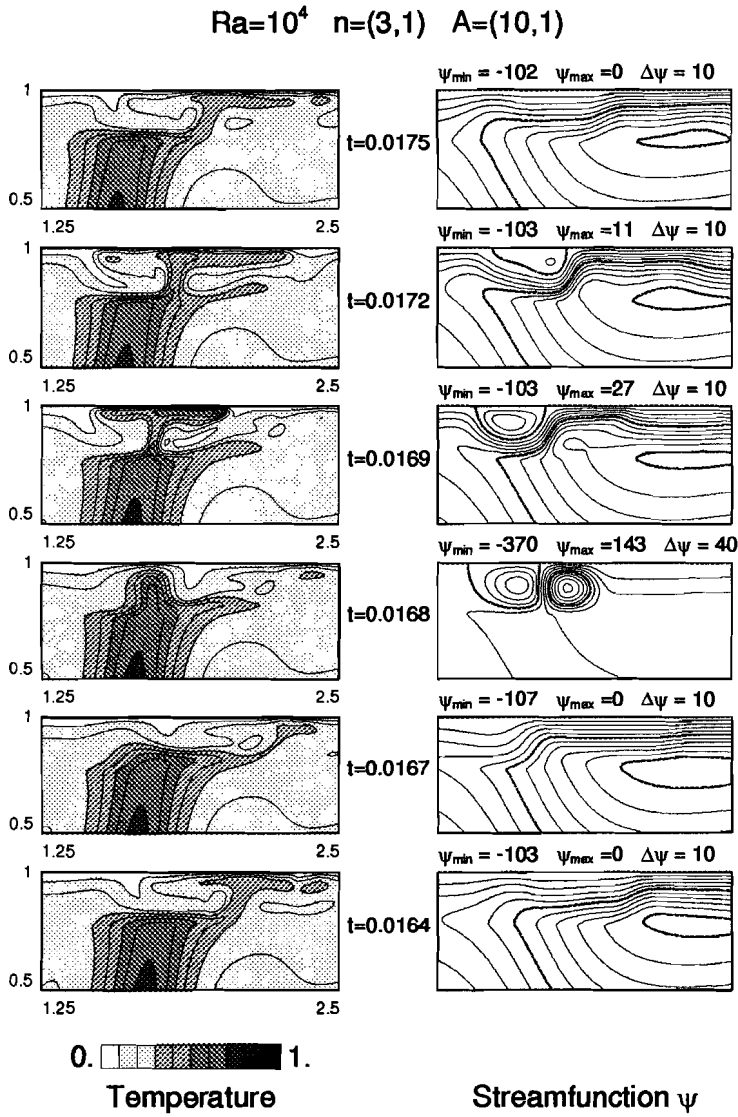tial development of this boundary layer, as it becomes unstable. The hot material is

Ra=10^4 n=(3,1)   A=(10,1)

Figure 6.3 *Sequence of zoom-in snapshots of T and ψ for case A. Time advances upward. The period of the pulsation is around 0.0008 which is shorter than the overturn time of the large-scale flow. Overturn times scale as $O(d/V_{rms})$. For this case it is $O(0.005)$.*
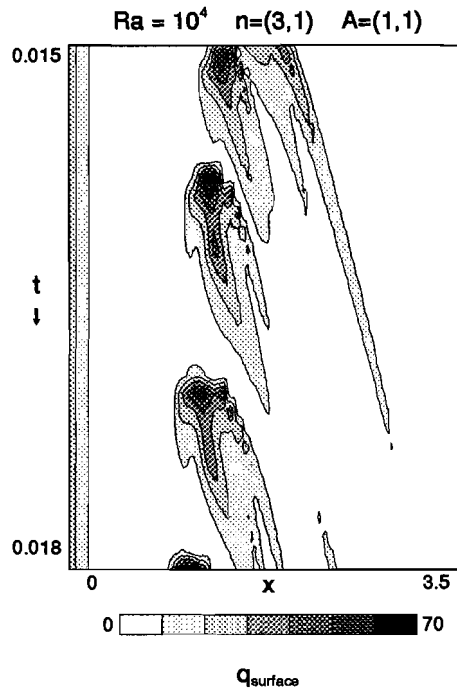
Ra = 10^4 n=(3,1)   A=(1,1)

Figure 6.4 *The temporal evolution of the local surface heat-flux for case A. Heat-flux is non-dimensionalized by $k\Delta T/d$, where k and ΔT are respectively the thermal conductivity, and temperature difference across the layer depth d. Time advances downward.*

transported very efficiently in the upper mantle as a consequence of the lower effective viscosity of the upper mantle and the drop in viscosity as a consequence of the stresses produced by the local thermal instability. As the supply of hot material from the lower mantle is at a much lower rate, it takes time for the thermal boundary layer to form again, after most of the hot material has been extracted from the interface. From comparing the first and last snapshot, one obtains a distinct impression of the periodic nature of this flow. The sharp decrease in viscosity as a consequence of the thermal instability is indicated in the extrema in the stream function, of which the amplitude increase by a factor of nearly four. The diapiric events take place on a much shorter time scale than the overturn time associated with the large-scale circulation. The periodicity of this pulsating mechanism is more evident in the plots shown below (figure 6.6). An effective Ra of between 10^4 and 10^5 for the lower mantle may not be all that unreasonable, when one takes into consideration the combined effects of a viscosity increase of 10 to 50 [Hager & Richards, 1989; Ricard & Wuming, 1991], a decrease of thermal expansivity of

6 [Chopelas & Boehler, 1989], and an increase of lattice thermal conductivity in the lower mantle of around 4 to 6 [Brown, 1986; Osaka & Ito, 1991].

In figure 6.4 we show the temporal development of the surface heat-flux q_s. From the grey scale contours one can readily discern the discrete pulses of heat arriving at nearly the same spot. The heat-flux associated with these thermal events (around 60) is nearly an order of magnitude greater than the background value of 7. It is also interesting to observe the effects of the excess heat-flow being propagated with time. A trail of high heat flux is left along x with time. Surrounding hotspot swells are typically anomalous heat flow patterns. This model shows the phenomenon of basal reheating of the lithosphere [Detrick & Crough, 1978; Menard & McNutt, 1982], which is based on field observations of the Hawaiian swell [Detrick et al., 1981].
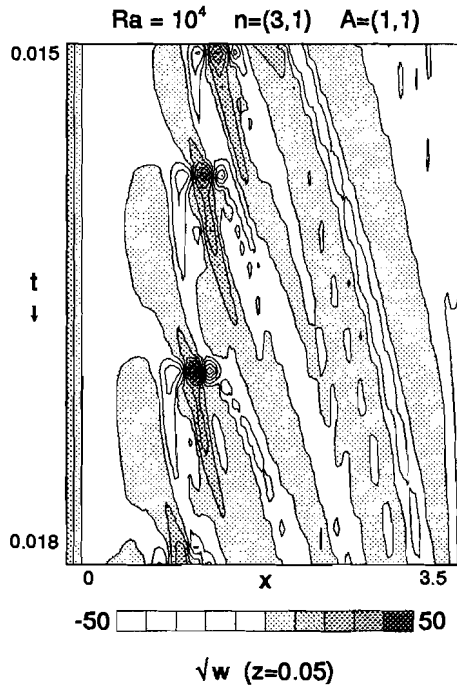
Figure 6.5 *Time history of the vertical velocity at a depth $z = 0.05$. We have plotted the sign of the square root of the vertical velocity component, with all descending velocities ($w < 0$) being whitened (see greyscale). Velocity is non-dimensionalized by thermal diffusivity and the depth of the layer in the usual way.*
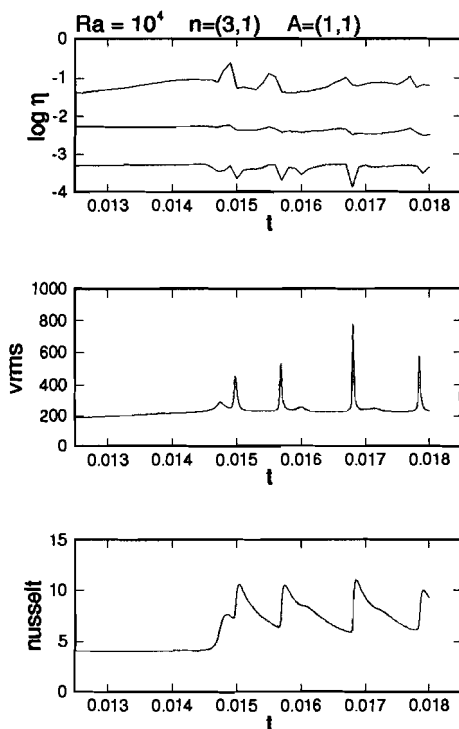
Figure 6.6 *The time history of the viscosity, root-mean-squared velocity V_{rms} and the surface Nusselt number for case A.*

Figure 6.5 displays the temporal evolution of the vertical velocity along x at a depth of $z = 0.05$ which is within the thermal boundary layer, since the time averaged Nusselt (Nu) number at the surface is around 7 (see figure 6.6). The close correlation between peaks of the surface heat flow (figure 6.4) and the vertical upwellings at the base of the lithosphere indicate that thermal advection is the dominating mechanism responsible for the local heat-transfer at these 'hot spots'.

Figure 6.6 summarizes the temporal evolution of the viscosity field, the root-mean-squared velocity V_{rms} and the surface Nu. The sharp spikes of the thermal events are well recorded by V_{rms}, where amplification by a factor of 4 is found. The surface Nu displays peaks with smaller amplitudes and behaves in a fashion that is similar to a non-linear oscillator by the form of a slow relaxation followed by a rapid rise. Temporal variations of the surface Nu are much smaller than those associated with the local heat-flow values q_s shown in figure 6.4. In strongly time-dependent flows there is a large disparity between the local $q_s(x, t)$ and Nu based
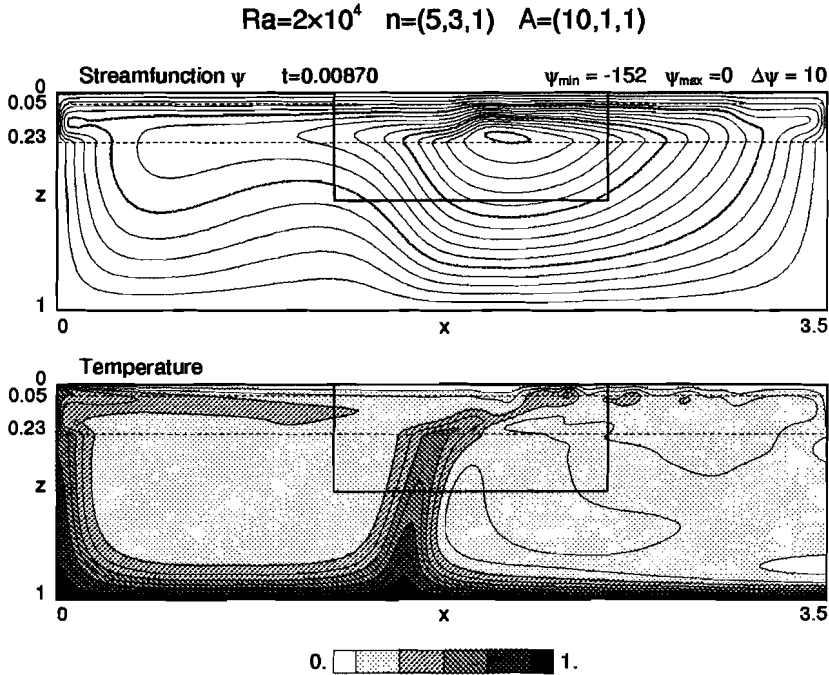
Figure 6.7 *Global snapshots of ψ and T for model C. Model C has a lithosphere which extends to z = 0.05. The power law indices n(z) are 5 for lithosphere, 3 for the upper mantle and 1 for the lower mantle. The box represents zoom-in snapshots to follow. Note the hot wide patch at the left being pulled by the large-scale circulation in the upper mantle.*

on the horizontal average. It is therefore important to recognize this distinction in the application of the usual heat-transfer scaling relationships to local and global geological phenomena. Changes in the viscosity field reflect the stress variations generated during these pulsing events. The average value of the viscosity (middle curve) does not vary as much as the extrema (top and bottom curves). The contrast of the averaged viscosities between the upper and lower mantle is 200 for case A.

Model C (with lithosphere, non-Newtonian upper mantle and Newtonian lower mantle)

More plate-like behaviour can be brought out by introducing a thin top layer with a larger power law index of $n = 5$ [Van den Berg et al., 1991]. For the time-

dependent case we have used a $n(z)$ of $(5,3,1)$ and a $A(z)$ of $(10,1,1)$ for Ra of 2×10^4. The global snapshot is shown in figure 6.7. From the stream function the more plate-like characteristics of this model C compared to case A is clearly manifested. There is now a hot tongue emanating from the edge plume. This hot flat patch is pulled quite strongly by the large-scale circulation produced by the presence of the mobile lithosphere. Its hot tip nearly reaches the middle plume where the diapiric structures are developed. The thermal anomalies developed from the rheological interface for case A and C are diapiric in nature because they consist of detached blobs and do not form a continuous conduit.

$$Ra = 2 \times 10^4 \quad n=(5,3,1) \quad A=(10,1,1)$$
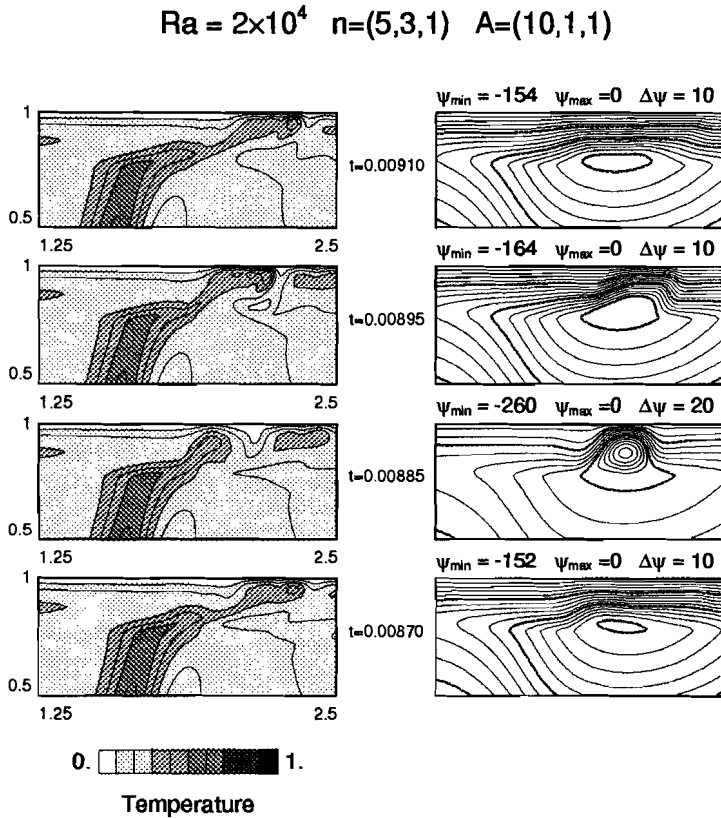
Figure 6.8 *Sequence of close-up snapshots of T and for model C. Time scale for pulsating event is around 0.0004 which is shorter than the overturn time of large-scale background circulation.*

Diapiric structures can also be formed under a wide variety of circumstances, such as in the interior of the cell for high Rayleigh number convection with Newtonian and non-Newtonian rheologies [Hansen et al., 1992; Malesvky & Yuen, 1992] and at phase-boundaries [Liu et al., 1991]. Here we have shown another mechanism based on changes in the rheological laws.

Figure 6.8 shows a sequence of temporal snapshots which have been zoomed around the central plume. Again, the episodic nature of this diapiric shedding process is illustrated by the development in T and ψ. Time scales for these diapiric outbursts are short relative to that for the large-scale circulation. The lithosphere acts to control the upstream flow of plume material beneath the plate. The pulsating nature of this flow is further demonstrated by the time histories of q_s and the vertical velocity w in figures 6.9 and 6.10.

The presence of the lithosphere brings in another time scale, owing to the thermal diffusion time of the plate with finite thickness. The periodicity of the pulses
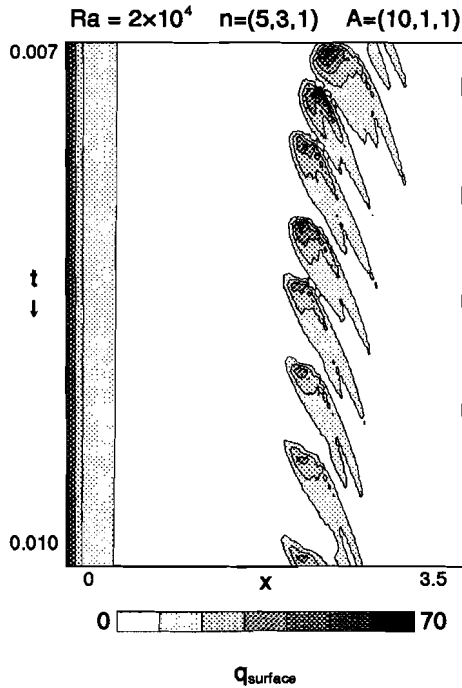
Figure 6.9 *Time history of local surface heat-flow for case C.*
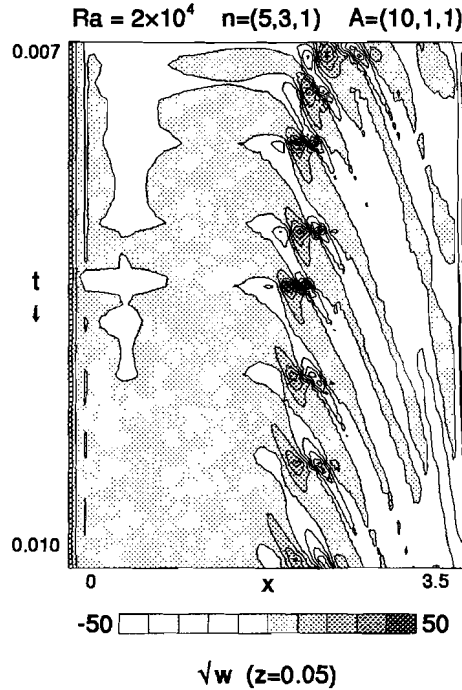
Figure 6.10 *Time history of the vertical velocity at the base of the lithosphere (z = 0.05) for case C. Otherwise, same convention used as in figure 6.5.*

in case C is reduced relative to case A because of the finite thickness of the lithosphere and the higher Ra. The effects of lithospheric shielding on the surface heat flow are clear from comparing figures 6.4 and figures 6.9. This low-pass filtering mechanism of the lithosphere on surface thermal signatures is thus illustrated. The presence of the lithosphere also helps to maintain better the stationarity of the diapiric signatures on the surface, as can be observed by comparing case A and C (see figures 6.4, 6.5, 6.9 and 6.10).

The time histories of the viscosity field, V_{rms} and the surface Nu for case C are shown in figure 6.11. The average viscosity contrast between the upper and lower mantle is about 200. The spiky character of non-Newtonian flows [Christensen & Yuen, 1989; Malevsky & Yuen, 1992] is clearly displayed where the time scales are shorter than for the case without the lithosphere (compare with figure 6.6).
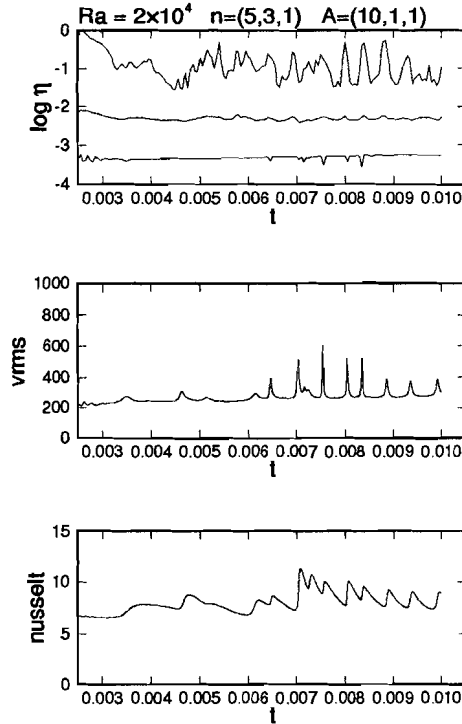
Figure 6.11 *Time history of the viscosity, V$_{rms}$, and surface Nu for model C.*

Model H (Newtonian viscously stratified)

One may well wonder whether or not a viscosity stratification in a purely Newtonian medium can also produce diapiric structures from the impingement of an ascending plume on an interface with a viscosity contrast of $O(10^2)$. Figure 6.12 shows the global shot taken from a Newtonian model with a viscosity jump of 200 and *Ra* of 2×10^4. Again, this simulation was started from a steady-state solution perturbed by a thermal perturbation with amplitude of 0.05 and harmonic variations having fundamental wavelengths along both directions.

Comparing figures 6.2, 6.7 and 6.12, we see that there are some differences in the flow patterns and temperature fields between a purely Newtonian rheological (case H) and the composite (case A and C) rheological models. The hot tongue so prominent in case C is now absent in the Newtonian model, because the large-scale
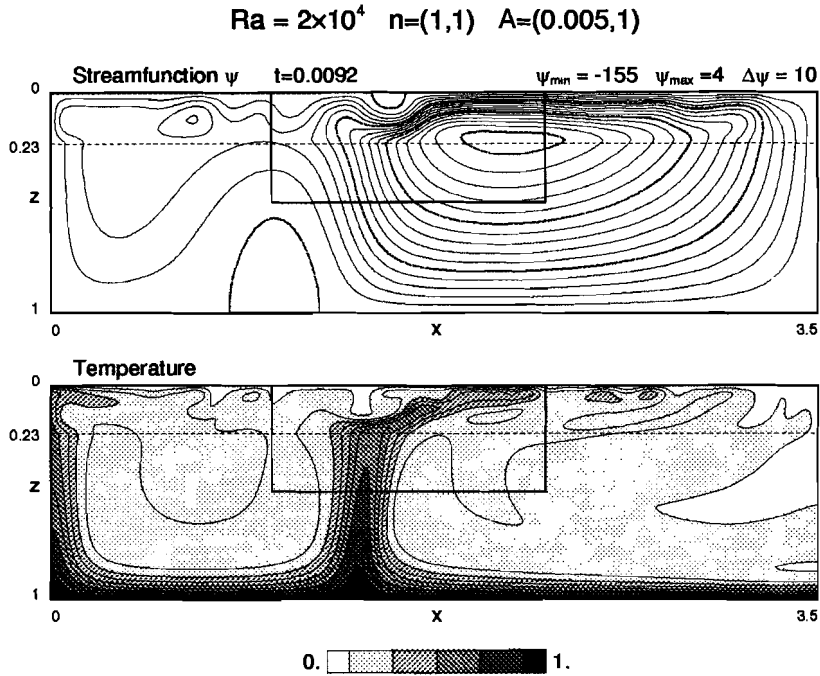
Figure 6.12 *Global snapshot of* ψ *and T for Newtonian model (H). The lower mantle is 200 times more viscous than the upper mantle. Note that the hot tongue from the plume at the left is small because of the more sluggish flow there.*

circulation is not as coherent and strong in drawing out hot anomalies, as in the case with the lithosphere. An important difference with the non-Newtonian models is the large number of spontaneous downwellings from the upper boundary layer.

Figure 6.13 shows the evolution of the plume as it interacts with the interface. Again the hot material is being extracted from the interface faster than it is supplied, showing that the viscosity decrease is the fundamental reason for the formation of these diapiric structures. Differences exist, in that the plumes developed off the interface are broader and remain in one piece closer to the surface, as the local stress-induced viscosity decrease is absent in these Newtonian models. From the snapshots of the stream function in figure 6.13 it is clear that the pulsating flow is much less vigorous than in the cases with the non-Newtonian mantle. This point is further emphasized by the temporal portrayal of the surface heat flow and the vertical velocity near the top (figures 6.14 and 6.15). The differences in the fluctuating intensity, periodicity, and the plume stationarity between case A and H are striking.
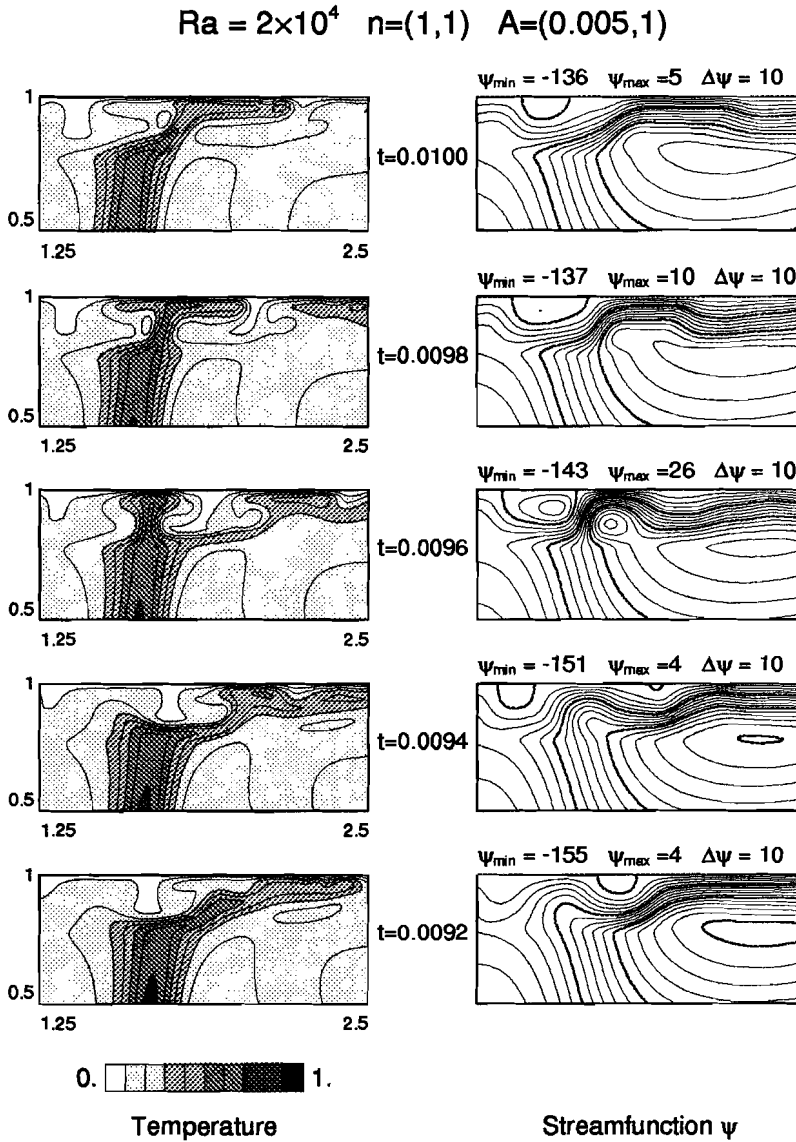
Ra = 2×10⁴   n=(1,1)   A=(0.005,1)

Figure 6.13 *Sequence of snapshots depicting T and ψ of the Newtonian model (H).*

The Newtonian signals are much more diffused and tend to drift more. The nature of the diapiric flow is more episodic than periodic. The spontaneous downwellings give rise to the noisy character of q_s and w.
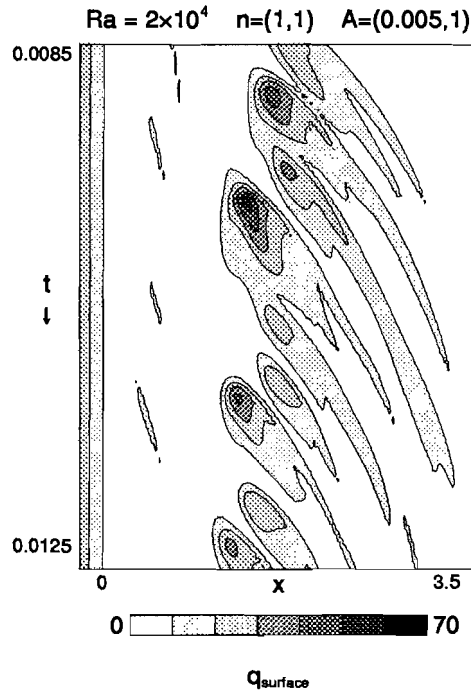
Ra = 2×10⁴   n=(1,1)   A=(0.005,1)

Figure 6.14 *Same as for figure 6.4 except for Newtonian rheology.*

Figure 6.16 summarizes the more sluggish Newtonian behaviour by showing the temporal evolution of V_{rms} and the surface Nu. Its departure from the spiky time series in figures 6.6 and 6.11 is quite evident.

6.4 Discussions and geophysical implications

The principal aim of this study was to investigate the effects of changes in creep laws, as suggested by recent experimental work on perovskite analogues [Karato & Li, 1992], on the dynamics of time-dependent mantle flows. We wished to see what sort of flow structures would result from the interaction of a rising plume and a rheological interface, and whether these secondary plumes penetrate the upper mantle and manifest themselves as hotspots on the Earth's surface.

   We found some new features in plume dynamics not encountered previously in
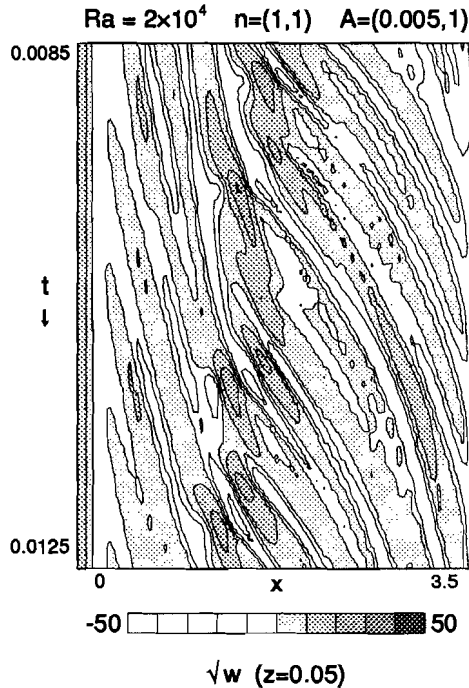
Figure 6.15 *Same as for figure 6.5 except for Newtonian model.*

time-dependent simulations with a homogeneous rheology throughout the mantle. These include (1) pulsating diapiric structures as a consequence of the viscosity decrease in the upper mantle, (2) fast time scales of the diapirs relative to those associated with the large-scale circulation, (3) the relative stationarity of recognizable surface heat-flow anomalies in models with a lithosphere, and (4) the stabilizing influences of plates in modulating the upstream flow of rising plume material beneath the plate [Schilling, 1991].

In addition to these points we have shown the importance of a non-Newtonian upper mantle and lithosphere in maintaining plate-like behaviour in time-dependent convection, which helps to generate coherent large-scale circulation in the upper mantle. This flow, in turn, can entrain hot anomalies away from a rising plume. Such shallow hot patches have recently been observed beneath the East Pacific from surface wave tomography [Zhang & Tanimoto, 1992]. The correlation of the horizontal extent of the negative seismic velocity contour with spreading rate [Zhang & Tanimoto, 1992] argues strongly for the dynamical role played by plate motions in pulling out hot patches from the ridge. On the other hand, Newtonian
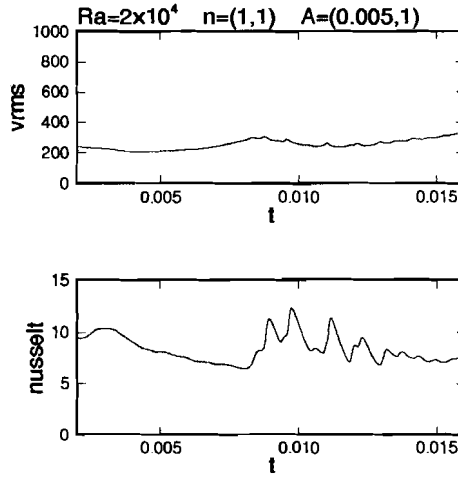
Figure 6.16 *Same as for figure 6.6 except for Newtonian model.*

viscously stratified models do not produce pronounced broad hot patches in the upper mantle.

The question arises whether this kind of diapiric upwellings can explain the periodicity in volcanism along the hot spot chains. In figure 6.17 we show a comparison of the surface heatflow q_s for the three models, in which the parameters are dimensionalized. The periodicity of the upwellings varies between 100 Myr (case A) to 30 Myr (case C), which is more than an order of magnitude larger than the period of volcanism, that is, for example, observed in the spacing between the Hawaiian islands (1-2 Myr). From the speed with which the thermal signals travel along the top boundary, we can estimate a plate velocity of approximately 1 cm/yr, which is at the lower bound of the observed present-day plate velocities.

An important parameter in controlling vigour of both the large-scale convection and the small-scale upwellings is the Rayleigh number. Increasing Ra will increase the frequency of the pulsations (compare e.g. model A with model C) and the magnitude of the plate velocity. The magnitude of the viscosity jump mainly influences the rate at which the hot material is extracted from the interface, especially in the cases of non-Newtonian viscosity, where the extraction rate is much faster than the supply rate. Decreasing the average viscosity in the upper mantle (or increasing the stress-induced drop in local viscosity by increasing the powerlaw index n) will tend to speed up the diapirs in the upper mantle; the period between the diapirs is however determined by factors governing the supply rate (the viscosity of the lower mantle and the vigour of convection), defined by the Rayleigh
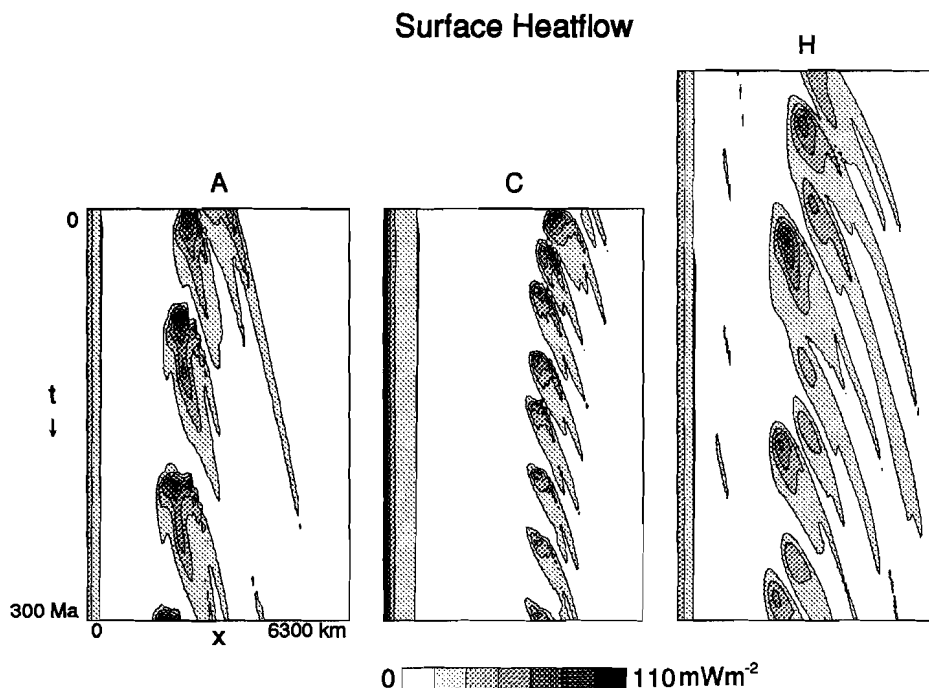
Surface Heatflow

Figure 6.17 *Comparison of the dimensionalized heatflow characteristics for the three cases. The scheme for dimensionalization is given in figure 6.2.*

number. Our choice of Ra is conservative. It would be more realistic to choose the Rayleigh number a factor of 10 higher. Exploring the behaviour of these layered models with higher Ra is however strongly limited by computational time. Smaller spatial and temporal discretization must be used to resolve these small scale features, and these 2-D calculations challenge the limits of present day computers.

Many interesting new consequences arising from vertical variations in the creep laws have been discussed here. Important features for inclusion in future studies would be temperature- and pressure-dependent viscosity and depth-dependent thermal expansivity, as depth-dependent properties in Newtonian convection have been shown to stabilize the upwellings [Yuen et al., 1991; Hansen et al., 1991]. Phase transitions can also influence the dynamics of the diapiric structures [Liu et al., 1991]. The development of plume structures are shown to be strongly affected by the change in mantle rheological laws across the lower mantle-upper mantle boundary. Taken together with effects from phase transitions [Liu et al., 1991], this type of rheological layering, non-Newtonian on top of Newtonian,

may really help to promote diapiric flows in the upper mantle with fast time scales.

The seismological discontinuities in the upper mantle can be related to phase changes. Their combined thermodynamical and rheological effects can be envisaged to modulate the behaviour of upwelling diapirs and to bring shorter time scales into play as a consequence of the shorter distance to the surface.

Acknowledgements

Chapter 7

The effects of shallow rheological boundaries in the upper mantle on inducing shorter time scales of diapiric flows †

P.E. van Keken, D.A. Yuen and A.P. van den Berg

Abstract

We have studied the effects of rheological boundaries in the upper mantle on the dynamics of inducing pulsating diapiric plumes. We have compared the effects due to shallower rheological interfaces in the upper mantle on the time scales of the pulsations. Comparing with a basic model with a rheological interface at 670 km depth, we find that time scales between pulsations can be reduced considerably down to a few million years by adding another rheological boundary at 400 km depth. These results suggest that short time scale diapiric flows may be generated from relatively stationary upwellings from the lower mantle because of the presence of rheological boundaries in the shallow upper mantle.

7.1 Introduction

Phase boundaries have been recognized for a long time as being important for mantle dynamics [Vening Meinesz, 1962; Verhoogen, 1965; Christensen & Yuen, 1984]. It is only recently that rheological boundaries separating creep regimes have been identified in the laboratory [Karato, 1988; Karato & Li, 1992; Karato, 1992]. Its ramifications on mantle flows can be tremendous, as seen from the recent results by Van Keken et al. [1992], who studied the interaction between a mantle plume and the 670 km discontinuity as a rheological boundary. Diapiric instabilities with short time scales, as compared with over-turn time, were found to develop from this rheological boundary. In this work we will show how shallower transitions can introduce shorter pulsations. As rheological boundaries can be shallower than phase boundaries, they may serve as a shallow site for producing diapiric flows with very short time scales.

7.2 Model description

We model the mantle as an incompressible viscous fluid medium at infinite Prandtl number in the Boussinesq approximation. A non-Newtonian upper mantle lies over an Newtonian lower mantle. The dimensionless depth-varying creep law used in the computations is given by
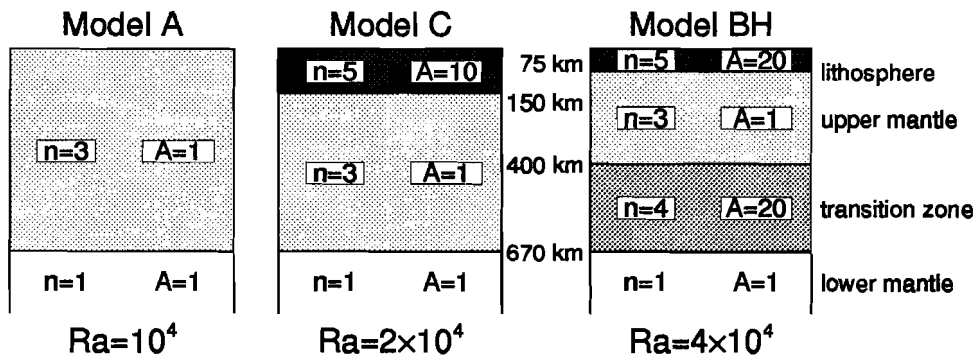

Figure 7.1 *Specification of the rheology parameters A(z) and n(z), and the thermal Rayleigh number Ra, based on the lower mantle viscosity, for the three models.*

$$\sigma_{ij} = A(z) \, \dot{\epsilon}^{1/n(z)-1} \dot{\epsilon}_{ij} \tag{7.1}$$

where σ_{ij} and $\dot{\epsilon}_{ij}$ are the elements of respectively the deviatoric stress and strain-rate tensor, $n(z)$ represents the depth variation of the power law index n in the mantle creep law, $A(z)$ is the pre-exponential factor which varies with depth, and $\dot{\epsilon}$ is the second invariant of the strain rate tensor. The non-dimensional differential equations describing conservation of mass, momentum and thermal energy are solved using a primitive variable finite element method, described in [Van den Berg et al., 1991; Van Keken et al., 1992]. The important control variables are $n(z)$, $A(z)$, and the thermal Rayleigh number Ra. Calculations are performed in a rectangular box with aspect ratio of 3.5.
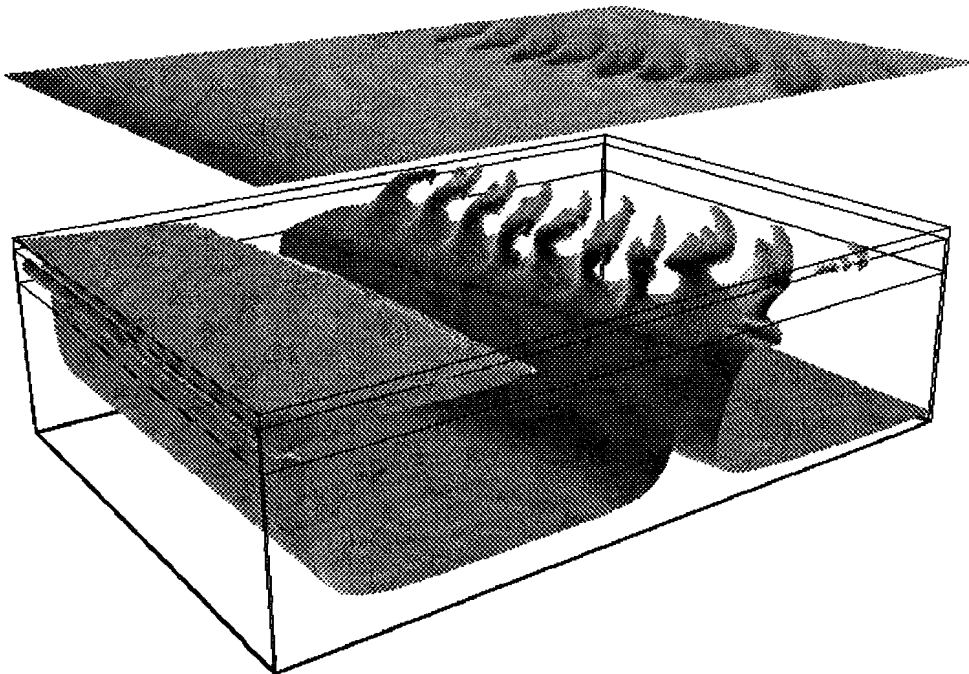

Figure 7.2a *Temporal development of the three-layer model C. Time progresses along the third axis, away from the viewer. In the lower frame the isosurface of temperature $T = 0.35$ is shown. Distinct diapiric structures are formed at the interface from the stationary plume in the lower mantle. The diapiric pulses correlate well with the peaks in the surface heat flow, shown in the top frame.*

The three models considered in this work are depicted in figure 7.1. Model A and C are the non-Newtonian models used in [Van Keken et al., 1992]. In the third model, BH, we have included a representation of the 'hard garnet' rheology that has been proposed for the transition zone between 400 and 670 km depth [Karato, 1989; Meade & Jeanloz, 1990]. Increasing $A(z)$ makes the rheology intrinsically harder. The thermal Rayleigh number (shown in figure 7.1) is based on the lower mantle Newtonian viscosity [Van den Berg et al., 1991], and increases from $Ra = 10^4$ for model A to $Ra = 4 \times 10^4$ for model BH.

7.3 Results

Snapshots displaying the development of temperature and stream function have already been displayed in [Van Keken et al., 1992] for models A and C. More detailed dynamics can be observed in a video available from the authors. Figure 7.2a shows the development of model C in a different way. The temporal evolution of the 2-D model is now depicted in a 3-D figure, in which time evolves in the third direction, pointing away from the viewer. The isosurface of $T = 0.35$ is shown. The interior of the plume is relatively cold. This cold origin is due to the cold tongue produced by the plate-like character of the upper boundary layer [Van den Berg et al., 1991; Lenardic & Kaula, 1993], that enables the long extension of the cold mass at the bottom. Features present in the data by Van Keken et al. [1992], can be identified in figure 7.2a. From the stationary upwelling at the left hand side a long flat patch can be seen, showing the strong pulling motion of the large scale circulation due to the presence of the mobile lithosphere. From the upwelling lower mantle plume in the center, discrete thermal anomalies are shedded off the interface and drawn away from the plume by the large scale circulation. The diapirs consist of detached blobs and do not form a continuous conduit.

If the parameters are dimensionalized using a model mantle depth of 1800 km (accounting for the spherical to cartesian transformation) the pulsating behaviour of the plume in model C is shown for 300 Myr; the period between the pulsations is approximately 35 Myr. The viscosity in the upper mantle is on average 200 times lower than the viscosity in the lower mantle for both model A and C. In model C, the viscosity in the lithosphere changes drastically from stagnation zones, where the viscosity is around 1000, to the positions at the boundaries and above the mantle plume, where the strong shearing motion decreases the viscosity drastically in this strongly non-Newtonian ($n = 5$) medium. The average viscosity of the lithosphere is around 1, corresponding to a dimensional viscosity of 10^{22} Pa $\cdot$ s.

Figure 7.2b gives a similar view of the evolution of model BH, which is shown for dimensional time of 75 Ma. The isosurface for $T = 0.42$ is shown. The
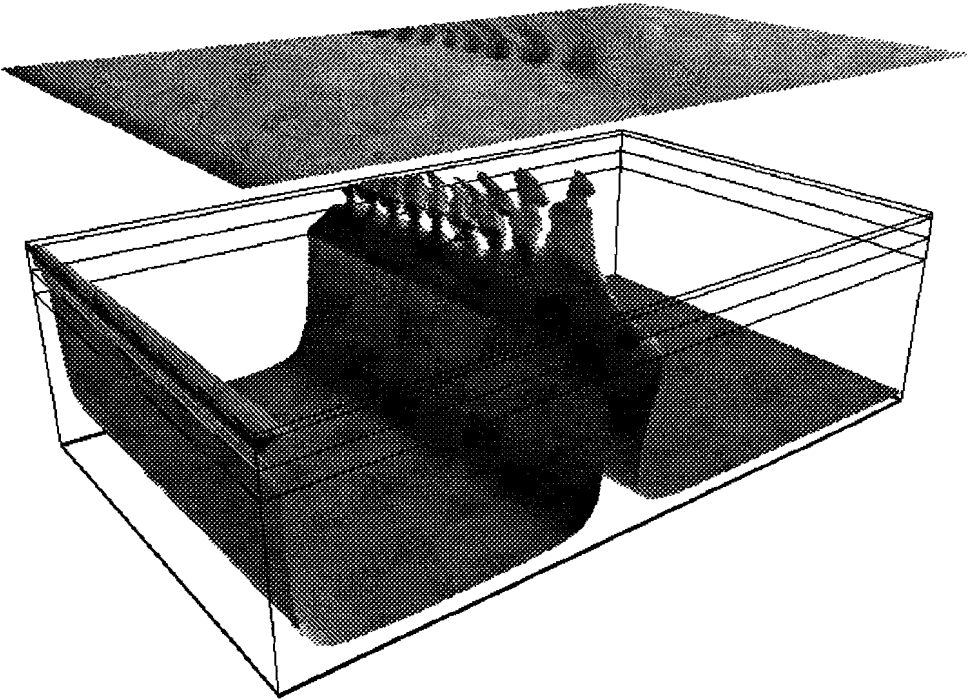
Figure 7.2b *A similar view as in figure 7.2a, but now of the four-layer model BH. The iso-surface is for T = 0.42. Very sharp diapiric structures are now formed at the 400 km discontinuity. Period between the pulsations is approx. 4 Myr.*

average viscosity in each layer is 5 in the lithosphere, 1/300 in the upper mantle, and 1/4 in the transition zone. Above the first discontinuity at 670 km, the hot material contained in the plume can travel faster than in the underlying lower mantle. In model C this leads to periodic instabilities off the boundary layer that is formed on top of the plume at the 670 km discontinuity. In this model BH, the viscosity contrast across 670 is much smaller (1/4 as compared to 1/200) and the faster transport leads only to a thinning of the plume in the transition zone, which remains stationary in time. At the top of the transition zone, at 400 km depth, the viscosity contrast is approximately 1/80. Here the much faster transport of the hot material, helped by the non-Newtonian effects, leads again to the periodic pulsating flow. The discrete diapirs originating off the 400 km discontinuity are clearly visible in figure 7.2b. The 'hot tongue' emanating from the stationary upwelling at the left hand side boundary, prominently present in figure 7.2a, is strongly reduced in model BH (figure 7.2b). This is a consequence of the higher temperature indicated

by the isosurface, and the less dynamic large scale flow, caused by the thinner lithosphere (75 km as compared to 150 km), and the higher viscosity in the transition zone.

In Figure 7.3 we show a comparison of the dimensional surface heat flow as observed in the models A, C and BH. A common feature in the three models is the periodicity of the diapiric upwellings and the relative stationarity of the plume in the lower mantle. The periodicity decreases, from around 80 Myr for model A and 35 Myr for model C, to approximately 4 Myr for model BH. This increase of frequency is a consequence of the higher Rayleigh number (figure 7.1) and the shallower origin of the diapirs.

Figure 7.4 shows the maximum vertical velocity as observed in the direct vicinity of the upwelling plume The dramatic decrease in the period between the diapirs between models C and BH is clearly visible. The maximum vertical velocity increases strongly from 3 cm/yr for model A and 4 cm/yr for model C to more than 15 cm/yr for model BH, again demonstrating the dynamical effect induced by the shallower level of the rheological interface. The velocities are much higher in
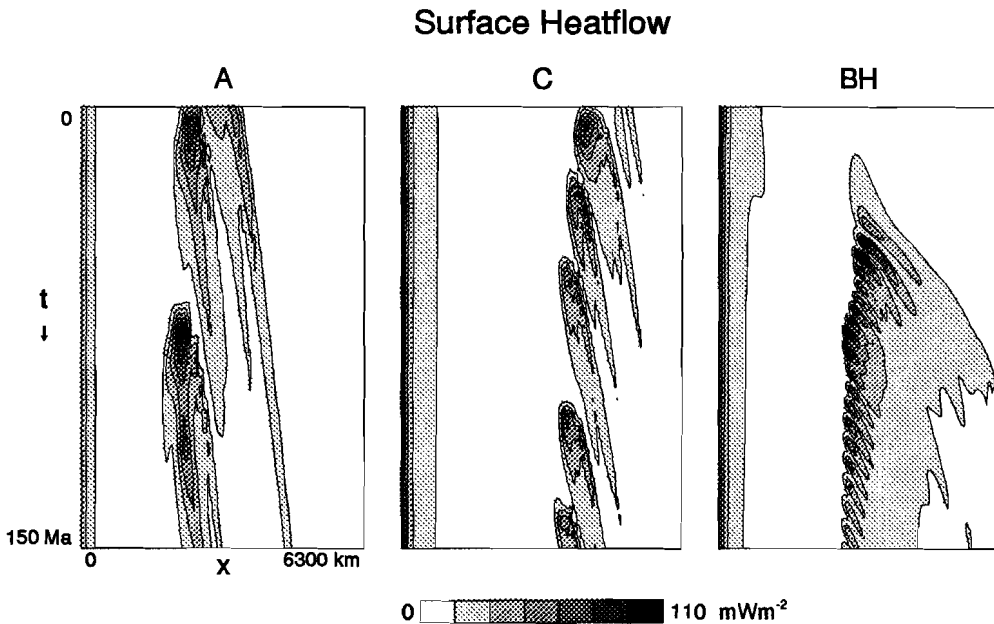

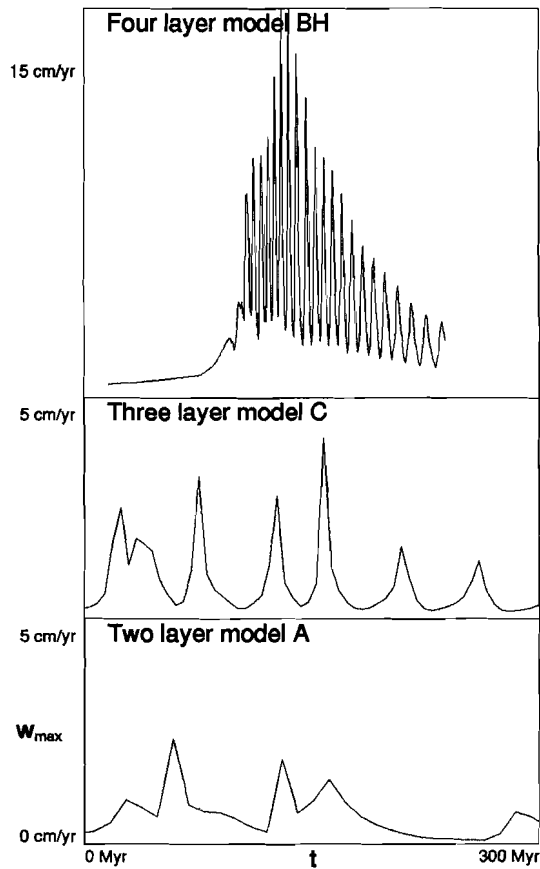Figure 7.3 *Comparison of dimensional surface heatflow for the three cases.*

Figure 7.4 *Comparison of maximum dimensional upward velocity around the plume. The pulsating flow is much more frequent and faster for the four-layer model BH, than for the models A and C.*

case BH compared with case A, but less volume is carried, resulting in approximately equal heat flow maxima above the diapirs for the two cases (figure 7.3). Heat flow maxima for models BH and A are around $110 \, mW \cdot m^2$, close to an order of magnitude greater than the mean heat flow.

7.4 Discussion

In this work we have demonstrated the importance of rheological boundaries in upper mantle dynamics. An important feature of the dynamical models is the pulsating diapiric flow, that produces discrete upwellings of hot material at a steady position under a moving lithospheric plate. This kind of behaviour is observed in hot spot volcanism of the type exemplified by the Hawaiian [Schilling, 1985] and Galapagos islands [Christie et al., 1992]. Thermodynamic phase transitions can also cause diapiric flow, but their behaviour is not as regular [Liu et al., 1991; Zhao et al., 1992]. These type of models demonstrate that depth varying creep laws can explain, at least to some extent, the coexistence of a large scale flow, as observed by the plate motions, and persistent small scale 'hot spots', as observed underneath mid-oceanic island chains. Both are expressions of the advective cooling of the Earth and seem to behave independently of each other at the time scales, less than 200 Myr, considered.

The pulsating behaviour of mantle upwellings is a consequence of the viscosity decrease over a rheological boundary, and in itself independent of the type of large scale flow, whether it is whole, layered or intermittent mantle convection. Furthermore, one can expect that at shallow levels, less than 400 km, rheological transitions occur that are not connected with the major thermodynamical phase transitions between 400 and 670 km depth [e.g., Karato, 1992]. The shallower level of a rheological boundary can be envisaged to induce diapiric instabilities with time scales shorter than those found in present models. This mechanism might well be used to explain the temporal variations in magmatic activity as observed e.g. underneath island chains [Schilling, 1985; Christie et al. 1992], asthenospheric upwellings in rift zones [Tatsumi & Kimura, 1991], and at mid-oceanic ridges [Batiza et al., 1992; Gente et al., 1992].

Acknowledgements

Chapter 8

Cooling of the Earth in the Archaean

8.1 Introduction

There is still considerable controversy over the mantle temperature during the Archaean (approx. 3.5-2.7 Gyr B.P.). On the one hand, high mantle temperatures are inferred from the occurrence of very magnesian komatiitic lavas, that are widespread in most Archaean greenstone belts, but rarely found after the Archaean-Proterozoic transition at 2.7 Gyr. These komatiites indicate high extrusion temperatures and melting temperatures some 400-500 K in excess of today's mantle temperatures. Some have taken this indicative of the average mantle temperatures [Sleep, 1979; Nisbet & Fowler, 1983; Vlaar, 1986]. Others assume the average mantle temperature to have been only 200-300 K higher than at present [Sleep & Windley, 1982; McKenzie, 1984; Jeanloz & Morris, 1986] and take the komatiite occurence to be the consequence of hotspot activity. A third group proposes even lower temperatures for the Archaean [Campbell & Griffiths, 1992]. On the other hand, the temperatures at 50-100 km depth in the Archaean continents, as have been derived from high-grade terrains, indicate conditions that have not been very different from the present day situation. This 'Archaean paradox' has led many investigators to models in which cooling of the hotter Earth took place through rapid convection underneath the oceans. In most of these model studies it is implicitly assumed that mantle convection models can simulate present day plate tectonic processes, and that plate tectonics has been operative in the Archaean [e.g., Bickle, 1978; Davies, 1979; Schubert et al., 1980; Sleep & Windley, 1982]. However, the present day tectonic plate forces of 'slab pull' and 'ridge push' are strongly dependent on lithospheric age and hence on lithospheric recycling rate and mantle temperature. A uniformitarian extrapolation of present conditions to the Archaean may not be valid [Vlaar, 1985; 1986] and therefore, a different approach has to be adopted [Vlaar et al., 1993].

First, we will consider some previously published thermal cooling models of the Earth which have been used to constrain Archaean mantle temperatures. Next, the influence of higher temperatures on the pressure-release melting of mantle diapirs, and the related changes in upper mantle dynamics are considered. Finally,

we will present a model for the dynamics of the oceanic lithosphere and discuss its applicability to the cooling of the Earth in the Archaean.

8.2 Cooling models for the Earth based on parameterized convection

Several authors have studied thermal histories of the Earth using parameterized mantle convection models. In these, the change of average mantle temperature with time follows from the energy balance equation:

$$\tfrac{4\pi}{3}\, \rho c_p (R_m^3 - R_c^3)\, \frac{dT}{dt}\; =\; -4\pi q R_m^2 + \tfrac{4\pi}{3}\, Q(R_m^3 - R_c^3) \tag{8.1}$$

where q is the average heat flux out of the Earth's surface and Q is the average heat production in the mantle. The definition of the other parameters is given in table 8.1. The heat flux from the core into the base of the lower mantle is probably small [Stacey, 1977] and is neglected by most authors. For the mantle the Nusselt number Nu can be defined as the ratio of the total heat flux to the conductive heat flux out of the mantle

$$Nu\; =\; (q_{cond} + q_{conv})/q_{cond}\; =\; qD/k\Delta T \tag{8.2}$$

where ΔT is the temperature difference across the mantle. The relation between the Nusselt number and the vigour of convection in the mantle, which has been

Table 8.1 Notation and nominal values

Parameter	Definition	Value
g	gravitational acceleration	$9.8\ \mathrm{ms^{-2}}$
α	thermal expansivity	$3 \times 10^{-5}\ \mathrm{K}$
κ	thermal diffusivity	$10^{-6}\ \mathrm{m^2 s^{-1}}$
D	Depth of convection layer	$2.8 \times 10^6\ \mathrm{m}$
v	kinematic viscosity	
η	dynamic viscosity	
v_0	Minimum kinematic viscosity	$2.21 \times 10^7\ \mathrm{m^2 s^{-1}}$
A	Activation temperature (γT_m)	$5.6 \times 10^4\ \mathrm{K}$
k	thermal conductivity	$4.2\ \mathrm{Wm^{-1}K^{-1}}$
ρc_p	volumetric specific heat	$4.2 \times 10^6\ \mathrm{Jm^{-3}K^{-1}}$
R_c	core radius	$3.471 \times 10^6\ \mathrm{m}$
R_m	mantle outer radius	$6.271 \times 10^6\ \mathrm{m}$
Ra_c	critical Rayleigh number	1100
T_s	surface temperature	$273\ \mathrm{K}$
β	power law exponent	0.3

exploited in parameterized convection models, is

$$Nu = (Ra/Ra_c)^\beta \tag{8.3}$$

where Ra is the mantle Rayleigh number and Ra_c is the critical Rayleigh number, $Ra_c \sim 10^3$. For a mantle heated entirely from below Ra is defined by

$$Ra = Ra_E = \frac{\alpha g(T - T_S)D^3}{\kappa\nu} \tag{8.4}$$

This definition has been used by Sharpe & Peltier [1978] to study the loss of primordial heat, initially stored in the core, through mantle convection. For a mantle heated entirely from within Ra is defined by

$$Ra = Ra_I = \frac{\alpha g Q(R_m - R_c)^5}{\kappa^2 \nu \rho c} \tag{8.5}$$

In (8.1) the lower boundary of the mantle is explicitly assumed to be insulated, and the second definition of the Rayleigh number, Ra_I, should be used. However, Schubert et al. [1980], Jackson & Pollack [1984,1987] and McGovern & Schubert [1989] have used the first definition, based on the claim of Schubert et al. [1980] that this was justified if T in (8.4) represents the characteristic temperature of the convecting region.

A temperature-dependent rheology of the form

$$\nu = \nu_0 \exp(A/T) \tag{8.6}$$

has been used in the models. The parameter A can be interpreted as an activation temperature. Several formulations have been used to determine A, either using Weertman & Weertman's [1975] formulation based on homologous temperature ($A = \gamma T_m$, $\gamma \approx 30$), using activation energy ($A = E/R$), or both activation energy and volume ($A = (E + pV)/R$). Determination of the value of A, to be used in (8.6), from the formulations mentioned above is correct only for Newtonian fluids. In non-Newtonian fluids the activation temperature decreases with a factor n, an effect that has been neglected by several authors [e.g., Davies, 1979; Williams & Pan, 1992]. To include the effect of volatiles an effective A as a function of volatile content has been defined through the melting temperature T_m [Jackson & Pollack, 1987; Williams & Pan, 1992].

The general form of the heat production is

$$Q = Q_0 \exp(-\lambda t) \tag{8.7}$$

where λ is the decay rate of the radioactive material and Q_0 is the heat production at $t = 0$. Jackson & Pollack [1987] have used an effective λ to describe a mixture of several isotopes with different decay rates. Q_0 is not well known and in most calculations it has been used as a free parameter; Q_0 was varied to constrain the

present day heat flux at 70 mWm^{-2}, based on the estimate of oceanic heat loss [Sclater et al., 1980]. In contrast to this, Sleep [1979] and Stacey [1980] used the abundance of atmospheric ^{40}Ar to constrain absolute values of the concentration of ^{40}K and from that the concentrations of the other heat producing elements.

Substitution of (8.2)-(8.4), (8.6) and (8.7) into (8.1) gives

$$\frac{dT}{dt} = \frac{-3\left[\dfrac{\alpha g(T-T_S)D^3}{Ra_c \kappa v_0 \exp(A/T)}\right]^{\beta} k(T-T_S)R_m^2}{D\rho c_p(R_m^3 - R_c^3)} + \frac{Q_0}{\rho c_p}\exp(-\lambda t) \tag{8.8}$$

This non-linear differential equation can be solved numerically. A typical result is shown in figure 8.1, that shows the averaged mantle temperature and mantle heat flow as a function of age. A fourth order Runga-Kutta scheme with a constant step size of 10 Myr has been used to solve (8.8). The nominal values shown in table 8.1 and a decay rate $\lambda = 4.48 \times 10^{-10}$ yr^{-1} have been used. This decay rate corresponds to the time-averaged decay constant for a chondritic composition [Schubert et al., 1980]. The model run with $Q_0 = 220$ nWm^{-3} (bold line) yields a present day heat flow of 70 mWm^{-2}.

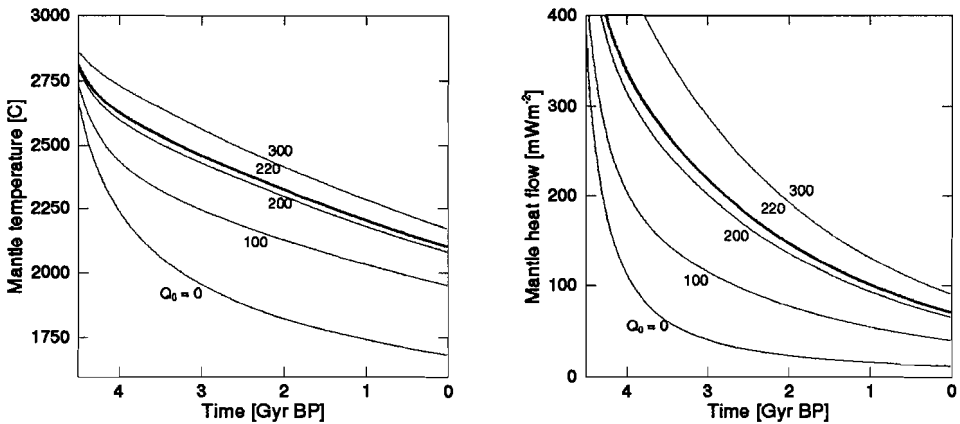Other models include different distributions of radioactive heat sources [e.g.,

Figure 8.1 *Example of evolution of internal mantle temperature and surface heat flow, based on parameterized mantle convection modelling (see text). Heat production is given by* $Q(t) = Q_0 \exp(-\lambda t)$, *where the decay constant* $\lambda = 4.48 \cdot 10^{-10}$ yr^{-1} *is for a chondritic composition [Schubert et al., 1980]. The initial heat production* Q_0 *is used as a free parameter.* $Q_0 = 220$ nW $\cdot$ m^{-3} *yields a present day heat flow of 70 mW $\cdot$ m^{-2}.*

Jackson & Pollack, 1984], volatile-dependent rheology and the de/regassing history of the Earth [McGovern & Schubert, 1989; Williams & Pan, 1992]. In general, the results show the strong self-regulating effect of the temperature- and volatile-dependent rheology on the dynamical cooling and a temperature decrease of 200-300 K since the Archaean. A lower estimate of the amount of cooling is made by Davies [1979], who derives from isoviscous models, that the Earth cannot have cooled by more than 100-150 K.

The assumptions and simplifications that have been used to make this analysis possible, make it difficult to judge the applicability of these models to the evolution of the Earth. One point of criticism applies to the employed Nusselt-Rayleigh number relationship, which in general does not take into account the effects of large aspect ratio convection [Hansen & Ebel, 1984], viscous dissipation [Steinbach, 1991], and depth variations in rheological [Hager, 1984] and thermodynamical properties [Chopelas et al., 1989; Osaka & Ito, 1991].

Another shortcoming of the models concerns the implementation of temperature-dependent rheology, as has been pointed out by Christensen [1984c; 1985]. He essentially indicates the importance of the rheology of the upper boundary layer in controlling the cooling of the Earth. As the surface temperature is assumed to have varied very little over geological times, the upper boundary layer may well have a rheology that is largely independent of the internal temperature. A consequence could be that the Nusselt number Nu would become independent of the Rayleigh number and heat flux would be constant throughout most of the Earth's history. As has been shown later, this effect might be less important for high Rayleigh number ($Ra > 10^8$) convection, for which the heat flow would become a function of Ra again, even for strongly temperature-dependent viscosity [U. Hansen, personal communication, 1993]. However, it is not clear if these high Rayleigh number convection results apply to the Earth, even in its early history.

In addition to this, Vlaar [1985; 1986] and Vlaar & Van den Berg [1991] have shown that the thicker basaltic and underlying depleted harzburgitic layer, that are created at higher mantle temperatures [e.g., Sleep, 1979], constitute a compositional boundary layer with a strong stabilizing influence, that might effectively prohibit plate tectonics in the way it operates today. This effect has been neglected thus far.

In order to study the thermal evolution of the Earth since the early Archaean, it is essential to incorporate these rheological and compositional properties of the upper thermal boundary layer. In present paper we will assume that the cooling of the Earth is completely governed by the dynamics of the upper boundary layer. Any sinking material is passively replaced by adiabatically upwelling mantle. This approach is similar to that of Sleep [1979], who used analytical half space cooling models, combined with estimates of the average age of the oceanic lithosphere, to study the thermal evolution.

8.3 Pressure-release melting

The process of pressure-release melting of undepleted mantle peridotitie plays an important role in the Earth. It is held to be the cause of the present day generation of basaltic oceanic crust at mid-ocean ridges. It is generally agreed upon, that in a hotter mantle the melting of a rising diapir starts at a deeper level and a larger volume of basaltic magma is formed [e.g., Sleep, 1979; McKenzie, 1984; Vlaar, 1985; Takahashi, 1990]. McKenzie & Bickle [1988] derive the thickness of the formed basaltic crust as a function of the potential temperature of the mantle, which is the absolute mantle temperature extrapolated along the adiabat to zero pressure. Estimates for the present day potential temperature range from 1280 °C to 1400 °C [Sleep, 1979; McKenzie, 1984; Christensen, 1985; Abbott et al., 1993]. The range indicates the uncertainties in eruption temperatures of basaltic magmas and in the temperature drop as a consequence of the latent heat consumption. An important effect that has not been implemented by McKenzie & Bickle [1988], is that the amount of melting will be influenced by the pressure that is exerted by the already formed basaltic crust. This will lead to considerably less production of basaltic crust upon pressure-release melting [Vlaar & Van den Berg, 1991].

Figure 8.2a illustrates the effect of higher mantle temperature on the melting of an adiabatically rising diapir, using the formalism developed by McKenzie [1984], corrected for the crustal pressure effect [Vlaar & Van den Berg, 1991]. Shown are the solidus and liquidus of mantle peridotite, each given as a third order polynomial fit to the data of Takahashi [1990], $T(p) = a_0 + a_1 p^1 + a_2 p^2 + a_3 p^3$. The coefficients can be written as a vector **a**. These are given, with pressure in Gpa and temperature in °C, by **a** = $(1136, 134.2, -6.581, 0.1054)^T$ for the solidus, and **a** = $(1762, 57.46, -3.487, 0.0769)^T$ for the liquidus. The dotted lines indicate lines of equal melting for 15 and 50 % melting, based on data from Jaques & Green [1980]. For the entropy of melting we used $\Delta S = 300 \text{ J} \cdot \text{kg}^{-1}\text{K}^{-1}$, which is approximately equivalent to 1 R J $\cdot$ mol(atom)$^{-1}$K^{-1} [Jeanloz, 1985; Miller et al., 1991]. The bold lines indicate the (T,p)-paths for rising diapirs at three different potential temperatures, T_{pot} = 1330, 1600, and 1750 °C. The present day situation, with a crustal thickness of 7 km, is simulated with T_{pot} = 1330 °C. The extrusion temperature here is T_{extr} = 1240 °C. At T_{pot} = 1600 °C, 29 km of basaltic crust is generated with T_{extr} = 1420 °C. At the highest potential temperature shown, T_{pot} = 1750 °C, melting of a rising diapir generates 50 km of basaltic crust with T_{extr} = 1520 °C. Note the strong effect of the consumption of latent heat on the extrusion temperatures. Although the potential temperatures differ by 420 °C, the temperatures at 50 km depth differ only by 280 °C.

Figure 8.2b shows the density in the underlying depleted harzburgitic residue for the three cases with different potential temperature. The density of the
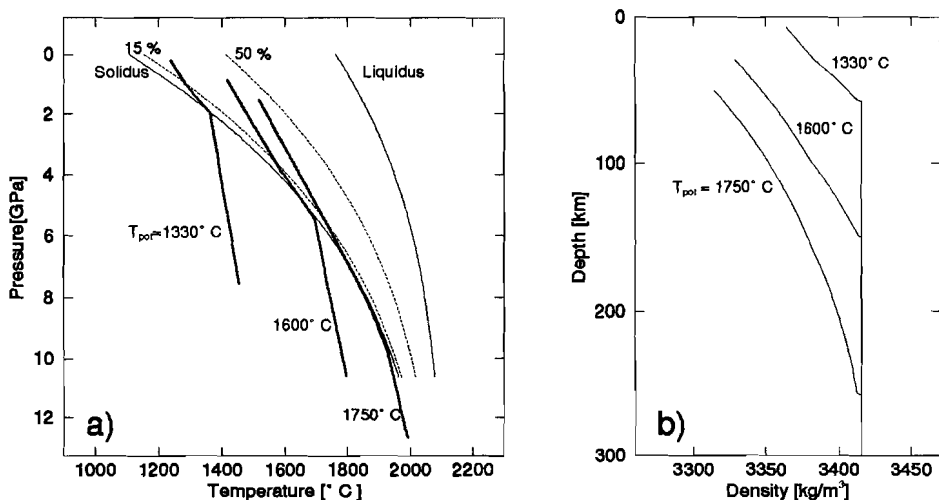
Figure 8.2 *a) The effect on higher mantle temperatures on the pressure-release melting of a adiabatically rising diapir. The solidus and liquidus of mantle peridotite are shown as a a third order polynomial fit (see text). Lines of equal melting for melt fraction 15 % and 50 % are shown, based on data by Jaques & Green [1980]. The thick solid lines indicate schematically the (T,p)-paths of a rising diapir at potential temperatures T_{pot} = 1330, 1600, and 1750 °C, based on McKenzie [1984]. In the calculations we have corrected for the crustal pressure effect [Vlaar & Van den Berg, 1991] (see text).*

b) Compositional density in harzburgite and lherzolite. Density increases with depth, as a consequence of the lower degree of depletion.

harzburgite increases with depth as a consequence of the decreasing amount of depletion. As has been shown by Vlaar [1985] and Vlaar & Van den Berg [1991], this compositional stratification has a large effect on the stability of the oceanic lithosphere.

In this scenario, komatiite might be the melt generated at considerable depth (>150 km) and low degrees of partial melting. At depth, the komatiitic magma separates from the matrix and rises adiabatically to the surface [O'Hara, 1975; McKenzie, 1984; Takahashi, 1990]. This can explain the occurrence of komatiites as the first extrusion product in greenstone belt formation, followed by outflows of less MgO-rich basaltic lavas [Nisbet, 1987].

In the following section we will discuss the consequences of this for the dynamics of the lithosphere in a hotter mantle.

8.4 Consequences for upper mantle dynamics

Vlaar [1985; 1986] presented qualitative constraints on Archaean global dynamics, which are summarized by the following:
i) The mantle was originally molten, shortly after accretion [e.g., Stevenson, 1989].
ii) Rapid solidification started at the bottom of the mantle and progressed upward [Miller et al., 1991], until the whole mantle was at or below the solidus temperature. iii) At high mantle temperatures, pressure-release melting of rising diapirs generates a thick basaltic layer on top of a very thick harzburgitic layer [Sleep, 1979; Vlaar, 1985; McKenzie & Bickle, 1988]. iv) Compositional stability [Vlaar, 1975; Vlaar & Wortel, 1976; Oxburgh & Parmentier, 1977] and lack of mechanical coherency of this upper boundary layer [Hoffman & Ranalli, 1988], renders modern style plate tectonics ineffective [Vlaar, 1985; 1986]. v) Continents stabilized on top of strong chemical zonation in harzburgitic root and the generation of radiogenic heat in the continental crust blankets the surface cooling [Vlaar, 1985]. vi) After formation of stable basalt-harzburgite layering, recycling of basaltic material can occur through its denser phases garnet-granulite and eclogite. The recycling of eclogite allows for new generation of basaltic magma.

In the following section we will consider the consequences of these constraints on the evolution of the lithosphere and upper mantle in a hotter Earth.

8.5 Dynamical modelling

Model description

We have employed a 2-dimensional thermochemical model of the cooling of the lithosphere and upper mantle (to 400 km depth), both in an oceanic and continental setting, schematically indicated in figure 8.3. In the continental model (figure 8.3a) a crust of 40 km thickness (consisting of a 10 km thick granitic upper crust on top of a 30 km thick more tonalitic or granulitic lower crust) overlies a thick harzburgitic root. The radioactive heat production is indicated in figure 8.3a. The value of the upper crust is based on the estimate for the heat production of a surface shield [O'Connell & Hager, 1980], corrected for the assumed three times higher productivity in the early Earth. The lower crust is assumed to have a 10× lower heat production. The oceanic lithosphere/upper mantle (figure 8.3b) comprises the layering formed through decompression melting of rising diapirs, with basalt (B) on top of depleted peridotite (harzburgite; Hz), overlying the undepleted mantle peridotite (lherzolite; Lh). The harzburgite layer has a density gradient as a consequence of the varying degree of depletion by partial melting with depth. The properties of the layering are strongly dependent on potential mantel temperature.

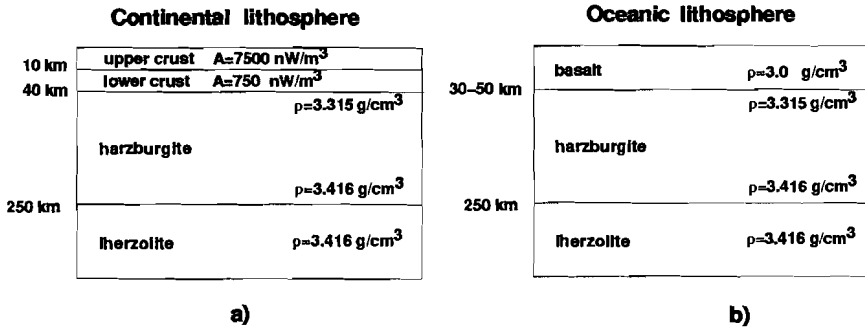The stability of these models against cooling from the top is considered. The

Figure 8.3 *Schematical overview of the compositional layering for the a) continental and b) oceanic lithosphere-upper mantle in a 'hot Earth', with potential temperatures $T_{pot} > 1600$ °C.*

free-slip upper boundary is kept at constant temperature $T = 0$ °C. At the lower boundary a constant, adiabatic temperature gradient is maintained.

To describe the rheology of the lithosphere and mantle, we have used linearized ductile creep laws, following Hoffman & Ranalli [1988]. The general form of the creep law is given by

$$\sigma = (\dot{\varepsilon}/A)^{1/n} \exp(E/nRT) \qquad (8.9)$$

where σ is differential stress (in MPa), $\dot{\varepsilon}$ the strain rate (in s^{-1}), n the power law index, E the activation energy (in Jmol^{-1}K^{-1}), R the gas constant (8.314 Jmol^{-1}), T the absolute temperature (in K). Note that σ here is specified in MPa. From this we can derive an effective viscosity $\eta = \sigma/2\dot{\varepsilon}$ (MPa · s), which can be expressed as

$$\eta = C \exp(E/nRT) \qquad (8.10)$$

where

$$C = \frac{10^6}{2} \cdot \left[\frac{\dot{\varepsilon}^{1-n}}{A} \right]^{1/n} \quad \text{(Pa · s)} \qquad (8.11)$$

The numerical values for diabase have been used to model basalt and eclogite, the values for peridotite have been used to model harzburgite and lherzolite. Tabel 8.2 gives the values for A, n and E from Hoffman & Ranalli [1988] and the value of C for $\dot{\varepsilon} = 10^{-15}$ s^{-1}. Figure 8.4 shows the effective viscosity of diabase and peridotite as a function of temperature.

The equations governing the models are the Stokes equation together with the

Table 8.2 Parameters used in the rheological description (8.11)

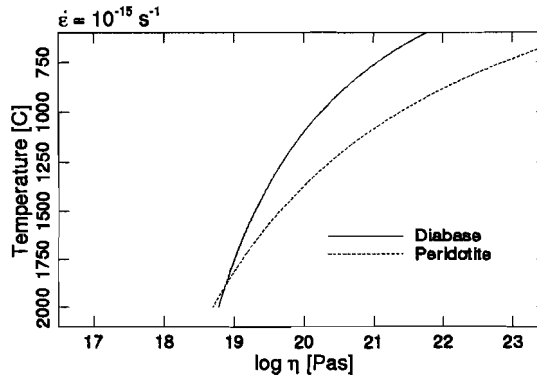| Rock	$\log A$ (MPa^{-n}s^{-1})	n	E (kJmol^{-1})	C (Pa·s)
Diabase	-2.5	3.3	268	81×10^{15}
Peridotite	4.5	3.6	535	19×10^{14}

Figure 8.4 *Effective viscosity of diabase (used to model basalt and eclogite) and peridotite (used to model harzburgite and lherzolite) as a function of temperature. Rheological parameters are defined in table 8.2.*

incompressibility constraint, the advection-diffusion equation for temperature and the advection equation for the composition, as have been derived in Chapter 2. The equations are solved numerically by finite element methods. The Stokes equation is solved in the stream function formulation (2.22), using the non-conforming element (refer chapter 3). The time-dependent heat equation (2.3) is solved using linear triangles and a predictor-corrector method. The Boussinezq approximation is used and the adiabatic temperature increase with depth has no influence on the dynamics of the model. In the numerical model this adiabatic temperature is subtracted from the absolute temperature. The absolute temperature is used in the calculation of viscosity and for output purposes. For the advection equation for the composition we have used a mixed approach. The discontinuous density jumps, as e.g. between the basalt and harzburgite (figure 8.2b) are modelled using a marker-chain method. The density gradient in the harzburgite is modelled using a field approach. In this an explicit solution of the hyperbolic equation (2.4) is required. The time step in the predictor-corrector method was taken as 50 % of the Courant time step (refer chapter 3), with an upper limit of 1 Myr.
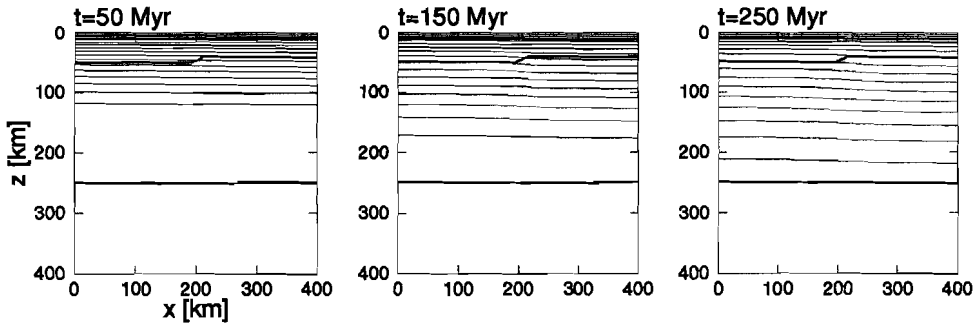
Figure 8.5 *Evolution of a cooling continental lithosphere. The compositional stratification and distribution of heat producing elements are defined in figure 8.3. Retarded by the crustal heat production, the cooling progresses slowly to deeper levels. As a consequence of the density gradient in the harzburgitic root, the lithosphere remains stably stratified.*

Results

Continental lithosphere, potential temperature 1750 °C

The evolution of the continental lithosphere is shown in figure 8.5. The lower crust is slightly thicker on one side of the model, to avoid that the model remains artificially stably stratified. The first frame shows the initial temperature profile, based on the (T,p)-path of a rising diapir. The crustal heat production balances ("blankets") only partially the heat loss through the top and the cooling progresses slowly to larger depths. As is shown in figure 8.5, the continental lithosphere is stable to at least 250 Myr. After this, the cooling progresses into the undepleted peridotitic layer. In some simulations this creates an instability in the lower parts of the model, which can recycle the lowermost parts of the (now thermally defined) continental root. However, the most important result of these simulations is that the proposed layering is intrinsically stable to cooling. This leads to a firm basis of the suggestion that the early proto-continents have been able to resist recycling on top of a chemically zoned root, and that the present thickness of the continental cratons (~ 200 km) has been maintained throughout geological history.

Oceanic lithosphere, potential temperature 1750 °C

The oceanic lithosphere, formed at T_{pot} = 1750 °C, is stably stratified in a similar fashion as the continental lithosphere, discussed above. Recycling of the basaltic crust and underlying harzburgite can only be achieved in this environment through the formation of the denser phases of gabbroic basalt: viz., garnet-granulite (GG;
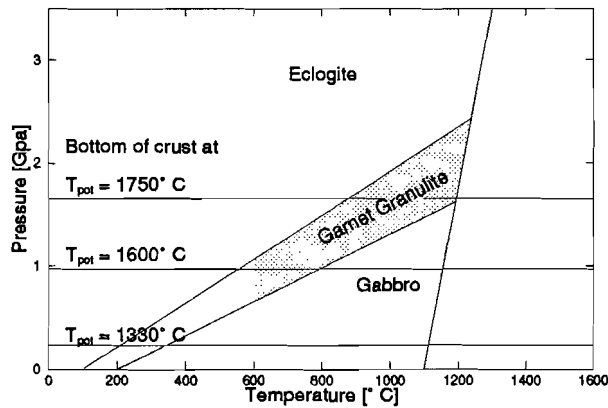
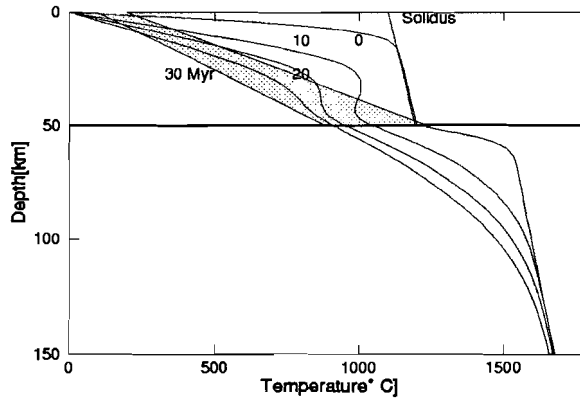**Figure 8.6** *Phase diagram for basalt [after Ringwood, 1975].*

Figure 8.7 *Evolution of the horizontally averaged temperature in the oceanic lithosphere, generated at T = 1750 °C. Convection in the basalt generates an asthenosphere and relatively cool temperatures in the lower crust.*

$\rho \sim 3.3$ g · cm^{-3}) and eclogite (E; $\rho \sim 3.6$ g · cm^{-3}). Figure 8.6 shows a phase diagram for basalt, taken from Ringwood [1975]. The horizontal lines indicate the pressures at the base of the crust, formed at $T_{pot} = 1750$, 1600 and 1330 °C, resp. At $T_{pot} = 1750$ °C, the crust is approximately 50 km thick and solid state convection can occur in the basaltic layer (assuming that the upper brittle crust has negligible influence on the dynamics). Figure 8.7 shows the evolution of the horizontally averaged temperature in the oceanic lithosphere. The initial temperature
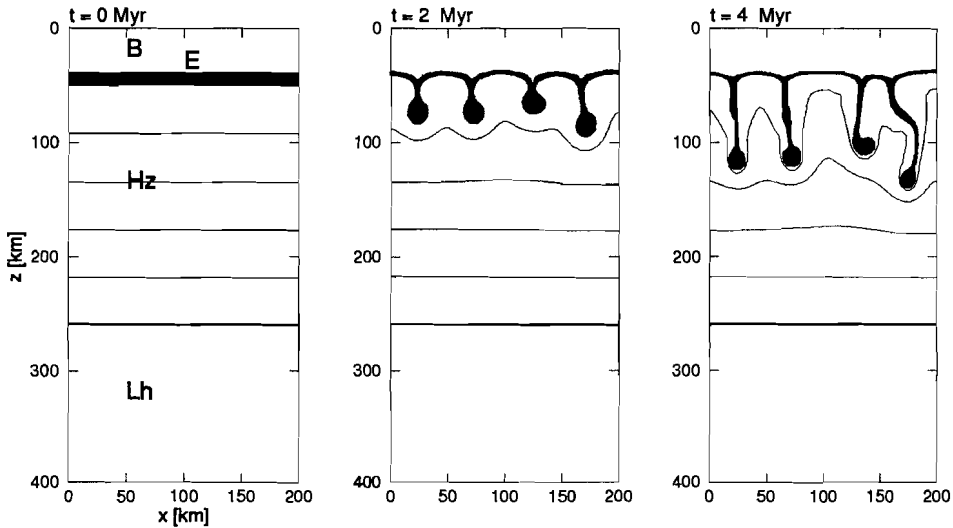
Figure 8.8 *The recycling of eclogite into the upper mantle. Original oceanic lithosphere generated at 1750 °C.*

profile underneath the basalt layer is taken from figure 8.2a. It is assumed that, after formation the basaltic crust solified very rapidly and that the basalt is at its solidus temperature, except for the thin boundary layer on top. The grey area indicates the garnet-granulite stability field, taken from figure 8.6. Cooling progresses rapidly through the efficient heat loss by the combined effects of conduction and low Rayleigh number convection. After 10 Myr, the lower part of the crust is in the garnet-granulite stability field. Garnet-granulite is nearly as dense as the underlying harzburgite. The cooler garnet-granulite may have sufficiently high density to recycle into the mantle, although the density difference with the underlying harzburgite is not very large. A more efficient way of recycling the basaltic crust is through its high density phase eclogite. This is considered in the following paragraphs.

When it is just formed, the brittle layer is thin and weak [Hoffman & Ranalli, 1988], and can probably not resist sinking into the hot ductile lower crust. Through this mechanism of crustal or 'mini'-subduction, a relatively cool ($T < 1000$ °C) and hydrated basaltic layer can be formed on top of the harzburgite. Under these conditions, the transformation from gabbro to eclogite is fast, with time scales on the order of 1 Myr [Ahrens & Schubert, 1975]. Once eclogite is formed, recycling of crustal material into the harzburgitic layer is fast. Figure 8.8 illustrates this for a layering formed at potential temperature $T_{pot} = 1750$ °C. The eclogite layer has a thickness of 10 km. Within 5 Myr most of the eclogite is recycled into the
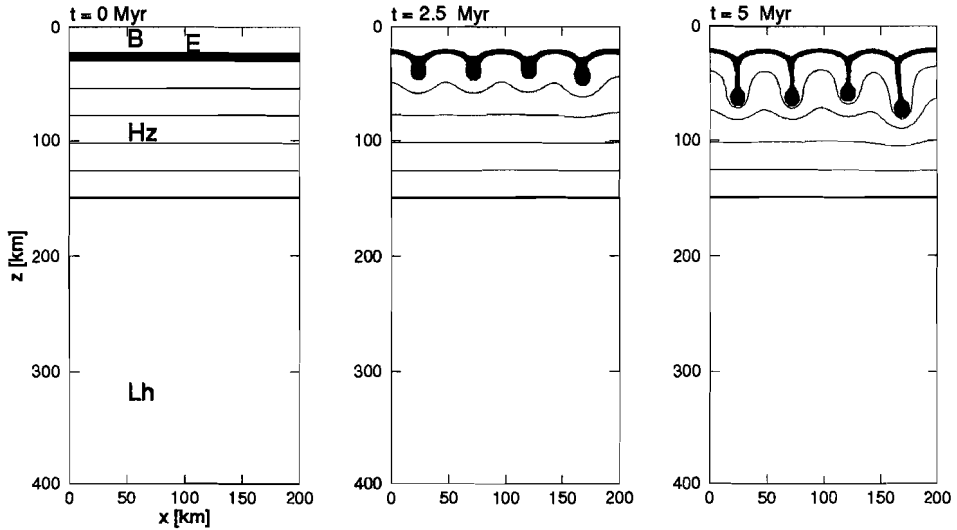
Figure 8.9 *The recycling of eclogite into the upper mantle. Original oceanic lithosphere generated at 1600 °C.*

underlying harzburgite. The harzburgite wells up passively and, if the top of the harzburgite is still hot enough, new basalt can be formed by pressure-release melting.

We propose that this mechanism of recycling of basaltic crust through mini-subduction, rapid eclogitization at the bottom of the crust, recycling of the eclogite into the upper mantle and formation of new crust by pressure-release melting, is responsible for the initial cooling of the hot Earth, after solidification of the mantle.

Oceanic lithosphere, potential temperature 1600 °C

At lower potential temperature, the proposed mechanism of cooling of the Earth will become less efficient, and eventually cease to occur. The viscosity of the lower basaltic crust and harzburgite increases, the recycling of hydrated crust will become less efficient and eclogitization is less rapid. The less efficient eclogitization of the lower crust is the main factor determining the lower speed of the mechanism. The increase in viscosity and thinning of the eclogite layer have only a minor effect, as is illustrated in figure 8.9, where the recycling of a now 5 km thick eclogitic layer is shown in a model based on a basalt-harzburgite layering formed at T_{pot} = 1600 °C. The basaltic crust has a total thickness of 29 km. Initial temperature and compositional density are given for the harzburgite/lherzolite in figures

8.2a-b. Recycling of the eclogite layer is now approximately 2x slower.

At even lower temperatures, the crust will become too thin and the brittle upper crust too strong for crustal subduction to take place and pressures at the bottom of the crust may be too low for eclogite to be formed, although it is not clear at which crustal thickness this will occur. The phase diagram for basalt (figure 8.6) indicates that eclogite cannot be formed at crustal thicknesses below ~ 25 km. However, some evidence exist for the formation of eclogite from hydrated basalt at shallower levels [Ahrens & Schubert, 1975]. The driving forces of the present day form of plate tectonics will become increasingly important and in a certain temperature range a gradual transition from the proposed mechanism and plate tectonics may occur. Tentatively, we put this transition at a potential "blocking" temperature of $T_{pot} = T_0 = 1475$ °C, at which 15 km of crust is produced.

8.6 A thermal model for the early Earth

We will now turn to the consequences of the presented dynamical model for the thermal history of the Earth. Our approach to this problem is necessarily speculative, due to the lack of detailed knowledge on the interaction between the different processes and the variability of the parameters governing the dynamical behaviour.

We assume that the cooling of the Earth's mantle is entirely caused by heat loss through the oceanic lithosphere. At present, this is estimated at 3×10^{13} W, predominantly (> 90 %) by the conductive cooling of the continuously recycling lithosphere [Sclater et al., 1980]. The consumption of latent heat at mid-oceanic ridges is only a fraction of this [Takahashi, 1990]. However, in a hotter mantle, the amount of melt generated is much larger and the dissipation of heat by magma generation may be the dominant form of cooling of the Earth [Ogawa, 1988; Takahashi, 1990]. We will use this and estimate the amount of cooling in our models by i) consumption of latent heat by pressure-release melting, ii) advection of magma to the surface, and iii) conductive cooling of the basaltic crust. Key parameter in this is the rate of recycling of basaltic crust through the eclogite phase. We will make some simplifying assumptions regarding the recycling process. Consider the 1-D lithospheric column depicted in figure 8.10a. Removal of the eclogitic layer will result in passive upwelling of the total column underneath the crust, leading to renewed pressure-release melting. The amount of latent heat consumed upon melting is equal to $\rho L \dot{V}$, where $\rho = 3000$ kg · m^{-3} is the density, $L = 6 \times 10^5$ Jkg^{-1} the latent heat of basalt melt [Fukuyama, 1985], and $\dot{V}$ the rate of eclogite recycling (in m^3 · s^{-1}). The basaltic magma is generated at a specific extrusion temperature T_{extr}. Percolation of magma to the surface will continue until the temperature in the basaltic layer is below the solidus temperature, leading to additional heat loss,
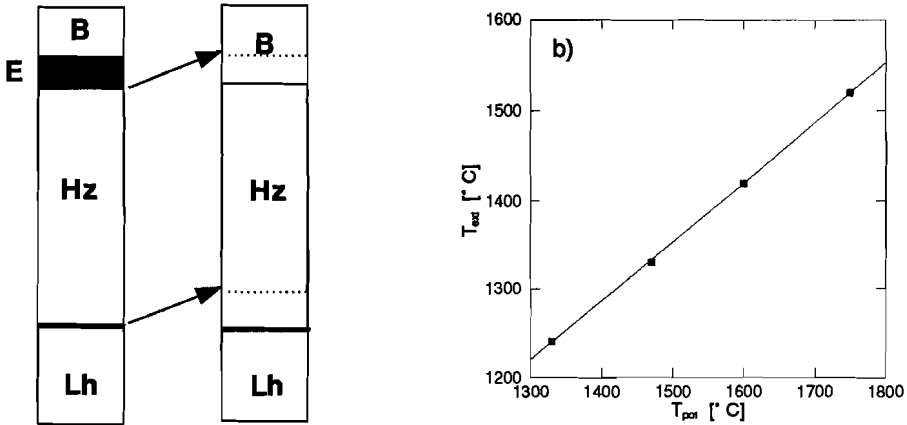
Figure 8.10 *a) Cooling of a lithospheric column through pressure-release melting. Recycling of the eclogitic layer leads to uplift of the entire column below the crust and heat loss by consumption of latent heat and magma migration. b) Dependence of extrusion temperature T_{extr} on the potential temperature T_{pot}. Points indicate the calculations made using the formalism of McKenzie [1984], corrected for the crustal pressure effect [Vlaar & Van den Berg, 1991]. The solid line indicates the first order approximation $T_{extr} = 2/3 \times (T_{pot} - 1330) + 1240$ °C.*

estimated at $\rho c_p \dot{V}(T_{extr} - T_{SB})$, where $c_p = 1.3 \times 10^3$ Jkg^{-1}K^{-1} is the specific heat and $T_{SB} = 1200$ °C the solidus temperature of basalt (assumed constant here). Furthermore, we will assume that the process of eclogite recycling is continuous and that this process leads to a continuous decrease in mantle temperature. The amount of crustal recycling is strongly dependent on potential temperature, through the processes describe above. We will parameterize this influence as a linear function $\dot{V} = a(T_{pot} - T_0)$. The parameter a depends on the rates of crustal subduction, eclogite formation and eclogite recycling. In the 1-D column the maximum combined rate is determined by the recycling rate of eclogite, which can be estimated from the results above to be ~5 km · Myr^{-1} at $T_{pot} = 1750$ °C. Assuming that 70 % of the Earth's surface is oceanic, we can convert this to an effective rate

$$\dot{V}_{\max} = (5 \text{ km} \cdot \text{Myr}^{-1}) \times (0.7 \times 5 \times 10^8 \text{ km}^2) = 1.8 \times 10^9 \text{ km}^3\text{Myr}^{-1} \quad (8.12a)$$

with corresponding

$$a_{\max} = 6.4 \times 10^6 \text{ km}^3\text{Myr}^{-1}\text{K}^{-1} \quad (8.12b)$$

The extrusion temperature T_{extr} depends on the potential temperature as well. In a first order approximation this dependence is given by (figure 8.10b):

$$T_{extr} = 2/3 \times (T_{pot} - 1330) + 1240 \,°C \tag{8.13}$$

In this model, we can only guess at the rate of cooling through conductive heat loss. The dynamic models presented above indicate only the efficiency of eclogite recycling, once it is formed. It does not provide us with information on the processes controlling melt segregation, melt migration and the temperature distribution in the lithospheric column as has been described above. We estimate that, in comparison to the heat loss by latent heat consumption and melt migration, conductive cooling has only a minor contribution to the total heat loss in the hotter Earth. For practical purposes, we assume that the conductive heat loss has not varied throughout geological time, and fix it at the present day value of

$$4\pi q R_m^2 = 3 \times 10^{13} \,W \tag{8.14a}$$

In comparison, at the highest estimated recycling rate $\dot{V}_{max}$, the cooling through latent heat consumption contributes

$$\rho L \dot{V}_{max} = 2 \times 10^{14} \,W \tag{8.14b}$$

and the melt migration contributes ($T_{pot} = 1750 \,°C$)

$$\rho c_p (T_{extr} - T_{SB}) \dot{V}_{max} = 1.5 \times 10^{14} \,W \tag{8.14c}$$

We can now model the thermal evolution of the Earth using an extension to (8.1), given

$$\frac{4\pi}{3} \rho c_p (R_m^3 - R_c^3) \frac{dT}{dt} = -4\pi q R_m^2 + \frac{4\pi}{3} Q(R_m^3 - R_c^3)$$

$$- \rho c_p \dot{V} (T_{extr} - T_{SB}) - \rho L \dot{V} \tag{8.15}$$

The temperature T is the mean mantle temperature, which is assumed to be the temperature at 1500 km depth. The relation with the potential temperature is given $T = T_{pot} + 750$, assuming a constant adiabatic gradient of $0.5 \,K \cdot km^{-1}$. Heat production Q is modelled using Sleep's [1979] estimates of the absolute abundance of K, U and Th from the amount of ^{40}Ar. Figure 8.11 shows the evolution of the model, initially with $T_{pot} = 1750 \,°C$, for initial crustal recycling rates $\frac{1}{2} \dot{V}_{max}$, $\frac{1}{5} \dot{V}_{max}$, and $\frac{1}{10} \dot{V}_{max}$, resp. Shown are from left to right the potential temperature T_{pot} (in °C), latent heat consumption and heat advected by migrating melt (both in 10^{12} W). At potential temperature $T_0 = 1475 \,°C$, it is assumed that the mechanism becomes inefficient and heat loss is governed by conductive heat loss (8.14a) only. At the highest recycling rate shown the Earth cools by more than 200 K within 200 Myr. At $t = 0.5$ Gyr, the blocking temperature T_0 is reached. At the lower recycling rates the cooling progresses slower, but still a large drop in temperature is observed in 1 Gyr. These results should be considered with proper caution as they
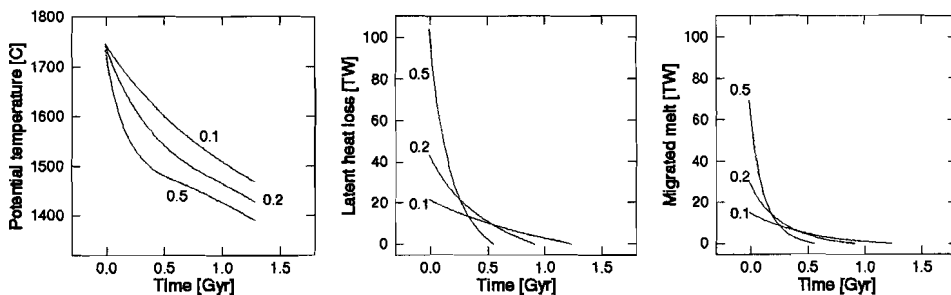
Figure 8.11 *Influence of the latent heat loss and melt migration on the internal temperature of the Earth (8.15). Numbers indicate the crustal recycling rate at the arbitrary starting point, put at t = 0, relative to the proposed maximum $\dot{V}_{max}$ (8.12a).*

are based on a rather speculative quantification and error margins are large. Most likely the conductive heat loss has been larger than modelled here, leading to a more efficient cooling. The estimates for the radiogenic heat production of Sleep [1979] are rather low compared to others. Increasing the heat production by a factor of two leads to much longer cooling times. However, it is not fully unreasonable to assume that, when the proposed mechanism has been active at some time in the Earth's history, it has efficiently cooled the mantle by several hunderds of degrees in, say, a 500 Myr period, leading to a moderate mantle temperature, maybe some 100-200 K higher than the present day situation.

Geological constraints on the thermal development of the upper mantle are given by the extrusion temperatures of volcanic rocks. Komatiites indicate the highest mantle temperatures, approx. $T_{pot} = 1650 - 1750°C$ at 3.5 Gyr B.P., and $T_{pot} = 1500 - 1600°C$ at 2.7 Gyr B.P. These are based on the estimates of the extrusion temperatures of the komatiites [e.g., Arndt & Nesbit, 1982] and the *ad hoc* estimates of the amount of latent heat, necessary to generate komatiitic melt at depth, ranging from 0 °C [McKenzie, 1984; Takahashi, 1990] to 100 °C [Sleep, 1979]. Other Archaean volcanic rocks, like ophiolites and greenstones, have extrusion temperatures that are distinctly lower. Abbott et al., [1993] determine for these rocks, that the mean extrusion temperature has decreased by approximately 150 K since the early Archaean (3.5 Gyr B.P.). Assuming that they are generated by pressure-release melting, a decrease in potential mantle temperature of 250 K can be inferred. It is not unreasonable to assume that the mean Archaean mantle temperature has been some 200-300 K higher than present day's. Even higher mantle temperatures imply conditions that are more favourable for eclogite formation and recycling as a consequence of the thicker basaltic layer, lack of mechanical coherency and larger mobility of the crust and upper mantle. The remelting of

eclogite upon recycling at moderate depths (50-100 km; see figure 8.7) may well have been important in the formation of tonalitic proto-continents in the very early Archaean [Condie, 1984]. The middle to late Archaean could have been characterized by some form of 'flake tectonics' [Hofmann & Ranalli, 1988], at the transition between the hot Earth dynamics and the present day plate tectonics. At these moderately higher upper mantle temperatures, the basaltic crust is still thick enough to resist lithospheric subduction, but is probably to thin to allow for efficient eclogite formation and recycling.

8.7 Discussion

In the above, we have illustrated, quantitatively, some dynamical effects that can occur in a hotter mantle. Using the results of the dynamical modelling, we can envisage a strong episodic behaviour of the upper boundary layer, with periods of relative stabilization and conductive cooling followed by strong magmatic activity as a consequence of the thermal and compositional instability of the lower basaltic crust.

The interaction between the different mechanisms has yet to be explored. Presently, this is hampered by technical difficulties: a high resolution both in time and space is necessary to resolve the complex interaction. A large problem is presented by the different time scales at which relevant processes take place, as for example the migration of magma compared to the deformation of the solid phase. Studying one of these processes necessitates simplifying assumptions of the other one, although the two processes are dependent on each other.

Comments on rheological parameters

The rate of recycling is strongly dependent on the rheology of the basalt/eclogite and harzburgite. Some field evidence exists that eclogite has a lower viscosity than basalt [Austrheim, 1991]. We have taken this into account in some model calculations but no large difference was observed: as harzburgite is more viscous than both basalt and eclogite at the ambient temperatures (figure 8.4), it controls the speed of the sinking eclogite. In some models we have included pressure-dependence by extending the Arrhenius term in (8.9): $\sigma \sim \exp[(E + pV)/nRT)$, where p is the pressure and V the activation volume, which was assumed constant, $V = 10$ cm^{3}mol^{-1}. The pressure-dependence is relatively unimportant in the upper 100 km and, consequently, little influence on the dynamics could be observed. The linearization of the power law creep law (8.9) will not be correct for strain rates much higher or lower than $\dot{\varepsilon} = 10^{-15}$ s^{-1}. In the highest temperature models the recycling of eclog-

ite took place at strain rates significantly higher than this. The non-Newtonian effects will help drain the eclogitic layer even faster.

Venus

It is interesting to note a similarity of the presented models, with one that has recently been proposed for Venus by Parmentier & Hess [1992]. These authors studied the influence of the chemical stability of the lithosphere on the dynamics of Venus. They found that by surface cooling the Venusian lithosphere would become periodically unstable (with a characteristic period of 300-500 Myr) and resurfacing of Venus would occur. This model has been used to explain the relatively young crust (with ages of at most 500 Myr), as has been inferred from the record of impact cratering [Solomon, 1993]. The time scales found by Parmentier & Hess [1992] are much longer than we find in present paper. The efficient recycling and eclogitization of the hydrated upper crust as is proposed for the 'hot Earth' is not likely to work on Venus, as a consequence of the absence of water. Delamination of the upper and lower basaltic crust and consequent recycling of the cold and brittle upper crust is much less efficient. Moreover, the reaction time of the dry gabbro-eclogite transition is very long: probably on the order of 100 Myr [Ahrens & Schubert, 1975].

Coupling between upper and lower mantle

In the model presented above, we assumed that the cooling of the Earth is completely governed by the dynamics of the upper boundary layer and that any sinking material is replaced by passively upwelling mantle material. This is probably too simple a viewpoint, considering the mounting evidence for the strong influence of the transition zone on mantle dynamics. In recent modelling it has been shown that the thermodynamical [e.g., Christensen & Yuen, 1984; Machetel & Yuen, 1989; Steinbach & Yuen, 1992], compositional [Kellogg, 1991; Hansen et al., 1993] and rheological [Van Keken et al., 1992] properties of the transition zone will retard the exchange of material between upper and lower mantle. One can think of a scenario in which the upper mantle is efficiently cooled on top of a temporarily insulated lower mantle, until the temperature difference between upper and lower mantle is suffiently large to overcome the resistance of the transition zone and large parts of the cold upper mantle are replaced by hot lower mantle. This mechanism may have occured periodically through geologic time. The occurence in the mid-Cretaceous of a sudden increase in plate velocities and crustal formation, combined with the eruption of massive flood basalts [Larson, 1991], may be understood in this way, and the abundant occurrence of komatiites in the Archaean may well have been a consequence of the episodic mixing between upper and lower mantle.

8.8 Conclusions

We have investigated some aspects of the dynamical behaviour of a proposed mechanism to cool the Earth in the Archaean. This mechanism involves thermal and compositional advection in a strongly stratified oceanic lithosphere at high average mantle temperatures. The basaltic crust is recycled into the mantle through its high pressure phase eclogite, leading to renewed pressure-release melting and basaltic crust formation. Consumption of latent heat and the advective cooling through magma migration is sufficient to cool the mantle in the (early) Archaean by several hundreds of degrees.

Acknowledgements

Appendix A

Penalty function method

The finite element package Sepran is used to solve the equation of motion (2.2) in the penalty function formulation. Chapter 3 gives an outline of the method. In this appendix some technical details are discussed.

In the matrix assembly process the velocity components in the barycenter and the pressure derivatives are eliminated from the Crouzeix-Raviart element (figure 3.1) resulting in the modified Crouzeix-Raviart ($P_2^+ - P_1$) element [Cuvelier et al., 1986] with the velocity components given in the six boundary nodal points and the pressure in the barycenter (figure A.1a). A profile method is used to store the matrix [Cuvelier et al., 1986] and the nodal points are renumbered using an algorithm by Sloan [1986] to reduce the profile of the matrix. The resulting system of equations is solved by Gaussian elimination.

The temperature equation is solved on a mesh with the same nodal point distribution as is used in solving the equation of motion. Each Crouzeix-Raviart element
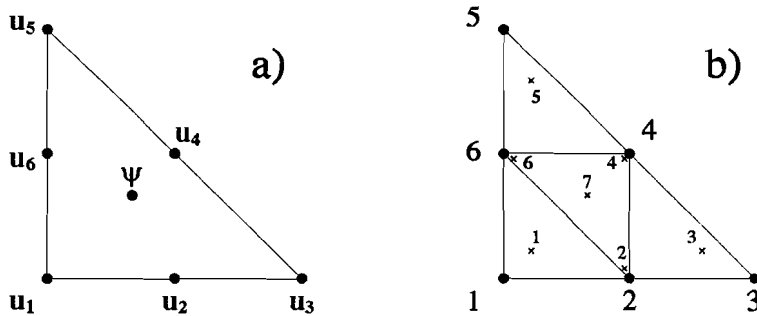

Figure A.1 *a) The modified Crouzeix-Raviart element b) Subdivision of the Crouzeix-Raviart element into four elements with three nodal points each. These elements are used in the solution of the temperature equation. Solid dots are the nodal points in which the temperature and velocity components are known. Crosses indicate the positions of the Gaussian points used in the penalty function method.*

is subdivided into four linear triangles (figure A.1a). After solving the Stokes equation, the nodal point values of velocity can be used without interpolation in constructing the stiffness matrix (3.3b) of the discretized temperature equation.

The integral expressions in the matrix and vector coefficients are approximated by a seven-point Gauss quadrature rule [Strang & Fix, 1973],

$$\int_e f(\mathbf{x}) \, de \approx \sum_{k=1}^{7} w_k f(\mathbf{x}_k) \tag{A.1}$$

where the weights w_k and the barycentric coordinates λ of the Gaussian points are given in table A.1a. The expressions for viscosity η and buoyancy forces have to be evaluated in the Gaussian points. This can be done by calculating the quantities in the nodal points and interpolating these onto the integration points using the quadratic shape functions, but it is found that the accuracy of the method is considerably increased by first calculating the dependent variables (p, Γ, T, $\dot{\varepsilon}$) in the Gaussian points before evaluating the viscosity and buoyancy forces. The strain rate $\dot{\varepsilon}$ can be expressed as a function of the nodal point values of velocity ($\mathbf{u}_i$) and the values of the derivatives of the quadratic shape functions in the Gaussian points (ϕ_i). Components of the strain rate tensor are given by expressions of the form

a. 7 point Gauss rule

point	λ_1	λ_2	λ_3	w
1	a_1	a_2	a_2	g_1
2	b_1	b_1	b_2	g_2
3	a_2	a_1	a_2	g_1
4	b_2	b_1	b_1	g_2
5	a_2	a_2	a_1	g_1
6	b_1	b_2	b_1	g_2
7	1/3	1/3	1/3	g_3

b. Interpolation coefficients for (A.3)

k	r_1^k	r_2^k	r_3^k	r_4^k	r_5^k	r_6^k
1	c_2	c_1	0	0	0	c_1
2	0	d_1	0	d_2	0	d_2
3	0	c_1	c_2	c_1	0	0
4	0	d_2	0	d_1	0	d_2
5	0	0	0	c_1	c_2	c_1
6	0	d_2	0	d_2	0	d_1
7	0	1/3	0	1/3	0	1/3

Table A.1
a. Barycentric coordinates λ of integration points and weights w for 7 point Gaussian quadrature rule [Strang & Fix, 1973]. $a_1 = 0.79743$, $a_2 = 0.10129$, $b_1 = 0.47014$, $b_2 = 0.05971$, $g_1 = 0.06296$, $g_2 = 0.06619$ and $g_3 = 0.11250$.
b. Interpolation coefficients for equation (A.3). $c_1 = 2a_2 = 0.2026$, $c_2 = 2a_1 - 1 = 0.5946$, $d_1 = 4b_1 - 1 = 0.8806$ and $d_2 = 1 - 2b_1 = 0.05971$.

$$\dot{\varepsilon}_{12}(\mathbf{x}_k) = \frac{\partial u}{\partial y}(\mathbf{x}_k) + \frac{\partial v}{\partial x}(\mathbf{x}_k) = \sum_{i=1}^{6}\left[u_i \frac{\partial \phi_i}{\partial y}(\mathbf{x}_k) + v_i \frac{\partial \phi_i}{\partial x}(\mathbf{x}_k) \right] \qquad \text{(A.2)}$$

Linear shapefunctions, defined on the triangle using the points $\mathbf{x}_1$, $\mathbf{x}_3$ and $\mathbf{x}_5$, are given by

$$\lambda_i = a_i + b_i x_{2i-1} + c_i y_{2i-1} \quad , \quad i = 1,3 \qquad \text{(A.3)}$$

where the coefficients a_i, b_i and c_i are given by

i	$b_i \cdot \Delta$	$c_i \cdot \Delta$	a_i
1	$y_2 - y_3$	$x_3 - x_2$	$-b_1 x_3 - c_1 y_3$
2	$y_3 - y_1$	$x_1 - x_3$	$-b_2 x_3 - c_2 y_3$
3	$y_1 - y_2$	$x_2 - x_1$	$-b_3 x_1 - c_3 y_1$

[Cuvelier et al., 1986]. Here $\Delta = -c_3 b_1 + b_3 c_1$. The expressions for the quadratic shape functions defined on the triangle can be defined using (A.3) as

$$\phi_1 = \lambda_1(2\lambda_1 - 1) \quad , \quad \phi_3 = \lambda_2(2\lambda_2 - 1) \quad , \quad \phi_5 = \lambda_3(2\lambda_3 - 1) \qquad \text{(A.4a)}$$

and

$$\phi_2 = 4\lambda_1\lambda_2 \quad , \quad \phi_4 = 4\lambda_2\lambda_3 \quad , \quad \phi_6 = 4\lambda_3\lambda_1 \qquad \text{(A.4b)}$$

[Cuvelier et al., 1986]. The derivatives of these shape functions, that occur in (A.2), can be calculated analytically. The temperature field is interpolated from the nodal points in a consistent way, using the shape functions of the linear triangles (figure A1.b). The temperature in each Gaussian point can be expressed as a weighted sum of the nodal point values T_i

$$T(\mathbf{x}_k) = \sum_{i=1}^{6} r_i^k T_i \qquad \text{(A.5)}$$

The weights r_i^k can be derived from the barycentric coordinates of the Gaussian points and are given in table A.1b.

Appendix B

Stream function methods

Two methods have been developed to solve the equation of motion (2.2) in the stream function formulation. This appendix adds some technical details to the general discussion of the methods in chapter 3.

Non-conforming element

Consider the rectangular finite element depicted in figure B.1 Coordinates of the nodal points are given by $x_1 = (0, 0)$, $x_2 = (a, 0)$, $x_3 = (a, b)$ and $x_4 = (0, b)$.
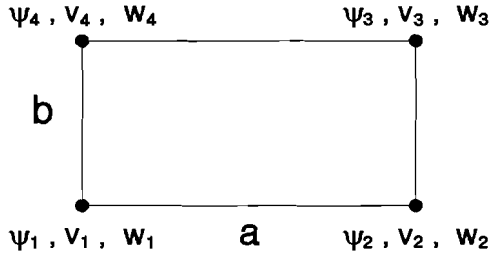

ψ_4, V_4, W_4 ψ_3, V_3, W_3

b

ψ_1, V_1, W_1 a ψ_2, V_2, W_2

Figure B.1 *Rectangular non-conforming element.*

In each nodal point the stream function and its derivates to x and y are the components of the displacement vector (3.27)

$$\mathbf{a}_i = \left[\; \bar{\psi}_i \; , \quad (\frac{\partial \bar{\psi}}{\partial y})_i \; , \quad -(\frac{\partial \bar{\psi}}{\partial x})_i \; \right]^{\mathrm{T}} \tag{B.1}$$

The stream function in the element is approximated by (3.25)

$$\bar{\psi} = \sum_{i=1}^{4} \mathbf{N}_i \mathbf{a}_i \tag{B.2}$$

where the shape functions contained in $\mathbf{N}_i$ are derived from the polynomial expansion

$$\bar{\psi} = \alpha_1 + \alpha_2 x + \alpha_3 y + \alpha_4 x^2 + \alpha_5 xy + \alpha_6 y^2 + \alpha_7 x^3$$

$$+ \alpha_8 x^2 y + \alpha_9 x y^2 + \alpha_{10} y^3 + \alpha_{11} x^3 y + \alpha_{12} x y^3 \qquad \text{(B.3)}$$

Explicit expressions for N_i can be derived from Cheung & Yeo [1979]. These are written

$$N_1 = [\ 1 - \eta\xi - (3 - 2\eta)\eta^2(1 - \xi) - (1 - \eta)(3 - 2\xi)\xi^2 \ ,$$

$$\eta(1 - \eta)^2(1 - \xi)b \ , \ -(1 - \eta)\xi(1 - \xi)^2 a \ ] \qquad \text{(B.4a)}$$

$$N_2 = [\ (1 - \eta)(3 - 2\xi)\xi^2 + \eta(1 - \eta)(1 - 2\eta)\xi \ ,$$

$$\eta(1 - \eta)^2\xi b \ , \ (1 - \eta)(1 - \xi)\xi^2 a \ ] \qquad \text{(B.4b)}$$

$$N_3 = [\ (3 - 2\eta)\eta^2\xi - \eta\xi(1 - \xi)(1 - 2\xi) \ ,$$

$$-(1 - \eta)\eta^2\xi b \ , \ \xi^2(1 - \xi)\eta a \ ] \qquad \text{(B.4c)}$$

$$N_4 = [\ (3 - 2\eta)\eta^2(1 - \xi) + \eta\xi(1 - \xi)(1 - 2\xi) \ ,$$

$$-(1 - \eta)\eta^2(1 - \xi)b \ , \ -\xi\eta(1 - \xi)^2 a \ ] \qquad \text{(B.4d)}$$

where $\xi = x/a$ and $\eta = y/b$.

The integral expressions occurring in the coefficients of the stiffness matrix (3.27) and load vector (3.28) are calculated using a 3×3 Gaussian quadrature rule. The resulting system of equations is stored by a profile method (appendix A) and solved by Gaussian elimination. The velocity within the element is approximated by

$$v(x, y) = \frac{\partial \bar{\psi}}{\partial y}(x, y) = \sum_{j=1}^{4} \mathbf{a}_j \cdot \frac{\partial N_j(x, y)}{\partial y} \qquad \text{(B.5a)}$$

$$w(x, y) = -\frac{\partial \bar{\psi}}{\partial x}(x, y) = -\sum_{j=1}^{4} \mathbf{a}_j \cdot \frac{\partial N_j(x, y)}{\partial x} \qquad \text{(B.5b)}$$

where the derivatives of the shape functions are evaluated analytically. In case of non-Newtonian flows, the second invariant of the strain rate tensor is evaluated in a similar way, prior to calculating the effective viscosity (refer appendix A)

The temperature equation is solved on a mesh consisting of linear triangles (refer chapter 3) with the same nodal point distribution. The nodal point values of temperature are interpolated onto the Gaussian points using bilinear shape functions. The horizontal temperature derivative in the Gaussian points - that is used in the calculation of the load vector - is then written

$$\frac{\partial T}{\partial x}(\mathbf{x}_{gauss}) \;=\; \frac{\eta_{gauss}}{a}(T_1 - T_2 + T_3 - T_4) + \frac{1}{a}(T_2 - T_1) \tag{B.6}$$

where T_i is the temperature in nodal point i.

Spline method

Figure B.2 shows the shapes of the 1-D cubic B-spline Φ_0 and its derivatives, for a spline centered at $x = 0$ and element size $\Delta x = 1$. The spline is non-zero on four elements. In the outer nodal points the spline and its first and second derivatives are zero. If the elements are of the same size, then the spline and its derivatives can be written as the functions y_i that are shown for each element i in table B.1; ξ is the local coordinate in the element.

Table B.1   **Figure B.2**

1-D cubic B-spline and derivatives.

i	y_i	y_i'	y_i''
1	ξ^3	$3\xi^2$	6ξ
2	$-3\xi^3 + 3\xi^2 + 3\xi + 1$	$-9\xi^2 + 6\xi + 3$	$-18\xi + 6$
3	$3\xi^3 - 6\xi^2 + 4$	$9\xi^2 - 12\xi$	$18\xi - 12$
4	$(1-\xi)^3$	$-3(1-\xi)^2$	$6(1-\xi)$
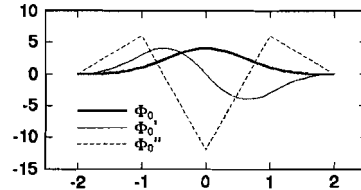
Similar functions can be written for a specific type of non-equidistant grids [Kopitzke, 1977]. The two-dimensional equivalent of Φ_j is the bicubic spline $\Psi_j = \Phi_{j,x}\Phi_{j,y}$, which has a characteristic bell shape. In each element 16 splines have a non-zero contribution (figure B.3a) and this makes the construction of the matrix coefficients (3.33) an expensive task. The calculation is obscured by the fact that the splines with contributions at the boundaries have to be modified. Consider the region $\Omega = [0, \lambda] \times [0, 1]$, that is discretized using $N_x \times N_y$ equidistant elements, each with dimensions $\Delta x \times \Delta y$. The approximate solution to the boundary value problem is constructed by (3.31), where the splines at the edges of the mesh have been adapted to satisfy to boundary conditions (figures B.3b-c). Consider figure B.3b. The free-slip boundary condition $\bar{\psi} = \bar{\psi}_{xx} = 0$ is satisfied by subtracting the virtual spline centered at the first grid point outside the domain Ω (at $x = -\Delta x$) from the spline centered at $x = \Delta x$ and neglecting the spline centered at the boundary ($x = 0$). The free-slip boundary condition in a corner element can be obtained by using the 12 virtual splines displayed in figure B.3c. Only the spline
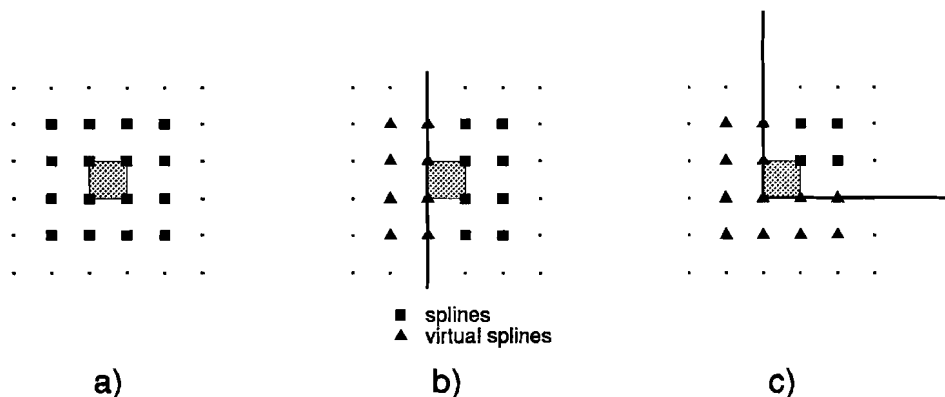
Figure B.3 *Geometry of bicubic splines. Small dots indicate the grid. a) In one element (grey area) 16 splines (solid squares) have non-zero contribution. In elements at the edge (b) and in the corner (c) virtual splines (solid triangles) are used to satisfy the boundary conditions.*

coefficients that belong to the splines centered at the $(N_x - 1) \times (N_y - 1)$ grid points within the geometry Ω are unknown. In general the aspect ratio is $\lambda \geq 1$ and $N_x \geq N_y$. In this case the nodal points are numbered in a standard fashion: point 1 is at $(0,0)$, point 2 at $(0, \Delta y)$, point N_y at $(0, 1)$, point $N_y + 1$ at $(\Delta x, 0)$ etc.

The matrix is stored as a band matrix and solved using standard Linpack band solvers. The matrix coefficients A_{ij} contain products of the derivatives bicubic splines Ψ_i and Ψ_j. In 1-D the product between two B-splines Φ_i and Φ_j is only non-zero if the distance between the nodal points i and j is ≤ 3. Hence the the bandwidth of the resulting matrix is 3. In 2-D the maximum spacing, and hence the bandwith, is $3 \times N + 3$, where $N = N_y$ in the nodal point numbering described above.

The calculation of the matrix coefficients is optimized by using the localization of the splines and pre-calculating the products of the derivatives occurring in (3.33) in the Gaussian points. As has been shown by Christensen [cf. Blankenbach et al., 1989], a more efficient code can be obtained by calculating the integral expressions analytically, which is, to some extent, possible for generalized Newtonian fluids as well [Kopitzke, 1977].

References

Abbot, D., Burgess, L., Longhi, J., and Smith, W.H.F., 1993. An empirical thermal history of the Earth's upper mantle. Submitted to J.Geoph.Res.

Ahrens, T.J., and Schubert, G., 1975. Gabbro-eclogite reaction rate and its geophysical significance. Rev.Geoph.Space Phys., 13: 383-400.

Anderson, D.L., 1989. Theory of the Earth, Blackwell Scientific Publishers, Boston, 366 pp.

Arndt, N.T., 1983. Role of a thin, komatiite-rich oceanic crust in the Archean plate-tectonic process. Geology, 11: 372-375.

Arndt, N.T., and Nisbet, E.G. (eds), 1982. Komatiites. Allen & Unwin, London.

Austrheim, H., 1991. Eclogite formation and dynamics of crustal roots under continental collision zones. Terra Nova, 3: 492-499.

Batchelor, G.K., 1967. An introduction to fluid dynamics. Cambridge University Press.

Batiza, R., Karsten, J., Niu, Y., Boger, W., Sherman, S., Cushing, J., Duncan, R., Graham, D., Gallahan, W., Sinton, C., Paslick, C., and Janney, P., 1992. Temporal variation of East Pacific Rise lavas to 0.5 Ma at 9.30' N, 10.30' N and 11.20' N, Eos Trans.AGU, 73: 525.

Berner, H., Ramberg, H., and Stephansson, O., 1972. Diapirism in theory and experiment. Tectonophysics, 15: 197-218.

Bickle, M.J., 1978. Heat loss from the Earth: constraints on Archean tectonics from the relation between geothermal gradients and the rate of plate production. Earth Plan.Sci.Lett., 40: 301-315.

Bickle, M., 1986. Implication of melting for stabilization of the lithosphere and heat loss in the Archaean. Earth Plan.Sci.Lett., 80: 314-324.

Blankenbach, B., Busse, F., Christensen, U., Cserepes, L., Gunkel, D., Hansen, U., Harder, H., Jarvis, G., Koch, M., Marquart, G., Moore, D., Olson, P., Schmeling, H., and Schnaubelt, T., 1989. A benchmark comparison for mantle convection codes. Geoph.J.Int., 98: 23-38.

Biot, M.A., and Odé, H., 1965. Theory of gravity instability with variable overburden and compaction. Geophysics, 30: 213-227.

Bird, R.B., Stewart, W.E., Lightfoot, E.N., 1960. Transport phenomena. Wiley, New York.

Bobineau, J.P., 1992. Simulations numériques de phénomènes tectoniques. PhD thesis, Ecole Centrale de Paris.

Brown, J.M., 1986. Interpretation of the D" zone at the base of the mantle: dependence on assumed values of thermal conductivity, Geophys. Res. Lett., 13: 1509-1512.

Buck, W.R., and Parmentier, E.M., 1986. Convection beneath young oceanic lithosphere: implications for thermal structure and gravity. J.Geophys.Res., 91: 1961-1974.

Busse, F.H., 1989. Fundamentals of thermal convection. In: "Mantle convection, plate tectonics and global dynamics", W.R. Peltier (ed), Gordon & Breach, New York, 23-95.

Byerlee, J.D., 1978. Friction of rocks. Pure and Appl.Geoph., 116: 615-626.

Campbell, I.H., and Griffiths, R.W., 1992. The changing nature of mantle hotspots through time: implications for the chemical evolution of the mantle. J.Geol., 92: 497-523.

Carter, N.L., and Hansen, F.D., 1983. Creep of rocksalt. Tectonophysics, 92: 275-333.

Carter, N.L., Kronenberg, A.K., Ross, J.V. and Wiltschko, D.V., 1990. Control of fluids on deformation of rocks. In: "Deformation mechanisms, rheology and tectonics", R.J. Knipe and E.H. Rutter (editors). Geological Society special publication, 54: 1-13.

Carter, N.L., Handin, J., Russeld, J.E. and Horseman, S.T., 1992. Rheology of rocksalt. In: J.M. Christie Festschrift, Journal of Structural Geology, in press.

Chandrasekhar, S., 1961. Hydrodynamic and hydromagnetic stability, Dover Publications, New York.

Cheung, Y.K., and Yeo, M.P., 1979. A practical introduction to finite element analysis. Pitman.

Chopelas, A. and Boehler, R., 1989. Thermal expansion measurements at very high pressure, systematics and a case for a chemically homogeneous mantle, Geophys. Res. Lett., 16: 1347-1350.

Christie, D.M., Duncan, R.A., McBirney, A.R., Richards, M.A., White, W.M., Harpp, K.S., and Fox, C.G., 1992. Drowned islands downstream from the Galapagos hotspot imply extended speciation times, Nature, 355: 246-248.

Christensen, U., 1984a. Convection with pressure- and temperature-dependent non-Newtonian rheology. Geoph.J. R.A.S., 77: 343-384.

Christensen, U.R., 1984b. Instability of a hot boundary layer and initiation of thermo-chemical plumes, Annal. Geophys., 2: 311-320.

Christensen, U.R., 1984c. Heat transport by variable viscosity convection and implications for the Earth's thermal evolution. Phys.Earth Plan.Int., 35: 264-282.

Christensen, U.R., 1985. Thermal evolution models for the Earth. J.Geoph.Res., 90: 2995-3008.

Christensen, U., 1991. Segregation of subducted oceanic crust - a numerical model. Ann. Geoph., suppl. to 9:C68.

Christensen, U.R., 1992. An Eulerian technique for thermomechanical modelling of lithospheric extension. J.Geoph.Res., 97: 2015-2036.

Christensen, U., and Yuen, D.A., 1984. The interaction of a subducting lithospheric slab with a chemical or phase boundary. J.Geoph.Res., 89: 4389-4402.

Christensen, U.R. and Yuen, D.A., 1989. Time-dependent convection with non-Newtonian viscosity, J. Geophys. Res., 94: 814-820, 1989.

Clark, S.P., 1966. Thermal conductivity. In: "Handbook of physical constants", Clark, S.P. (editor). Geol.Soc.Am.Mem., 97: 459-482.

Cloetingh, S.A.P.L., Wortel, M.J.R., and Vlaar, N.J., 1982. Evolution of passive continental margins and initiation of subducting zones, Nature, 297: 139-142.

Cobbold, P.R., and Szatmari, P., 1991. Radial gravitational gliding on passive margins. Tectonophysics, 188: 249-289.

Condie, K.C., 1984. Archean geotherms and supra crustal assemblages. Tectonophysics, 105: 29-41.

Cuvelier, C., Segal, A., and Van Steenhoven, A.A., 1986. Finite Element methods and Navier-Stokes equations. D. Reidel, Dordrecht.

Daudré, B., Poliakov, A., Van Balen, R., Cloetingh, S., and Stephenson, R., 1992. Salt diapirism and mechanics of sedimentary basins. Ann.Geoph., suppl. to 10: C91.

Davies, G.F., 1979. Thickness and thermal history of continental crust and root zones. Earth Plan.Sci.Lett., 44: 231-238.

Detrick, R. and Crough, S.T., 1978. Island subsidence, hot spots, and lithosphere thinning, J. Geophys. Res., 83: 1236-1244.

Detrick, R.S., Von Herzen, R.P., Crough, S.T., Epp, D., and Fehn, U., 1981. Heat flow on the Hawaiian Swell and lithosphere reheating, Nature, 292: 142-143.

Dongara, J.J., 1986. Performance of various computers using standard linear equations software in a Fortran environment. Technical Memorandum No. 23, Argonne National Laboratory, 9700, South Cass Avenue, Argonne, IL 60349, USA.

Fukuyama, H., 1985. The heat of fusion of basaltic magma, Earth Plan.Sci.Lett., 73: 407-414.

Gevantman, L.H. (editor), 1981. Physical properties data for rocksalt. U.S. Dept. of Commerce, Nat.Bur. of Standards Mon. 167.

Gente, P., Ceuleneer, G., Durand, C., Pockalny, R., Deplus, C., and Maia, M., 1992. Propagation rate of segments along the Mid-Atlantic Ridge between 20 and 24 deg. (SEADME I Cruise). Eos Trans.AGU, 73: 569.

Goetze, C. and Kohlstedt, D.L., 1973. Laboratory study of dislocation climb and diffusion in olivine,

J. Geophys. Res., 78: 5961-5971.

Gurnis, M., 1986. The effects of chemical density differences on convective mixing in the earth's mantle. J.Geoph.Res., 91: 6375-6395.

Hager, B.H., 1984. Subducted slabs and the geoid: constraints on mantle rheology and flow, J.Geoph.Res., 89: 6003-6016.

Hager, B.H. and Richards, M.A., 1989. Long-wavelength variations in Earth's geoid: physical models and dynamical implications, Phys. Trans. R. Soc. Lond., A 328: 309-327.

Hansen, U., and Ebel, A., 1984. Experiments with a numerical model related to mantle convection: boundary layer behaviour of small- and large scale flows. Phys.Earth Plan.Int., 36: 374-390.

Hansen, U., and Ebel, A., 1988. Time dependent thermal convection - a possible explanation for multiscale flow in the Earth's mantle. Geoph.J., 94: 181-191.

Hansen, U., Yuen, D.A., and Kroening, S.E., 1990. Transition to hard turbulence in thermal convection at infinite Prandtl numer. Phys. Fluids, A2(12): 2157-2163.

Hansen, U., Yuen, D.A., and Kroening, S.E., 1991. Effects of depth-dependent thermal expansivity on mantle circulations and lateral thermal anomalies, Geophys. Res. Lett., 18: 1261-1264.

Hansen, U., Yuen, D.A., and Kroening, S.E., 1992. Mass and heat transport in strongly time-dependent thermal convection at infinite Prandtl number, Geophys. Astrophys. Fluid Dyn., 63: 67-89.

Hansen, U., Steinbach, V., and Yuen, D.A., 1993. The dynamics at internal boundaries in an Earth's mantle with depth-dependent material properties. EUG VII, suppl. to Terra Nova, 5: 101.

Hatheway, A.W. and Kiersch, G.A., 1982. Engineering properties of rock. In: "Handbook of physical properties of rocks, Vol. II", Carmichael, R.S. (editor). CRC Press, 289-331.

Heard, H.C., 1972, Steady-state flow in polycrystalline halite at pressure of 2 kilobars. In: "Flow and fracture of rock", Heard, H.C., and others (editors). American Geophysical Union Geophysical Monograph Series, 16: 191-210.

Heinrich, J.C., Huyahorn, P.S., Zienckiewicz, O.C., and Mitchell, A.R., 1977. An upwind finite element scheme for two-dimensional convective transport equations. Int.J.Num.Meth.Eng., 11: 131-143.

Hoffman, P.F., and Ranalli, G., 1988. Archaean oceanic flake tectonics. Geophys.Res.Lett., 15: 1077-1080.

Horseman, S.T. and Handin, J., 1990. Triaxial compression tests on rocksalt at temperatures from 50 °C to 200 °C and strain rates from 10^{-4} to 10^{-9}/s. American Geophysical Union monograph series, 56: 103-110.

Horseman, S.T., Russel, J.E., Hardin, J., and Carter, N.L., 1992. Slow experimental deformation of Avery Island Salt. In: "Proceedings of the Seventh Internation Symposium on salt", April 6-9 1992, Kyoto, Japan, in press.

Hughes, T.J.R., 1987. The finite element method. Prentice-Hall, Englewood Cliffs, N.J.

Hughes, T.J.R., and Brooks, A., 1982. A theoretical framework for Petrov-Galerkin methods with discontinuous weighting functions: application of the streamline-upwind procedure, in: "Finite elements in fluids", Gallagher, R.H., Norrie, D.H., Oden, T.J., and Zienkiewicz, O.C. (Eds), Wiley, New York, 4: 47-65

Hunsche, U., 1977. Modellrechnungen zur Entstehung von Salzstockfamilien. Diss. Techn. Univ. Braunschweig, 102 pp.

Ita, J., and Stixrude, L., 1992. Petrology, elasticity and composition of the mantle transition zone. J.Geoph.Res., 97: 6849-6866.

Ito, E., and Takahashi, E., 1989. Postspinel transformations in the system $Mg_2SiO_4 - Fe_2SiO_4$ and some geophysical implications. J.Geoph.Res., 94: 10637-10646.

Jackson, M.J. and H.N. Pollack, 1984. On the sensitivity of parameterized convection to the rate of

decay of internal heat sources, J.Geoph.Res., 84: 10103-10108.

Jackson, M.J., and Pollack, H.N., 1987. Mantle devolatilization and convection: implications for the thermal history of the earth. Geoph.Res.Lett., 14: 737-740.

Jackson, M.P.A., and Talbot, C.J., 1986. External shapes, strain rates, and dynamics of salt structures. Geol.Soc.Amer.Bull., 97: 305-323.

Jackson, M.P.A., Cornelius, R.R., Craig, C.H., Gansser, A., Stoecklin, J., and Talbot, C.J., 1990. Salt diapirs of the Great Kavir, Central Iran. Geol.Soc.Amer., Memoir 177.

Jaques, A.L., and Green, D.H., 1980. Anhydrous melting of peridotite at 0-15 kb pressure. Contr.Mineral.Petr., B73: 287-310.

Jarvis, G.T. and McKenzie, D.P., 1980. Convection in a compressible fluid with infinite Prandtl number. J. Fluid Mech., 96: 515-583.

Jarvis, G.T. and Peltier, W.R., 1982. Mantle convection as a boundary-layer phenomenon, Geophys. J.R. Astron. Soc., 68: 385-424.

Jeanloz, R., 1985. Thermodynamics of phase transitions. Rev.Mineral., 14: 389-429.

Jeanloz, R., and Morris, S., 1986. Temperature distribution in the crust and mantle. Ann.Rev.Earth Planet.Sci., 14: 377-415.

Jenyon, M.K., 1986. Salt tectonics, Elsevier, London.

Karato, S., 1988. The role of recrystallization in the preferred orientation of olivine, Phys. Earth Planet. Inter., 51, 107-122.

Karato, S., 1989. Plasticity-crystal structure systematics in dense oxides and its implications for the creep strength of the Earth's deep interior: a preliminary result. Phys.Earth Plan.Int., 64: 37-51.

Karato, S., 1992. On the Lehmann discontinuity. Geophys.Res.Lett., 19: 2255-2259.

Karato, S., Paterson, M.S., and FitzGerald, J.D., 1986. Rheology of synthetic olivine aggregates: influence of grain size and water, J. Geophys. Res., 91: 8151-8176.

Karato, S., and Li, P., 1992. Diffusion creep in the perovskite: implications for the rheology of the lower mantle, Science, 255: 1238-1240.

Kellogg, L.H., 1991. Interactions of plumes with a compositional boundary at 670 km. Geophys.Res.Lett., 18: 865-868.

Kirby, S.H., 1983. Rheology of the lithosphere, Rev.Geoph., 21:1458-1487.

Kirby, S.H., and Kronenberg, A.K., 1987. Rheology of the lithosphere: selected topics. Rev.Geoph., 25: 1219-1244.

Kopitzke, U., 1977. Modellrechnungen zur Konvektion in Erdmantel mit Hilfe von Projektionsverfahren in Spline-Raeumen. Diplomarbeit, Braunschweig.

Kopitzke, U., 1979. Finite element convection models: comparison of shallow and deep mantle convection, and temperatures in the mantle. J.Geoph., 46: 97-121.

Larson, R.L., 1991. Latest pulse of the Earth: evidence for a mid-Cretaceous superplume. Geology, 19: 547-550.

Lenardic, A., and Kaula, W.M., Tectonic plates and the nature of mantle plumes. Submitted to Earth Plan.Sci.Lett., 1993.

Liu, M., Yuen, D.A., Zhao, W., and Honda, S., 1991. Development of diapiric structures in the upper mantle due to phase transitions, Science, 252: 1836-1839.

Machetel, P. and Yuen, D.A., 1989. Penetrative convective flows induced by internal heating and mantle compressibility, J. Geophys. Res., 94: 10609-10626.

Malevsky, A.V. and Yuen, D.A., 1991. Characteristics-based methods applied to very high Rayleigh number and infinite Prandtl number thermal convection. Phys. Fluids, A3: 2105-2115.

Malevsky, A.V. and Yuen, D.A., 1992. Strongly chaotic non-Newtonian mantle convection. Geophys.Astrophys. Fluid Dynamics, 65: 149-171.

Malvern, L.E., 1969. Introduction to the mechanics of a continuous medium. Prentice-Hall,

Englewood-Cliffs, N.J.

Mart, Y., and Hall., J.K., 1984. Structural trends in the northern Red Sea. J.Geoph.Res., 89: 352-364.

McGovern, P.J., and Schubert, G., 1989. Thermal evolution of the Earth: effects of volatile exchange between atmosphere and interior. Earth Plan.Sci.Lett., 96: 27-37.

McKenzie, D.P., 1984. The generation and compaction of partially molten rock. J.Petr., 25: 713-765.

McKenzie, D., and Bickle, M.J., 1988. The volume and composition of melt generated by the extension of the lithosphere. J.Petr., 29:625-679.

Meade, C., and Jeanloz, R., 1990. The strength of mantle silicates at high pressure and room temperature: implications for the viscosity profile of the mantle. Nature, 348: 533-535.

Menard, H.W. and McNutt, M.K., 1982. Evidence for and consequences of thermal rejuvenation, J. Geophys. Res., 87: 8570-8580.

Miller, G.H., Stolper, E.M., and Ahrens, T.J., 1991. The equation of state of a molten komatiite 2. application to komatiite petrogenesis and the Hadean mantle. J.Geoph.Res., 96: 11849-11864.

Nettleton, L.L., 1934. Fluid mechanics of salt domes, Bull.Am.Ass.Petrol.Geol., 18: 1175-1204.

Nisbet, E.G., and Fowler, C.M.R., 1983. Model for Archaean plate tectonics. Geology, 11: 376-379.

Nisbet, E.G., 1987. The young Earth: an introduction to Archaean geology. Allen & Unwin, London.

O'Connell, R.J., and Hager, B.H., 1980. In: "Physics of the Earth's interior", A.M. Dziewonski and E. Boschi (eds), 270-317, Elsevier, New York.

Ogawa, M. 1988. Numerical experiments on coupled magmatism-mantle convection system: implications for mantle evolution and Archean continental crust. J.Geophys.Res., 93: 15119-15134.

O'Hara, M.J., Saunders, M.J., and Mercy, E.L.P., 1975. Garnet-peridotite, primary ultrabasic magma and eclogite: interpretation of upper mantle processes in kimberlite. Phys.Chem.Earth, 9: 571-604.

Olson, P., Schubert, G., Anderson, C., and Goldman, P., 1988. Plume formation and lithosphere erosion: A comparison of laboratory and numerical experiments, J. Geophys. Res., 93: 15065-15084.

Osako, M. and Ito, E., 1991. Thermal diffusivity of $MgSiO_3$ perovskite, Geophys. Res. Lett., 18: 239-242.

Oxburgh, E.R., and Parmentier, E.M., 1977. Compositional and density stratification in oceanic lithosphere - causes and consequences. J.Geol.Soc.London, 133: 343-355.

Parmentier, E.M., Turcotte, D.L., and Torrance, K.E., 1975. Numerical experiments on the structure of mantle plumes. J.Geoph.Res., 80: 4417-4425.

Parmentier, E.M., Turcotte, D.L., and Torrance, K.E., 1976. Studies of finite amplitude non-Newtonian thermal convection with application to convection in the earth's mantle. J.Geoph.Res., 81: 1839-1846.

Parmentier, E.M., and Hess, P.C., 1992. Chemical differentiation of a convecting planetary interior: consequences for a one plate planet such as Venus. Geoph.Res.Lett., 19: 2015-2018.

Pironneau, O., 1982. On the transport-diffusion algorithm and its applications to the Navier-Stokes equations, Num. Mathematik, 38: 309-332.

Poliakov, A., and Podladchikov, Y., 1992. Diapirism and topography. Geophys.J.Int., 109: 553-564.

Poliakov, A., Van Balen, R., Podladchikov, Y., Daudre, B., Cloething, S., and Talbot, C.J., 1993. Numerical analysis of how sedimentation and redistribution of surficial sediments affects salt diapirism. submitted to *Tectonophysics*

Rabinowicz, M., Ceuleneer, G., Monnereau, M., and Rosenberg, C., 1990. Three-dimensional models of mantle flow across a low viscosity zone: implications for hot spot dynamics, Earth Plan. Sci. Lett., 99: 170-184.

Ramberg, H., 1981. Gravity, deformation and the Earth's crust in theory, experiments and geologic application. Academic Press, London, 2nd ed., 452 pp.

Ranalli, G., 1987. Rheology of the Earth. Allen and Unwin, Boston.

Remmelts, G., and Van Rees, D.J., 1992. Structureel-geologische ontwikkeling van zoutstructuren in noord-Nederland en het Nederlands deel van het continentaal plat. Dutch Geological Survey, report 30105/TRB2.

Ricard, Y. and Wuming, B., 1991. Inferring viscosity and the 3-D density structure of the mantle from geoid, topography and plate velocities, Geophys. J. Int., 105, 561-572.

Ringwood, A.E., 1975. Composition and petrology of the Earth's mantle. McGraw-Hill, New York.

Roemer, M., and Neugebauer, H., 1991. The salt dome problem: a multilayered approach. J.Geoph.Res., 96: 2389-2396.

Schilling, J.G., 1985. Upper mantle heterogeneities and dynamics, Nature, 314: 62-67.

Schilling, J.G., 1991. Fluxes and excess temperatures of mantle plumes inferred from their interaction with migrating mid-ocean ridges, Nature, 352, 397-403.

Schmeling, H., 1987. On the relation between initial conditions and late stages of Rayleigh-Taylor instabilities. Tectonophysics, 133: 65-80.

Schoen, J., 1983. Petrophysik. Ferdinand Enke Verlag, pp.405.

Schubert, G., Yuen, D.A., and Turcotte, D.L., 1975. Role of phase transitions in a dynamic mantle. Geophys.J.R.astr.Soc., 42: 705-735.

Schubert, G., Stevenson, D., and Cassen, P., 1980. Whole planet cooling and the radiogenic heat source contents of the Earth and Moon. J.Geoph.Res., 85: 2531-2538.

Schultz, M.H., 1973. Spline Analysis, Prentice-Hall, Englewood-Cliffs, N.J.

Schultz-Ela, D.D., and Bobineau, J.P., 1992. Extension of a brittle layer over a ductile substratum, AGU fall meeting 1992, EOS Trans.AGU, 73: 561.

Sclater, J.G., Jaupart, J., and Galson, D., 1980. The heat flow through oceanic and continental crust and the heat loss of the Earth. Rev.Geoph.Space Phys., 18: 269-311.

Segal, A., and Praagman, N., 1984. Sepran user manual, Sepra, Leidschendam, The Netherlands.

Selig, F., and Wallick, G.C., 1966. Temperature distribution in salt domes and surrounding sediments, Geophysics, 2: 346-361

Sharpe, H.N. and W.R. Peltier, 1978. Parameterized mantle convection and the Earth's thermal history, Geoph.Res.Lett., 5: 737-740.

Silver, P., Carlson, P.W., and Olson, P.L., 1988. Deep slabs, geochemical heterogeneity and the large scale structure of mantle convection. Ann.Rev.Earth Plan.Sci., 16: 477-541.

Skrotzki, W., and Haasen, P., 1988. The role of cross slip in the steady-state creep of salt. In: "The mechanical behaviour of salt: proceedings of the second conference", Hardy, H.R., and Langer, M., (editors). Trans Tech Publications, Clausthal-Zellerfeld, 69-81.

Sleep, N.H., 1979. Thermal history and degassing of the earth: some simple calculations. J.Geol, 87: 671-686.

Sleep, N., and Windley, 1982. Archean plate tectonics: constraints and inferences. J.Geol., 90: 367-379.

Sloan, S.W., 1986. An algorithm for profile and wavefront reduction of sparse matrices. Int.J.Num.Meth.Engng., 23: 239-251.

Solomon, S.C., 1993. Venus: keeping that youthful look. Nature, 361: 114.

Spiers, C.J., Urai, J.L., Lister, G.S., Boland, J.N., and Zwart, H.J., 1986. The influence and fluid-rock interaction on the rheology of salt rock. Nuclear Science and Technology, EUR 10399 EN. Office for Official publications of the European Communities, Luxembourg.

Spiers, C.J., Urai, J.L., and Lister, G.S., 1988. The effect of brine (inherent or added) on rheology and deformation mechanisms in salt rock. In: "The mechanical behaviour of salt: proceedings of the second conference", Hardy, H.R., and Langer, M., (editors). Trans Tech Publications, Clausthal-Zellerfeld, 89-102.

Spiers, C.J., Peach, C.J., Brzesowsky, R.H., Schutjens, P.M.T.M., Liezenberg, J.L., and Zwart, H.J.,

1989. Long-term rheological and transport properties of dry and wet salt rocks. Nuclear Science and Technology, EUR 11848 EN. Office for Official publications of the European Communities, Luxembourg.

Spiers, C.J., Schutjens, P.M.T.M., Brzesowksy, R.H., Peach, C.J., Liezenberg, J.L., and Zwart, H.J., 1990. Experimental determination of constitutive parameters governing creep of rocksalt by pressure solution. In: "Deformation Mechanisms, Rheology and Tectonics", R.J. Knipe and E.H. Rutter (editors). Geological Society special publication 54: 215-227.

Stacey, F.D., 1977. Physics of the Earth, John Wiley, New York.

Stacey, F.D., 1980. The cooling Earth: a reappraisal. Phys.Earth Plan.Int., 22: 89-96.

Steinbach, V., 1991. Numerische Experimente zur Konvektion in kompressiblen Medien, PhD thesis, Koeln.

Steinbach, V., and Yuen, D.A., 1992. The effects of multiple phase transitions on Venusian mantle convection, Geoph.Res.Lett., 19: 2243-2246.

Stevenson, D.J., 1989. Formation and early evolution of the Earth. In: "Mantle Convection", W.R. Peltier (ed), 818-873, Gordon and Breach, New York.

Strang, G., and Fix, G.J., 1973. An analysis of the finite element method. Prentice-Hall, Englewood-Cliffs, N.J.

Tackley, P.J., Stevenson, D.J., Glatzmaier, G.A., and Schubert G., 1993. Effects of an endothermic phase transition at 670 km depth in a spherical model of convection in the Earth's mantle. Nature, 361: 699-704.

Takahashi, E., 1990. Speculations on the Archean mantle: missing link between komatiite and depleted garnet peridotite. J.Geoph.Res., 95: 15941-15954.

Talbot, C.J., 1977. Inclined and asymmetric upward-moving gravity structures. Tectonophysics, 42: 159-181.

Tatsumi, Y., and Kimura, N., 1991. Secular variation of basalt chemistry in the Kenya Rift: evidence for the pulsing of asthenospheric upwelling. Earth Plan.Sci.Lett., 104, 99-113, 1991.

Temam, R., 1977. Navier-Stokes equations, theory and numerical analysis, North Holland, Amsterdam, 2nd ed.

Urai, J.L., Spiers, C.J., Zwart, H.J., and Lister, G.S., 1986. Water weakening effects in rocksalt during long term creep. Nature, 324: 554-557.

Urai, J.L., Spiers, C.J., Peach, C.J., Franssen, R.C.M.W., and Liezenberg, J.L., 1987. Deformation mechanisms operating in naturally deformed halite as deduced from microstructural investigations. Geologie and Mijnbouw, 66: 165-176.

Van den Berg, A.P., Yuen, D.A., and Van Keken, P.E., 1991. Effects of depth-variations in creep laws on the formation of plates in mantle dynamics. Geoph.Res.Lett., 18: 2197-2200.

Van den Berg, A.P., Van Keken, P.E., and Yuen, D.A., 1993. The effects of a composite non-Newtonian and Newtonian rheology on mantle convection. Geoph.J.Int., in press.

Van Keken, P.E., Yuen, D.A., and Van den Berg, A.P., 1992. Pulsating diapiric flows: Consequences of vertical variations in mantle creep laws. Earth Plan.Sci.Lett., 112: 179-194.

Vendeville, B.C., and Cobbold, P.R., 1987. Glissements gravitaires synsédimentaires et failles normales listriques: modèles expérimentaux. Compt.Rend.Acad.Sci., Paris, série II, 305: 1313-1319.

Vendeville, B.C., and Jackson, M.P.A., 1992. The rise of diapirs during thin-skinned extension. Mar.Petr.Geol. 9: 331-353.

Vening Meinesz, F.A., 1962. Thermal convection in the earth's mantle. In: "Continental Drift", S.K. Runcorn (ed), Academic Press, New York, 145-176.

Verhoogen, J., 1965. Phase changes and convection in the Earth's mantle. Phil.Trans.R.Soc.London A, 258: 276.

Vlaar, N.J., 1975. The driving mechanism of plate tectonics: a qualitative approach. In: "Progress in

Geodynamics", G.J. Borradaile and others (eds), North-Holland, Amsterdam.

Vlaar, N.J., 1985. Precambrian geodynamical constraints. In: "The deep proterozoic crust in the North Atlantic Provinces", Tobi, A.C., and Touret, J.L.R. (eds), D. Reidel Publishing Company.

Vlaar, N.J., 1986. Archaean global dynamics. Geologie en Mijnbouw, 65: 91-101.

Vlaar, N.J., and Wortel, M.J.R., 1976. Lithospheric aging, instability and subduction. Tectonophysics, 32: 331-351.

Vlaar, N.J., and Van den Berg, 1991. Continental evolution and archaeo-sea-levels. In: "Glacial Isostasy, Sea-level and Mantle Rheology", Sabadini, R., Lambeck, K., and Boschi, E. (eds), Kluwer Academic Publishers, Dordrecht

Vlaar, N.J., Van Keken, P.E., and Van den Berg, 1993. Cooling of the Earth in the Archaean: consequences of pressure-release melting in a hotter mantle. Submitted to Earth Plan.Sci.Lett.

Vonnegut, K., 1976. Slapstick. 243 pp. Dell, N.Y.

Wang Z., Karato, S., and Fujino, K., 1991. High-temperature plasticity of garnets II, Eos.Trans., AGU, 72: 452,

Wawersik, W.R., and Zeuch, D.H., 1986. Modeling and mechanistic interpretation of creep of rocksalt below 200 °C. Tectonophysics, 121: 125-152.

Weertman, J. and J.R. Weertman, 1975. High temperature creep of rock and mantle viscosity, Ann.Rev.Earth Planet.Sci, 3: 293-315.

Weinberg, R.F., and Schmeling, H., 1992. Polydiapirs: multiwavelength gravity structures. J.Struct.Geol., 14: 425-436.

Whitehead, J., and D. Luther, 1975. Dynamics of laboratory diapir and plume models. J.Geoph.Res, 80: 705-717.

Williams, D.R., and Pan, V., 1992. Internally heated mantle convection and the thermal and degassing history of the Earth. J.Geoph.Res., 8937-8950.

Woidt, W.D., 1978. Finite element calculations applied to salt dome analysis. Tectonophysics, 50: 369-386.

Woidt, W.D., 1980. Analytische und numerische Modellexperimente zur Physik der Salzstockbildung. PhD thesis, Braunschweig.

Woodbury, H.O., Murray, I.B., Jr., Pickford, P.J., and Akers, W.H., 1973. Pliocene and Pleistocene depocenters, outer continental shelf, Louisiana and Texas. Am.Ass.Petr.Geol.Bull., 57: 2428-2439.

Yuen, D.A. and Fleitout, L.M., 1985. Thinning of the lithosphere by small-scale convective destabilization, Nature, 313: 125-128

Yuen, D.A., Leitch, A.M., and Hansen, U., 1991. Dynamical influences of pressure-dependent thermal expansivity on mantle convection, in "Glacial Isostasy, Sea-level and Mantle Rheology", R. Sabadini and K. Lambeck (eds), 663-701, Kluwer Acad. Publ.

Zaleski, S., and Julien, P., 1992. Numerical simulation of Rayleigh-Taylor instabilitiy for single and mulitple salt diapirs. Tectonophysics, 206:55-69.

Zhang, Y.S. and Tanimoto, T., 1992. Ridges, hotspots and their interaction as observed in seismic velocity maps, Nature, 355, 45-49.

Zhao, W., Yuen, D.A., and Honda, S., 1992. Multiple phase transitions and the style of mantle convection, Phys.Earth Plan.Int., 72: 185-210.

Zienkewicz, O.C., 1977. The finite element method. McGraw-Hill, London, 787 pp.

Samenvatting (Summary in Dutch)

In de 25 jaar na de algemene aanvaarding van het concept van plaattektoniek zijn we getuige geweest van grote vooruitgang in observationele, laboratorium, voorwaartse modellering en inversie technieken. Deze geven een helder beeld van de grote complexiteit die ons tegemoet treden wanneer we de dynamica van het inwendige van de aarde willen bestuderen. Plaattektoniek kan gezien worden als zowel de uitdrukking als het controlerende mechanisme van de dynamische afkoeling van de aarde. Traditioneel zijn de soloïstische en vaak tegengestelde, vereenvoudigende invalshoeken aangenomen van ofwel de 'convectionist', die plaattektoniek ziet als de oppervlakte uitdrukking van mantelconvectie, of de 'tektonist', die de platen ziet als de enige dynamische component in een verder passieve aarde. Vanuit de observationele gegevens, kennis van deformatiemechanismen en de beschikbare resultaten van modelleringen en inversies wordt het steeds meer duidelijk, dat een benadering die beide gezichtspunten combineert, beter geschikt is om de dynamica van de aarde te beschrijven. Deze algemene beschrijving wordt bemoeilijkt door de sterk afwijkende karakteristieken van de lithosfeer, uitgedrukt door de thermische, compositionele en rheologische verschillen ten opzichte van de onderliggende mantel. In dit proefschrift presenteer ik enige modelstudies over de deformatie van lithosfeer en mantel. Centraal hierin staat de sterke invloed van de compositionele en rheologische verschillen. De benadering is meer 'convectionistisch' dan 'tektonistisch'. Het brosse en elastische gedrag van de bovenste en koudste delen van de lithosfeer wordt niet in beschouwing genomen.

Het gecompliceerde rheologische en dynamische gedrag van de aarde maakt het gebruik van vereenvoudigende aannamen noodzakelijk. Enige van deze aannamen worden in de volgende paragrafen besproken.

    De langzame deformatie van de aarde beneden de bovenste delen van de lithosfeer wordt bepaald door ductiele deformatie, of kruip, bij hoge temperatuur en druk. Experimenteel werk aan het deformatiegedrag onder deze condities laat zien dat het kruipgedrag van kandidaat-mantelgesteente goed beschreven wordt door een niet-Newtonse wet, waarin de kruipsnelheid niet-lineair afhangt van de spanning die op het gesteente wordt uitgeoefend. Theoretische modellen voor het deformatiegedrag worden gebruikt om de laboratoriumgegevens te extrapoleren naar de

omstandigheden die in de aarde gelden. Verschillende mechanismen, die gebaseerd zijn op het bewegen van dislocaties in kristallen, kunnen het niet-Newtonse gedrag verklaren. Naast de dislocatiekruip is het Newtonse, of lineaire, mechanisme van diffusiekruip van belang. Hierbij vindt deformatie plaats door diffusie van materiaal door en/of langs het oppervlak van de kristalkorrels. Dit mechanisme wordt niet vaak geobserveerd in laboratoriummetingen, maar het wordt verondersteld dat het van groot belang is voor de zeer langzame deformatie van de aarde, die niet in het laboratorium gesimuleerd kan worden.

Uit de behoudswetten voor impulsmoment, thermische energie en massa, worden differentiaalvergelijkingen afgeleid die de deformatie van de lithosfeer en mantel beschrijven. Hierbij wordt de aanname gemaakt dat de aarde als een Boussinesq vloeistof bij oneindig Prandtl getal kan worden beschreven. Dit impliceert dat visceuze dissipatie wordt verwaarloosd, de vloeistof inkompressibel is, en alle materiaalparameters konstant zijn, behalve in de drijf- of Archimedesterm van de bewegingsvergelijking. In de praktijk wordt deze laatste conditie versoepeld om, bijvoorbeeld variabele viscositeit en thermische diffusiviteit toe te staan. In het algemeen zijn de differentiaalvergelijkingen tijdafhankelijk, niet-lineair en niet-lineair gekoppeld. Alleen in extreem vereenvoudigde gevallen kan een analytische, of wiskundig exacte, oplossing worden gevonden. In het algemene geval zijn numerieke methoden noodzakelijk om oplossingen te vinden.

In de laatste jaren is het in toenemende mate mogelijk geworden om driedimensionale modellen te bestuderen. Het wordt verwacht dat binnen een aantal jaren de vooruitgang in rekenkundige methoden en de toenemende beschikbaarheid van snelle computers het mogelijk zal maken driedimensionale en tijdafhankelijke modellen met realistische rheologie te bestuderen. Voor het soort modellen als behandeld in dit proefschrift is het echter nog noodzakelijk om ons te beperken tot alleen tweedimensionale gevallen. In veel gevallen is dit een redelijke aanname, omdat het voorgesteld kan worden dat de modellen niet variëren in de derde dimensie.

Hoofdstuk 2 beschrijft de mathematische vergelijkingen voor het de ductiele deformatie van de lithosfeer en mantel onder bovenstaande aannamen. De eindige elementen methoden, die gebruikt worden om de niet-lineaire en tijdafhankelijke differentiaalvergelijkingen op te lossen worden beschreven in hoofdstuk 3. De methoden worden getest met gepubliceerde resultaten, waaruit blijkt dat de methoden zeer nauwkeurig zijn in het modelleren van thermische convectie in gegeneraliseerd Newtonse media. In de eindige elementen methoden beschreven in hoofdstuk 3 wordt het aangenomen dat de fundamentele natuurkundige grootheden, zoals temperatuur en snelheid, beschreven kunnen worden als continue functies. In veel geofysische toepassingen, verandert de compositie discontinu over grensvlakken (b.v. op de grens tussen zout en sediment bij zoutkoepels). In het algemeen is de

viscositeit en de daarvan afhankelijke deformatiesnelheid discontinu over zo'n grensvlak. Deze discontinuïteit kan niet nauwkeurig worden met continue functies en toepassing hiervan leidt tot niet-fysische oscillaties in deformatiesnelheid en, bij niet-Newtonse media, in de viscositeit. Om dit te voorkomen is een alternatieve Lagrangiaanse methode gebruikt, waarbij de deformatie gemodelleerd wordt met behulp van een deformerend eindige elementen grid (hoofdstuk 4).

De methoden worden toegepast op drie verschillende problemen:

Zouttektoniek

Eerst wordt het probleem van zouttektoniek beschouwd. Steenzout is vrij zwak en deformeert ductiel zelfs onder bovenkorstcondities. De vorming van zoutdiapieren, of zoutkoepels, is van groot economisch belang, gezien de rol die zij spelen in het vasthouden van olie- en gasreservoirs, en het mogelijke gebruik voor langdurige opslag van radioactief afval en energievoorraden. In voorgaande experimentele en numerieke modellering van zouttektoniek is gebruik gemaakt een constante, Newtonse rheologie voor het zout. In hoofdstuk 5 wordt gebruik gemaakt van recente laboratoriummetingen, die aangeven dat zout deformeert door de gelijktijdig optredende mechanismen van dislocatie- en diffusiekruip. The effectieve viscositeit van steenzout hangt af van de gesteente-eigenschappen (zoals korrelgrootte, activatie-energie en schuifmodulus), temperatuur en deformatiesnelheid. Voor snelheden die kenmerkend zijn voor zoutdiapirisme, wordt gevonden dat de gemiddelde viscositeit van het zout varieert tussen 10^{17} Pa · s (voor kleine korrelgrootte en hoge temperatuur) en 10^{20} Pa · s (voor grote korrelgrootte en lage temperatuur). Bij grotere korrelgrootte is het dislocatiekruip mechanisme dominant gedurende het actieve gedeelte van het diapirisme. Bij lagere snelheden en bij fijnkorrelig zout, met daarin zeer geringe hoeveelheden water, vindt deformatie voornamelijk plaats door diffusiekruip. De waarden voor de viscositeit van steenzout die traditioneel gebruikt zijn in numerieke en experimentele modellen zijn aan de lage kant van het interval van waarden dat hier gevonden wordt.

Mantelconvectie

Vervolgens wordt de invloed van rheologische overgangen in de aarde op grootschalige mantelconvectie besproken. De precieze rol van de transitiezone, tussen 400 en 670 km diepte, is nog steeds onbekend. Sommigen beschrijven de seismische overgang tussen onder- en bovenmantel op 670 km diepte als een chemische overgang, anderen als een fase-overgang, maar velen laten de keuze tussen beide mogelijkheden open. Er zijn veel studies bekend naar het effect van de

voorgestelde compositionele en/of met de fase-overgang gerelateerde discontinuïteiten op mantelconvectie. Recente laboratoriumresultaten van Karato & Li wijzen erop dat de ondermantel voornamelijk via diffusiekruip deformeert. Dit geeft het interessante model van een niet-Newtonse bovenmantel op een Newtonse ondermantel. Hoofdstukken 6 en 7 bespreken het effect van deze rheologische overgangen op de dynamica van de mantel. Bestudeerd zijn tijdafhankelijke modellen van de interactie tussen opwellende mantelpluimen en de grens tussen onder- en bovenmantel. Het blijkt dat het hete, continue opwellende ondermantelmateriaal als discrete diapieren in de bovenmantel omhoog komt, geholpen door de effectieve viscositeitsverlaging en de niet-Newtonse effecten in de bovenmantel. De diapieren zijn zichtbaar aan het oppervlak als periodieke pulsen in de locale warmtestroom boven de pluim, die relatief stationair blijft ten opzichte van de daarboven bewegende lithosferische plaat. De frequentie van de pulsering hangt af van het Rayleigh getal, het effectieve viscositeitscontrast over het grensvlak en, zoals in hoofdstuk 7 wordt aangetoond, van het diepteniveau van het grensvlak. Diapieren die van een rheologische overgang boven in de transitiezone komen, blijken een periode te hebben van enkele miljoenen jaren, hetgeen vergelijkbaar is met de episodiciteit van vulkanisme bij oceanische eilanden, met als prominent voorbeeld de eilandketen van Hawaii.

Dynamica in het Archaïcum

Tenslotte wordt een model gepresenteerd dat de afkoeling van de aarde kan beschrijven gedurende het Archaïcum (de periode tussen ongeveer 3.5 en 2.7 miljard jaar geleden). Geologische observaties geven een tegenstrijdig beeld over de karakteristieke temperaturen van de bovenmantel in het Archaïcum. Aan de ene kant worden komatiiten gevonden, magmatische gesteenten met zeer hoge uitvloeiingstemperatuur, die wijzen op een maximale temperatuur die zo'n 400-500 °C hoger ligt dan tegenwoordig. Aan de andere kant wijst de metamorfische signatuur van de Archaïsche continentale schilden erop, dat de continentale lithosfeer thermisch vergelijkbaar was met de huidige. Deze schijnbare tegenstelling kan verklaard worden met een model waarin de schilden vroeg in het Archaïcum stabiel werden en relatief lage temperaturen op 50-100 km diepte kon handhaven. De afkoeling van de aarde werd bepaald door convectie onder de oceanen. De meeste onderzoekers adopteren het standpunt dat de huidige vorm van plaattektoniek ook in het Archaïcum kon opereren. Het is echter niet waarschijnlijk dat plaattektoniek in een hetere aarde plaats heeft kunnen vinden. Eén van de consequenties van hogere temperaturen is de grotere hoeveelheden compositioneel licht basalt, dat bij midoceanische ruggen wordt gegenereerd. In de huidige situatie wordt een korst met een dikte van ongeveer 7 km gevormd. De pas gevormde lithosfeer is stabiel ten opzichte van de onderliggende mantel. Pas als de afkoeling van het

aardoppervlak voldoende is doorgedrongen kan de lithosfeer instabiel worden en subduceren. In een hetere mantel wordt aanzienlijk meer basalt geproduceerd. Samen met de daaronder liggende, compositioneel stabiel gelaagde Harzburgiet vormt het een oceanische lithosfeer die zeer lang stabiel blijft tegen afkoeling. Het gebrek aan mechanische coherentie van de lithosfeer maakt de huidige vorm van plaattektoniek onwaar-schijnlijk. In hoofdstuk 8 wordt een model gepresenteerd dat hiervoor een alternatief kan vormen. In de dikke basaltlaag die gevormd wordt bij hoge manteltemperaturen kan, door mechanische ontkoppeling van boven- en onderkorst, de brosse en gehydrateerde bovenkorst subduceren in de ductiele onderkorst. In de onderkorst zijn druk- en temperatuurcondities aanwezig om de basalt efficient in de hogere druk fase eclogiet om de drukken. Het zware eclogiet zinkt snel weg in de onderliggende mantel en dit zorgt voor hernieuwde vorming van basaltische smelt. De consumptie van latente warmte en advectieve koeling door de migratie van het magma kan de aarde efficient afkoelen. Het wordt voorgesteld dat dit mechanisme de mantel met enkele honderden graden heeft doen afkoelen in het vroege Archaïcum.

Curriculum Vitae

De auteur van dit proefschrift werd geboren op 29 maart 1966 te Hoevelaken. Hij behaalde het einddiploma Gymnasium-β aan het Stedelijk Gymnasium Johan van Oldenbarnevelt te Amersfoort op 17 mei 1984. In datzelfde jaar werd begonnen met de studie geofysica aan de Universiteit van Utrecht. Op 23 september 1985 werd het propaedeuse examen met goed gevolg afgelegd. Het doctoraaldiploma geofysica werd op 27 februari 1989 behaald. Van 1 maart 1989 tot 1 maart 1993 is de auteur verbonden geweest aan het Instituut van Aardwetenschappen te Utrecht bij de vakgroep geofysica als assistent in opleiding.

Acknowledgments (Dankbetuiging)